

# Optical Characterization of Nanomaterials

Guest Editors: Mun Seok Jeong, Gon Namkoong, Clare C. Byeon,  
Jong Su Kim, and Hong Seok Lee





---

# **Optical Characterization of Nanomaterials**

## **Optical Characterization of Nanomaterials**

Guest Editors: Mun Seok Jeong, Gon Namkoong,  
Clare C. Byeon, Jong Su Kim, and Hong Seok Lee



Copyright © 2014 Hindawi Publishing Corporation. All rights reserved.

This is a special issue published in “Journal of Nanomaterials.” All articles are open access articles distributed under the Creative Commons Attribution License, which permits unrestricted use, distribution, and reproduction in any medium, provided the original work is properly cited.



## Editorial Board

Katerina E. Aifantis, USA  
Nageh K. Allam, USA  
Margarida Amaral, Portugal  
Xuedong Bai, China  
Lavinia Balan, France  
Enrico Bergamaschi, Italy  
Theodorian Borca-Tasciuc, USA  
C. Jeffrey Brinker, USA  
Christian Brosseau, France  
Xuebo Cao, China  
Shafiul Chowdhury, USA  
Kwang-Leong Choy, UK  
Cui ChunXiang, China  
Miguel A. Correa-Duarte, Spain  
Shadi A. Dayeh, USA  
Ali Eftekhari, USA  
Claude Estournès, France  
Alan Fuchs, USA  
Lian Gao, China  
Russell E. Gorga, USA  
Hongchen Chen Gu, China  
Mustafa O. Guler, Turkey  
John Z. Guo, USA  
Smrati Gupta, Germany  
Michael Harris, USA  
Zhongkui Hong, China  
Michael Z. Hu, USA  
David Hui, USA  
Y.-K. Jeong, Republic of Korea  
Sheng-Rui Jian, Taiwan  
Wanqin Jin, China  
Rakesh K. Joshi, UK  
Zhenhui Kang, China  
F. Karimzadeh, Iran  
Alireza Khataee, Iran

Do K. Kim, Korea  
Alan K. T. Lau, Hong Kong  
Burtrand Lee, USA  
Jun Li, Singapore  
Benxia Li, China  
Xing-Jie Liang, China  
Shijun Liao, China  
Gong-Ru Lin, Taiwan  
Tianxi Liu, China  
Jun Liu, USA  
Songwei Lu, USA  
Daniel Lu, China  
Jue Lu, USA  
Ed Ma, USA  
Gaurav Mago, USA  
Santanu K. Maiti, India  
Sanjay R. Mathur, Germany  
V. Mittal, UAE  
Weihai Ni, Germany  
Sherine Obare, USA  
Atsuto Okamoto, Japan  
Abdelwahab Omri, Canada  
Edward A. Payzant, USA  
Kui-Qing Peng, China  
Anukorn Phuruangrat, Thailand  
Mahendra Rai, India  
Suprakas Sinha Ray, South Africa  
Ugur Serincan, Turkey  
Huaiyu Shao, Japan  
Donglu Shi, USA  
V. Sivakov, Germany  
M. Striccoli, Italy  
Bohua Sun, South Africa  
Saikat Talapatra, USA  
Nairong Tao, China

T. Thongtem, Thailand  
S. Thongtem, Thailand  
Alexander Tolmachev, Ukraine  
Valeri P. Tolstoy, Russia  
Tsung-Yen Tsai, Taiwan  
Takuya Tsuzuki, Australia  
Raquel Verdejo, Spain  
Mat U. Wahit, Malaysia  
Zhenbo Wang, China  
Ruibing Wang, Canada  
Shiren Wang, USA  
Cheng Wang, China  
Yong Wang, USA  
Jinquan Wei, China  
Ching-Ping Wong, Hong Kong  
Xingcai Wu, China  
Guodong Xia, Hong Kong  
Ping Xiao, UK  
Zhi Li Xiao, USA  
Yangchuan Xing, USA  
Shuangxi Xing, China  
Nanping Xu, China  
Doron Yadlovker, Israel  
Yingkui Yang, China  
Khaled Youssef, USA  
Kui Yu, Canada  
William W. Yu, USA  
Haibo Zeng, China  
Tianyou Zhai, China  
Renyun Zhang, Sweden  
Bin Zhang, China  
Yanbao Zhao, China  
Lianxi Zheng, Singapore  
Chunyi Zhi, Hong Kong

## Contents

**Optical Characterization of Nanomaterials**, Mun Seok Jeong, Gon Namkoong, Clare C. Byeon, Jong Su Kim, and Hong Seok Lee  
Volume 2014, Article ID 739212, 2 pages

**Optical Characterization of Silver Nanorod Thin Films Grown Using Oblique Angle Deposition**, Michael Benson, Piyush Shah, Michael Marciniak, Andrew Sarangan, and Augustine Urbas  
Volume 2014, Article ID 694982, 8 pages

**Formation and Evolution Mechanism of Plasmon Resonance from Single Ring-Shaped Nanotube to Dimer and Arrays**, F. Q. Zhou, Z. M. Liu, H. J. Li, Z. F. Liu, B. Tang, and X. Zhou  
Volume 2014, Article ID 387208, 7 pages

**Effects of Hydrogen on the Optical and Electrical Characteristics of the Sputter-Deposited  $\text{Al}_{2/3}\text{O}_{3/2}$ -Doped ZnO Thin Films**, Fang-Hsing Wang, Cheng-Fu Yang, Jian-Chiun Liou, and In-Ching Chen  
Volume 2014, Article ID 857614, 7 pages

**Tunable Band Gap Energy of Mn-Doped ZnO Nanoparticles Using the Coprecipitation Technique**, Tong Ling Tan, Chin Wei Lai, and Sharifah Bee Abd Hamid  
Volume 2014, Article ID 371720, 6 pages

**Electroluminescent Devices Based on Junctions of Indium Doped Zinc Oxide and Porous Silicon**, F. Severiano, G. García, L. Castañeda, J. M. Gracia-Jiménez, Heberto Gómez-Pozos, and J. A. Luna-López  
Volume 2014, Article ID 409493, 7 pages

**The Effect of Thermal Annealing Processes on Structural and Photoluminescence of Zinc Oxide Thin Film**, Huai-Shan Chin and Long-Sun Chao  
Volume 2013, Article ID 424953, 8 pages

**Symmetric Negative Differential Resistance in a Molecular Nanosilver Chain**, Tae Kyung Kim, Hoi Ri Moon, and Byung Hoon Kim  
Volume 2013, Article ID 814694, 5 pages

**Effect of Annealing on the ZnS Nanocrystals Prepared by Chemical Precipitation Method**, Nadana Shanmugam, Shanmugam Cholan, Natesan Kannadasan, Kannadasan Sathishkumar, and G. Viruthagiri  
Volume 2013, Article ID 351798, 7 pages

**Novel Method of Evaluating the Purity of Multiwall Carbon Nanotubes Using Raman Spectroscopy**, Young Chul Choi, Kyoung-In Min, and Mun Seok Jeong  
Volume 2013, Article ID 615915, 6 pages

## Editorial

# Optical Characterization of Nanomaterials

**Mun Seok Jeong,<sup>1</sup> Gon Namkoong,<sup>2</sup> Clare C. Byeon,<sup>3</sup> Jong Su Kim,<sup>4</sup> and Hong Seok Lee<sup>5</sup>**

<sup>1</sup> Department of Energy Science, Center for Integrated Nanostructure Physics, Institute for Basic Science, Sungkyunkwan University, Suwon 440-746, Republic of Korea

<sup>2</sup> Department of Electrical and Computer Engineering, Old Dominion University, Norfolk, VA 23529, USA

<sup>3</sup> School of Mechanical Engineering, Kyungpook National University, Daegu 702-701, Republic of Korea

<sup>4</sup> Department of Physics, Yeungnam University, Gyeongsan 712-749, Republic of Korea

<sup>5</sup> Department of Physics, Jeju National University, Jeju 690-756, Republic of Korea

Correspondence should be addressed to Mun Seok Jeong; [mjeong@skku.edu](mailto:mjeong@skku.edu)

Received 13 June 2014; Accepted 13 June 2014; Published 24 July 2014

Copyright © 2014 Mun Seok Jeong et al. This is an open access article distributed under the Creative Commons Attribution License, which permits unrestricted use, distribution, and reproduction in any medium, provided the original work is properly cited.

Studies on nanomaterials have recently been carried out widely and intensively in many fields in order to explore the new era of the nanoscopic world and to overcome the limitation of typicalness of the bulk materials. Nanomaterials with the enhanced mechanical, electrical, and optical properties distinctively different from the bulk material properties allow us to surmount many areas that the conventional technology could not address. Nowadays, such properties of the nanomaterials may be characterized electrically and mechanically by direct contact with the nanomaterials. Meanwhile, the optical methods take advantage of observing the essential characteristics of the nanomaterials without significantly modifying or permanently damaging them due to their noncontact and noninvasive nature. Common optical characterization methods include absorbance/transmittance, photoluminescence, and Raman scattering measurement.

This special issue arranges a series of up-to-date articles dealing with characterizing the various nanomaterials by using such optical characterization methods. M. Benson et al. discovers, from the absorbance analysis, the metamaterial properties of silver nanorod thin film grown by oblique angle deposition, “Optical characterization of silver nanorod thin films grown using oblique angle deposition.” Y. C. Choi et al. describes a purity analysis for carbon nanotubes by using Raman scattering, “Novel method of evaluating the purity of multiwall carbon nanotubes using Raman spectroscopy.” N. Shanmugam et al. reports the effect of thermal process on ZnS nanocrystals synthesized by chemical precipitation by

using UV-Vis absorption and photoluminescence, “Effect of annealing on the ZnS nanocrystals prepared by chemical precipitation method.” By FT-IR, absorbance, and fluorescence spectroscopy, T. L. Tan et al. observe the change in optical characteristics of Mn-doped ZnO nanoparticles synthesized by coprecipitation method while varying the manganese dopant concentration, “Tunable band gap energy of Mn-doped ZnO nanoparticles using the coprecipitation technique.” F. Severiano et al. introduces an electroluminescent device based on white light emission from ZnO:In/PS by electroluminescence and photoluminescence, “Electroluminescent devices based on junctions of indium doped zinc oxide and porous silicon.” By using photoluminescence, H.-S. Chin and L.-S. Chao investigate the thermal annealing effect on ZnO thin film grown by radio frequency sputtering, “The effect of thermal annealing processes on structural and photoluminescence of zinc oxide thin film.” Measuring the optical transmittance, F.-H. Wang et al. analyzes the hydrogen effect on sputter-deposited Al<sub>2</sub>O<sub>3</sub>-doped ZnO thin films, “Effects of hydrogen on the optical and electrical characteristics of the sputter-deposited Al<sub>2</sub>O<sub>3</sub>-doped ZnO thin films.” T. K. Kim et al. observes the negative differential resistance from molecular nanosilver chain, “Symmetric negative differential resistance in a molecular nanosilver chain.” F. Q. Zhou et al. proposes single ring-shaped nanotubes, dimmers, and arrays and discuss their optical transmission properties, “Formation and evolution mechanism of plasmon resonance from single ring-shaped nanotube to dimer and arrays.”

As we have seen from the papers in this special issue, the optical characterization methods are essential in analyzing the various fundamental and functional properties of the nanomaterials. The noncontact and noninvasive nature makes the optical characterization methods one of the best ideal and at the same time practical tools to investigate and to take advantage of many different types of nanomaterials. We believe that the articles in this special issue would serve as excellent examples of how these optical methods are utilized in characterization of some of the well-known nanomaterials.

*Mun Seok Jeong  
Gon Namkoong  
Clare C. Byeon  
Jong Su Kim  
Hong Seok Lee*

## Research Article

# Optical Characterization of Silver Nanorod Thin Films Grown Using Oblique Angle Deposition

Michael Benson,<sup>1</sup> Piyush Shah,<sup>2</sup> Michael Marciniak,<sup>1</sup>  
Andrew Sarangan,<sup>2</sup> and Augustine Urbas<sup>3</sup>

<sup>1</sup> Department of Engineering Physics, Air Force Institute of Technology, Wright-Patterson AFB, Dayton, OH 45433, USA

<sup>2</sup> Electro-Optics Graduate Program, University of Dayton, Dayton, OH 45469, USA

<sup>3</sup> Materials and Manufacturing Directorate, Air Force Research Laboratory, Wright-Patterson AFB, Dayton, OH 45433, USA

Correspondence should be addressed to Michael Benson; [mrbenson403@gmail.com](mailto:mrbenson403@gmail.com)

Received 18 November 2013; Accepted 2 April 2014; Published 15 May 2014

Academic Editor: Jong Su Kim

Copyright © 2014 Michael Benson et al. This is an open access article distributed under the Creative Commons Attribution License, which permits unrestricted use, distribution, and reproduction in any medium, provided the original work is properly cited.

Nanorods are metamaterial structures that have been shown to have wide application, ranging from biomedical uses to photovoltaic materials. These materials have unique optical characteristics. In this paper, two silver (Ag) nanorod thin-film samples are created using Glancing Angle Deposition (GLAD) at both near-room temperature ( $\sim 300$  K) and cryogenic temperature ( $\sim 100$  K). Generalized ellipsometry is used to measure the optical constants of the samples. The strong difference between the optical constants of the constituent materials and those of these thin films shows that the characteristics of the samples are due to how their metamaterial structures are defined. The principle optical axes of the films align well with the morphological characteristics of the nanostructures. The axis with the greatest index of refraction remains aligned to the principle axes but shifts orientation with respect to morphological characteristics between samples. Experimental results show differences in both magnitude and characteristics of the nanorod indexes. Reflectance and transmittance measurements are performed to extract absorptance data. The room temperature deposited sample shows a higher overall absorptance, while the cryogenic sample shows a clear orientation-dependent absorptance. Polarization data is analyzed to show that the 100 K thin film exhibits polarization-dependent absorptance, while the 300 K sample's absorptance has a strong orientation dependence.

## 1. Introduction

Nanorods can create materials with optical properties that are drastically different than their bulk material counterparts [1–3]. These structures have found a wide number of potential uses, ranging from biomedical applications [4] to photovoltaic device improvements [5]. The characterization of these structures has been studied extensively in a number of different places [6–9], focusing mostly on the optical constants of the material. Here, two nanorod samples are characterized using generalized ellipsometry and reflectance-based measurements to examine their varying optical properties, as well as their spectral absorptance properties.

## 2. Materials and Methods

**2.1. Growth Methodology.** The thin-film deposition method discussed in this study was done using a generic e-beam evaporation system (MDC evap-4000) made by Torr International. This chamber was retrofitted with a custom-built substrate holder to support thin-film growth at cryogenic ( $\sim 100$  K) and room ( $\sim 300$  K) temperatures concurrently. Liquid nitrogen was allowed to flow through the substrate holder in an open-loop configuration to achieve cryogenic substrate temperatures during the deposition process. Copper and teflon angle blocks with a preset angle of  $88^\circ$  were mounted on the substrate holder. Using mechanical clips, silicon (Si) substrates were attached to the angled surface of the block.

Two type-K thermocouples were attached to the angle blocks to measure substrate temperature during deposition. This experimental setup is shown in Figure 1. Further details of this experimental setup is discussed in [10].

Prime grade double-side-polished (DSP) *p*-type Si (100) wafers were used in this study. Partial wafers were cleaned using acetone, methanol, and isopropyl alcohol followed by nitrogen blow drying. The silver (Ag) evaporation pellets were of 99.99% purity from Kurt J. Lesker Company. The chamber base pressure was less than  $66 \times 10^{-6}$  Pa ( $0.5 \times 10^{-6}$  Torr) prior to the start of the deposition. After the initial preconditioning ramp, the final deposition rate was maintained at 0.3 nm/s. Film thickness was monitored using SQC-310 thin-film deposition controller.

Top view and cross sectional scanning electron microscope (SEM) images were acquired using Hitachi S-4800 high resolution SEM system and are shown in Figure 2. ImageJ software was used to structurally characterize morphological differences among the 300 K and 100 K grown Ag nanorod thin-film samples.

**2.2. Spectral Ellipsometry Measurements.** Ellipsometry measures the complex reflection coefficient [11]. This data is typically compared against a model of the material components to evaluate the actual parameters of the sample. In spectral ellipsometry, a broadband source is combined with a series of polarizing optics to illuminate a sample with an exact polarization state. A detector then views the specular reflectance of the sample through another polarizing optic to measure the proportion of light reflected by the sample.

The complex reflection coefficient can be described as

$$\rho_{pp} = \tan \Psi_{pp} \exp [i\Delta_{pp}], \quad (1)$$

where  $\tan(\Psi_{pp})$  is the ratio of the amplitude of light horizontally polarized over that vertically polarized, and  $\Delta_{pp}$  is the phase delay between the two orthogonal fields [12].

Fundamentally, this complex reflection coefficient relates back to the reflection Jones matrix of the sample. An element with a reflection matrix of

$$R_j = \begin{bmatrix} r_{pp} & r_{sp} \\ r_{ps} & r_{ss} \end{bmatrix} \quad (2)$$

will have a complex reflection coefficient that is equal to  $\rho_{pp} = r_{pp}/r_{ss}$ . Two other complex reflection coefficients are commonly used,

$$\begin{aligned} \rho_{sp} &= \frac{r_{sp}}{r_{ss}}, \\ \rho_{ps} &= \frac{r_{ps}}{r_{pp}}, \end{aligned} \quad (3)$$

and give new information on the relative Jones matrix. These reflection coefficients (and hence corresponding  $\Psi$  and  $\Delta$ ) can be extracted using generalized ellipsometry. Extraction methods are detailed in [13]. These additional two reflection coefficients are very important for measuring biaxial samples. A biaxial material's Jones matrix is nondiagonal everywhere

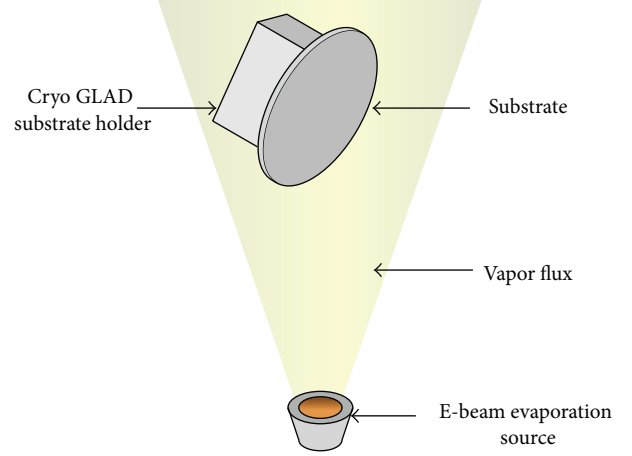


FIGURE 1: Nanorod growth experimental setup.

except for the principle axes. These extra measurements are required to properly extract the material parameters.

This data is typically measured as a function of angle of incidence,  $\psi$ , as measured from the surface normal. The reflection coefficient changes significantly given any change of material parameters, such as layer depth or surface roughness, making the measure of  $\Psi$  and  $\Delta$  over a range of angles fairly material specific.

The complex reflection coefficient, and hence  $\Psi$  and  $\Delta$ , can easily be modeled given material parameters. Because these parameters are calculated, they can be quickly varied by a computer to create a broad range of  $\Psi$  and  $\Delta$  data. These simulations are then compared to the measured data. If the modeled data and the measured data align well, it can be assumed that the sample is well described by the model.

Nanorods typically exhibit biaxial properties [3, 14–16], which means that the complex refractive index,  $n + ik$ , is not the same for every orientation or angle  $\psi$ . Biaxial materials have three principle axes ( $a, b, c$ ), each of which has a different index of refraction. In many applications, these axes do not line up with the laboratory frame of reference, which makes them difficult to measure [15]. Ellipsometric models can be set up to generate biaxial data, which can then be used to estimate the angles of these axes. Typically, these angles correspond with properties of the materials, such as the direction of the nanorods [16].

In our experiment, we found that the axis with the highest real part of the refractive index measured at the lowest sampled wavelength changed between samples. Due to the confusion of having the axes' names changing between samples, these axes are instead designated as  $\alpha$ ,  $\beta$ , and  $\gamma$ , which were chosen to correspond with the morphological characteristics of the sample and are aligned with the optical axis.  $\alpha$  corresponds with the direction of the nanorods,  $\gamma$  is perpendicular to  $\alpha$  in the plane of the substrate, and  $\beta$  is perpendicular to both  $\alpha$  and  $\gamma$ , pointing away from the surface. In other models,  $\alpha$  and  $\beta$  do not have to necessarily be perpendicular to each other. Here, they are defined as perpendicular.



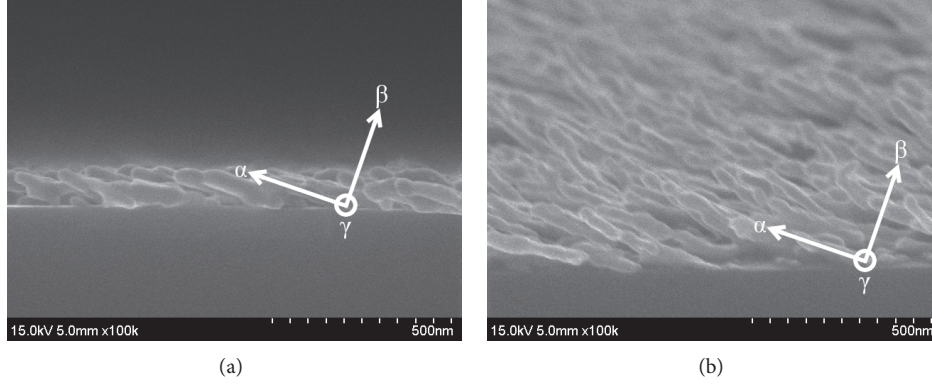


FIGURE 2: SEM images of silver nanorods. (a) Sample was grown at 300 K, while the (b) sample was grown at 100 K.

Previous studies of nanorods point to the fact that the material will have biaxial properties, and these axes typically align with the direction of the rods [17]. Knowing this, the ellipsometric measurements were taken along three directions: the plane of  $\alpha$  and  $\beta$  on the side of  $\alpha$  (also designated “INTO,” as the nanorods point towards the source), the same plane on the opposite side (also designated “AGAINST,” as the nanorods point away from the source), and the plane of the sample normal and  $\gamma$  (also designated “ACROSS,” as the nanorods are perpendicular to the source). This allows us to collect data along all three of the principle axes of the sample, which can be used to extract the relevant material parameters using an ellipsometric model. An example of the experimental setup used showing the sample orientation can be seen in Figure 3. Data collection was performed using J. A. Woollam Co.’s IR-VASE, and analysis was carried out using the associated software [18].

**2.3. Hemispherical Reflectance and Transmittance Measurements.** While ellipsometry measures specularly reflected light, light scattered at other angles can also be used to identify specific material parameters, such as absorbance. Typically, absorbance is fairly difficult to measure directly, but it can be extracted from reflectance and transmittance data. Conservation of energy states that absorbance ( $A$ ), reflectance ( $R$ ), and transmittance ( $T$ ) are related by

$$1 = A(\psi) + R(\psi) + T(\psi). \quad (4)$$

Absorbance can also be found given the  $n$  and  $k$  values of the material. Absorbance is calculated as

$$A = \exp \left[ -\frac{4\pi k}{\lambda_0} \frac{d}{\cos \theta} \right], \quad (5)$$

where  $\lambda_0$  is the free-space wavelength,  $d$  is the material thickness, and  $\theta$  is the angle of propagation within the sample. Because  $k$  is divided by  $\lambda_0$ , samples will have high absorbance when they have lower  $k$  (but  $>0$ ) values at shorter wavelengths or higher  $k$  values at longer wavelengths.

Reflectance and transmittance measurements were made using Surface Optics Corp.’s SOC-100 which measures hemispherical directional reflectance (HDR) and hemispherical

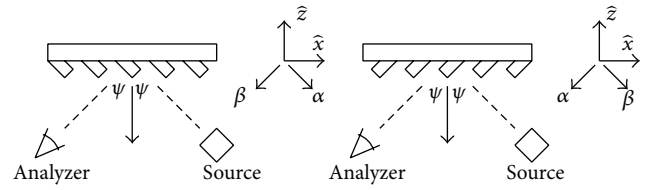


FIGURE 3: Ellipsometry experimental setup. The diagram on the left demonstrates the orientation “INTO,” while the diagram on the right demonstrates the orientation “AGAINST.”

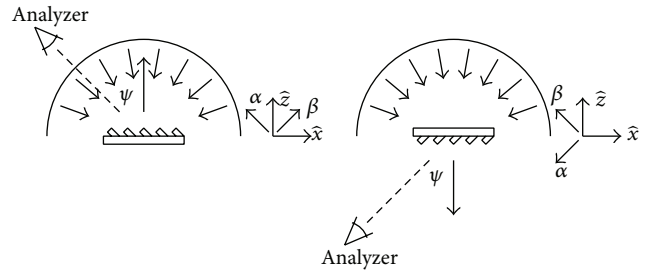


FIGURE 4: Reflectance (left) and transmittance (right) experimental setup. Both diagrams show the orientation “INTO.”

directional transmittance (HDT). Because of this, special care must be taken to ensure proper measurement of these nanorod samples. The sample must be mounted upside down relative to the reflectance measurement to properly measure the transmittance of the sample. This is shown in Figure 4.

### 3. Results and Discussion

**3.1. Sample Characteristics.** Figure 2 showed the top and side view SEM images for 300 K and 100 K grown Ag nanorod thin films. The distinct morphological differences in the structure of these films are evident from these images. The nanostructure of 300 K grown films is in agreement with previously reported results in literature [19, 20]. Compared to 300 K, 100 K grown thin films appear to have distinctly separate nanorods with smaller diameter. The 300 K sample has partially collapsed nanostructure with larger-diameter



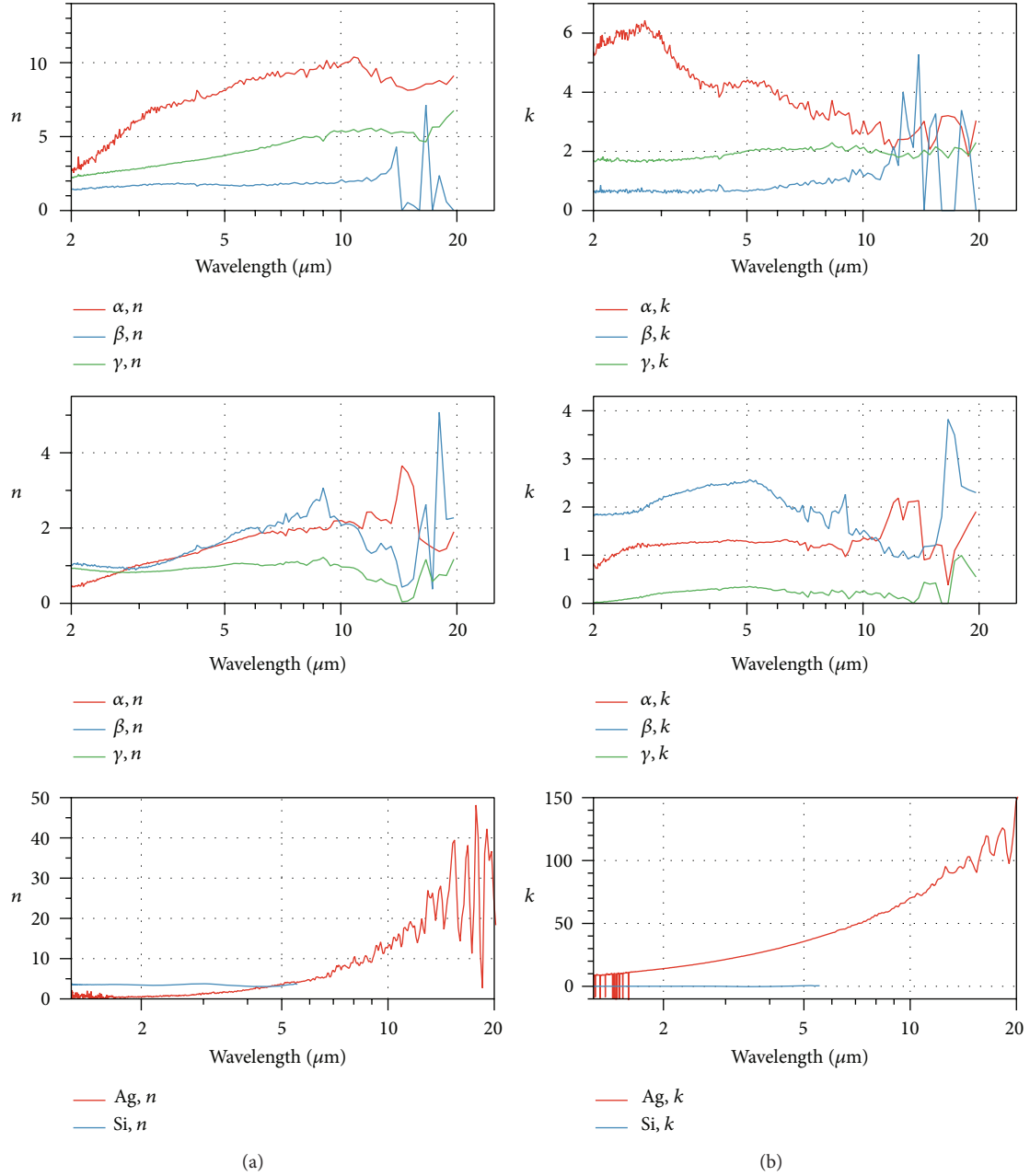


FIGURE 5: Measured  $n$  (a) and  $k$  values (b). Sample grown at 300 K is shown on top, while the sample grown at 100 K is shown in the middle.  $\alpha$  corresponds with the direction of the nanorods,  $\gamma$  is the perpendicular of  $\alpha$  lying in the plane of the sample, and  $\beta$  is the perpendicular to the two previous vectors. The  $n$  and  $k$  values extracted for the Si substrate and Ag deposition are shown at the bottom.

nanorods. This fact is not obvious unless the structure of the film is investigated using cross sectional view. Based on the observed differences in the diameter, length, number of nanorods per unit area, and nanorod spacing, it appears that the available Ag nanostructured surface area of the 100 K films will be larger than that of the 300 K grown thin films. Therefore, it is expected that the 100 K and 300 K grown thin films will exhibit different plasmonic, optical, electrical, and mechanical properties. The difference in the evolution of thin films and quantitative morphological differences of

these films is discussed in our previously reported study [10].

**3.2. Optical Constant Extraction.** The  $n$  and  $k$  values extracted along the principle axes are shown in Figure 5. The structure of the nanorods obviously has a strong impact on the overall characteristics of the metamaterial as a whole. Neither sample exhibits any behavior that can be attributed to a simple layered material model. These values were extracted by fitting the measured data to a biaxial layered model (summarized

TABLE 1: Modeling parameters and measurements for both sample grown at 300 K and sample grown at 100 K.

	300 K sample		100 K sample	
	Model parameter	SEM measurement	Model parameter	SEM measurement
Layer depth (nm)	135 nm	128 nm–160 nm	115 nm	110 nm–120 nm
Nanorod angle (deg.)	84°	68°–72°	84°	68°–72°

in Table 1). Given the average film thickness (taken from the SEM images),  $n$  and  $k$  were varied to match the collected generalized ellipsometry data.

Both samples exhibit clear anisotropic behavior. The effective index changes considerably as a function of the orientation and the angle  $\psi$ . More significantly, each sample demonstrates unique behavior, indicating that the subwavelength structures are responsible for the material's response. Both sets of nanorods have complex indexes significantly higher than that of the substrate and significantly lower than that of the Ag deposition (also shown in Figure 5).

The 300 K sample has an index that is highest along the direction of the nanocolumns. This behavior has been observed in other nanorod samples at shorter wavelengths [9]. This index has a high complex component, which would imply that the absorptance in this direction would be comparatively higher. The complex portion decreases sharply towards  $5\ \mu\text{m}$ , where it approaches the behavior of the other two axes.

The 100 K sample has a much different behavior. Here, the index along the  $\alpha$  axis starts lower than the other two, then increases to approximately the behavior of the  $\beta$  axis. This behavior has also been observed in other nanorod samples [16]. This axis has a complex part of the index that is lower than the  $\beta$  axis, which is contrary to the 300 K sample. The real portion of the index along  $\alpha$  crosses the  $\gamma$  index at  $2.65\ \mu\text{m}$  and crosses the  $\beta$  at both  $2.82\ \mu\text{m}$  and  $3.75\ \mu\text{m}$ .

While both of these behaviors have been noted before, these samples are novel because they exhibit both behaviors. The most significant difference between the two samples is the nanostructures, implying that this difference is responsible for this unique behavior.

These two structures have significantly different effective optical constants. The optical axes of these materials always roughly align with the morphological characteristics of the sample, which is why the  $\alpha$ ,  $\beta$ , and  $\gamma$  axes were chosen instead of the typical  $n_a$ ,  $n_b$ , and  $n_c$  axes found in similar papers. Choosing these axes allows for a much clearer comparison between the two samples.

Similar structures have been well described using a Bruggeman effective medium approximation [6]. Typically, this kind of film would be a silver and void mixture with a void fraction percentage likely around 70% with some depolarization factor. For our particular sample, these parameters were not of great importance; the effective index of the material was needed to correlate with the measured absorptance data.

The orientation of the optical axes was easily extracted for both samples and is shown in Figure 2. For the 300 K sample, the orientation of the  $\alpha$  axes is located at  $83.76^\circ$  from normal. Fitting placed  $\gamma$  at  $89.9^\circ$  from normal and  $\beta$  axis at  $6.21^\circ$  from normal, on the opposite side of the  $\alpha$  axis. This confirms that

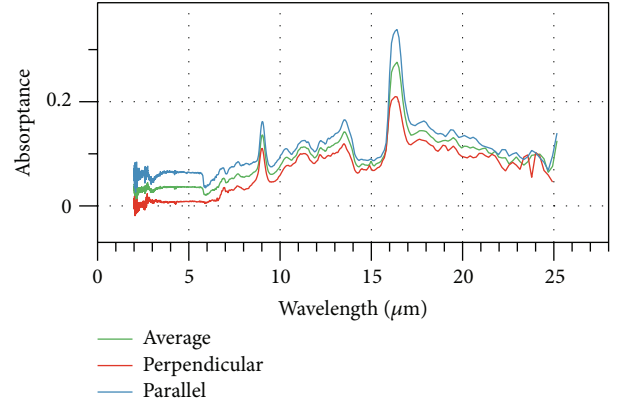


FIGURE 6: Polarization-based absorptance for Si substrate.

the  $\gamma$  axis is in the plane of the sample. Similarly, for the 100 K sample, the orientation of the  $\alpha$  axis was located at  $83.89^\circ$  from normal. The  $\beta$  axis is oriented at  $8.26^\circ$  from normal.  $\gamma$  axis is a bit further from the plane of the substrate, oriented  $5.53^\circ$  above the plane of the sample.

**3.3. Absorptance Calculations.** The absorptance is calculated using (4) with the reflectance and transmittance measurements. The absorptance of the Si substrate is shown in Figure 6. The absorptance of the substrate shows that two peaks inconsistent with the ellipsometric data discussed in Section 3.2. The peaks occurring at  $9\ \mu\text{m}$  and  $16\ \mu\text{m}$  are due to interstitial oxygen present in the Si. This is commonly found in silicon grown by Czochralski method [21].

Note that the absorptance is polarization dependent. This is due to the difference in reflectance between the two orthogonal states; the perpendicular polarization state is prevented from exiting the material. The reflected portion of the energy passes through the layer again, where it has another chance to be absorbed, which in turn leads to a higher absorptance.

The spectral reflectance and transmittance measurements of the samples are shown in Figure 7. The 300 K sample has a significantly lower reflectance than the 100 K sample. The “INTO” orientation reflects significantly better than the “AGAINST” orientation; the “AGAINST” and “ACROSS” transmittance measurements are nearly identical for this sample; and the “INTO” orientation transmits better at longer wavelengths.

The 100 K sample has clearly different reflectance and transmittance properties (Figure 7(b)). All three orientations have very similar characteristics, with the “ACROSS” orientation showing slightly higher reflectance. For transmittance,

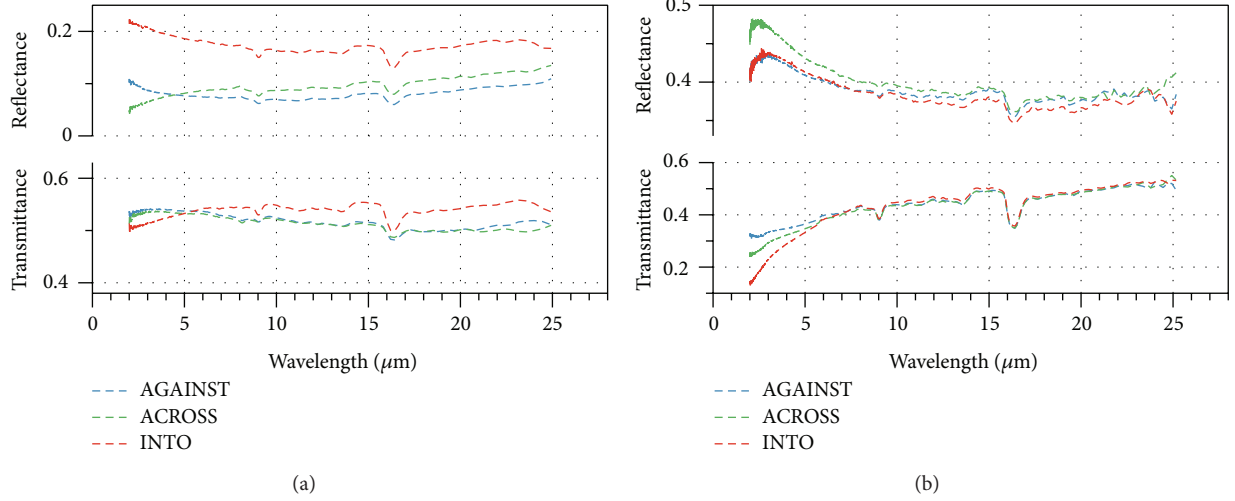


FIGURE 7: Reflectance and transmittance measurements for unpolarized light at  $\psi = 70^\circ$ . (a) Sample was grown at 300 K, while the (b) sample was grown at 100 K.

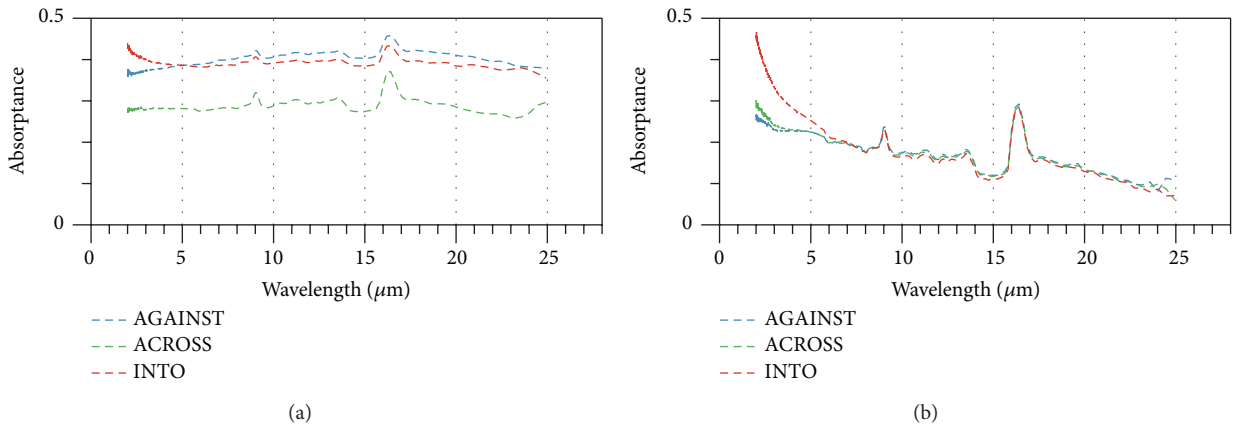


FIGURE 8: Absorbance measurements for unpolarized light at  $\psi = 70^\circ$ . (a) Sample was grown at 300 K, while the (b) sample was grown at 100 K.

all three measurements are nearly identical after about  $7 \mu\text{m}$ . For the shorter wavelengths, there is a large difference between the “AGAINST” and “INTO” orientations, contrary to what was observed in the 300 K sample.

The absorbance measurements show a significant difference between the two samples. These measurements are shown in Figure 8. The sample grown at 300 K absorbs light over the infrared wavelength range significantly better than the sample grown at 100 K. The “INTO” absorbance is slightly higher than the “AGAINST” absorbance at wavelengths lower than about  $5 \mu\text{m}$ . This measurement corresponds well to the indices presented in Figure 5. For example, the imaginary portion of the index along  $\gamma$  is very low, which matches very well with the much lower absorbance for the “ACROSS” measurement.

For the 100 K sample, all three orientations have nearly identical absorbance at wavelengths longer than about  $6 \mu\text{m}$ . At shorter wavelengths, the “INTO” orientation has a much stronger absorbance than the other two orientations. This

is a characteristic shared by both samples. “ACROSS” and “AGAINST” have very similar absorbances throughout the entire range of wavelengths examined here. Again, this matches well with the indices in Figure 5. The  $\alpha$  axis has a much higher imaginary index, correlating with the higher absorbance.

The absorbance measurement can also be decomposed into separate polarization states. This is shown in Figure 9. Additional measurements (not shown here) show that the differences are due to an inability for the sample to transmit the parallel (TM) polarization state. Normally, this state is easily transmitted through the sample. The inability to transmit this energy, which has already been coupled into the material, manifests as increased absorbance for this polarization state.

Furthermore, the polarization-based absorbance displays some unique characteristics. The absorbance shows a very clear polarization dependence of the 300 K material. In all orientations, the parallel polarization is most strongly

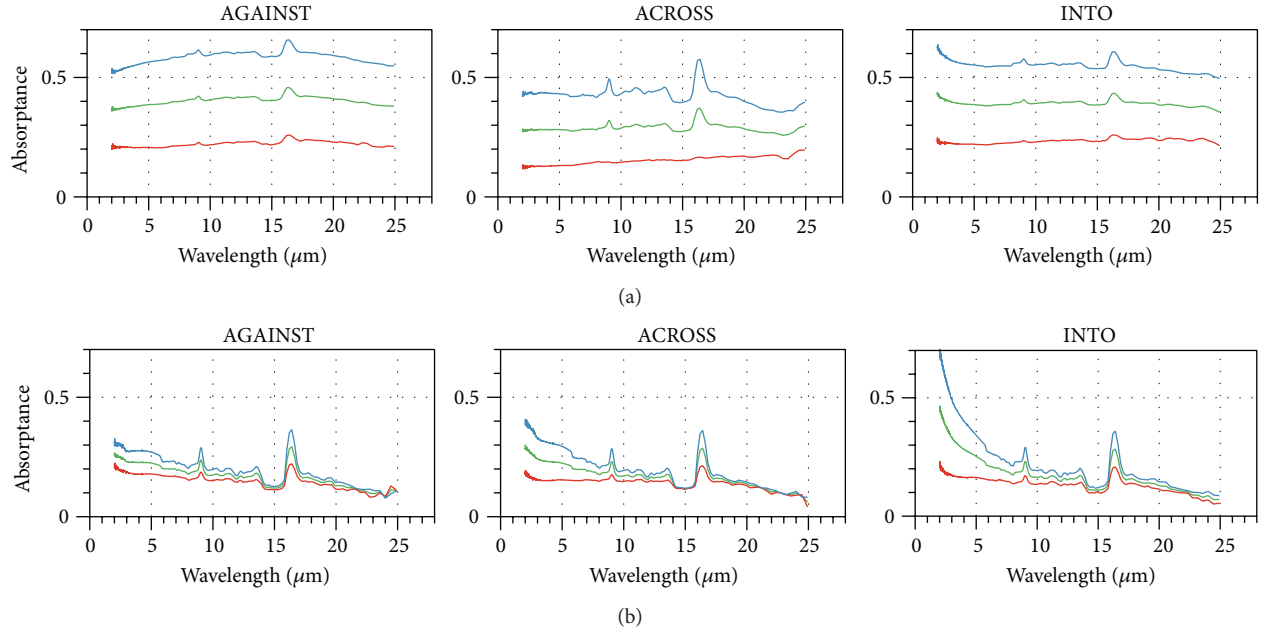


FIGURE 9: Polarization-based absorbance for the sample grown at 300 K (a) and 100 K (b). Blue is the parallel (TM) polarization state and red is the perpendicular (TE) polarization state. The green line is unpolarized.

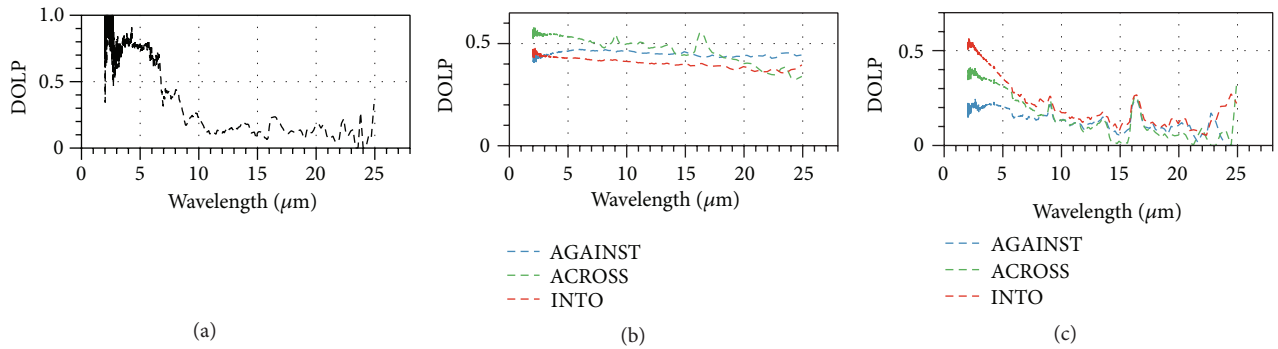


FIGURE 10: DOLP measurement for Si substrate (a), sample grown at 300 K (b), and sample grown at 100 K (c).

absorbed. The “INTO” absorbance shows the least difference between polarizations, likely due to the light being incident on the top of the nanorods. Because of the cylindrical symmetry, there is very little difference between polarization states. This would explain the lower degree of linear polarization (DOLP) for this orientation in Figure 10.

The “AGAINST” orientation shows the highest difference in absorbance between polarization states. In this case, the direction of the incident light is normal to the nanorods, which would explain why the two polarization states interact with the material so differently. “ACROSS” shows similar trends to the other two orientations, but to a lesser degree.

The polarization-based absorbance data for the sample grown at 300 K shows very little polarization-based absorbance (Figure 9(a)). All three orientations have similar DOLP values in Figure 10, averaging around 0.5. These values are very different than the DOLP for the Si substrate, also shown

in Figure 10, which averages around 0.75 between 2 and 7  $\mu\text{m}$  and then drops to around 0.25.

#### 4. Conclusion

These Ag nanorod thin films have exhibited strong metamaterial properties in the sense that they are well described by an effective medium approximation. Glancing angle deposition at cryogenic temperatures created a nanorod sample that has significantly different morphological properties than a similar sample grown at room temperature. Ellipsometry reveals that these two samples have greatly varying optical properties. Notably, the optical axis with the highest refractive index changed places with respect to the axes defined by the morphological features of the nanorods between the samples. The 300 K sample demonstrates a much higher set of indices than does the 100 K sample. The 100 K has significantly

different behavior than that of the 300 K sample. The absorbance of both samples has been measured. Absorbance measurements correspond well with the measured material indices. The 100 K sample exhibits a much lower difference in absorbance at wavelengths longer than  $6\ \mu\text{m}$ , while showing its absorbance is strongly orientation dependent in the shorter wavelengths. The 300 K sample shows a smaller orientation dependence, but across the entire infrared band. These measurements show the impact of the subwavelength structures on the observable optical properties of nanorod metamaterials.

## Conflict of Interests

The authors declare that there is no conflict of interests regarding the publication of this paper.

## References

- [1] S.-H. Hsu, E.-S. Liu, Y.-C. Chang et al., "Characterization of Si nanorods by spectroscopic ellipsometry with efficient theoretical modeling," *Physica Status Solidi A: Applications and Materials Science*, vol. 205, no. 4, pp. 876–879, 2008.
- [2] G. Beydaghyyan, C. Buzea, Y. Cui, C. Elliott, and K. Robbie, "Ex situ ellipsometric investigation of nanocolumns inclination angle of obliquely evaporated silicon thin films," *Applied Physics Letters*, vol. 87, no. 15, Article ID 153103, pp. 1–3, 2005.
- [3] D. Schmidt, B. Booso, T. Hofmann, E. Schubert, A. Sarangan, and M. Schubert, "Monoclinic optical constants, birefringence, and dichroism of slanted titanium nanocolumns determined by generalized ellipsometry," *Applied Physics Letters*, vol. 94, no. 1, Article ID 011914, 2009.
- [4] A. V. Kabashin, P. Evans, S. Pastkovsky et al., "Plasmonic nanorod metamaterials for biosensing," *Nature Materials*, vol. 8, no. 11, pp. 867–871, 2009.
- [5] W. U. Huynh, J. J. Dittmer, and A. P. Alivisatos, "Hybrid nanorod-polymer solar cells," *Science*, vol. 295, no. 5564, pp. 2425–2427, 2002.
- [6] D. Schmidt, "Characterization of highly anisotropic three-dimensionally nanostructured surfaces," *Thin Solid Films*, 2013.
- [7] D. Liang, D. Schmidt, H. Wang, E. Schubert, and M. Schubert, "Generalized ellipsometry effective medium approximation analysis approach for porous slanted columnar thin films infiltrated with polymer," *Applied Physics Letters*, vol. 103, no. 11, pp. 111906–111906, 2013.
- [8] K. B. Rodenhausen, D. Schmidt, T. Kasputis, A. K. Pannier, E. Schubert, and M. Schubert, "Generalized ellipsometry in-situ quantification of organic adsorbate attachment within slanted columnar thin films," *Optics Express*, vol. 20, no. 5, pp. 5419–5428, 2012.
- [9] D. Schmidt and M. Schubert, "Anisotropic bruggeman effective medium approaches for slanted columnar thin films," *Journal of Applied Physics*, vol. 114, no. 8, Article ID 083510, 2013.
- [10] P. J. Shah, X. Niu, and A. M. Sarangan, "High aspect ratio silver nanorod thin films grown at cryogenic substrate temperature," *Journal of Nanoscience Letters*, vol. 3, article 19, 2013.
- [11] J. A. Woollam, B. D. Johs, C. M. Herzinger, J. N. Hilfiker, R. A. Synowicki, and C. L. Bungay, "Overview of variable-angle spectroscopic ellipsometry (vase): I. basic theory and typical applications," in *Optical Metrology*, vol. 1 of *Proceedings of SPIE*, pp. 3–28, 1999.
- [12] D. H. Goldstein, *Polarized Light, Revised and Expanded*, vol. 83, CRC Press, 2003.
- [13] M. Schubert, B. Rheinländer, J. A. Woollam, B. Johs, and C. M. Herzinger, "Extension of rotating-analyzer ellipsometry to generalized ellipsometry: Determination of the dielectric function tensor from uniaxial  $\text{TiO}_2$ ," *Journal of the Optical Society of America A: Optics and Image Science, and Vision*, vol. 13, no. 4, pp. 875–883, 1996.
- [14] J. F. Elman, J. Greener, C. M. Herzinger, and B. Johs, "Characterization of biaxially-stretched plastic films by generalized ellipsometry," *Thin Solid Films*, vol. 313–314, pp. 814–818, 1998.
- [15] M. Schubert and W. Dollase, "Generalized ellipsometry for biaxial absorbing materials: Determination of crystal orientation and optical constants of  $\text{Sb}_2\text{S}_3$ ," *Optics Letters*, vol. 27, no. 23, pp. 2073–2075, 2002.
- [16] D. Schmidt, A. C. Kjerstad, T. Hofmann, R. Skomski, E. Schubert, and M. Schubert, "Optical, structural, and magnetic properties of cobalt nanostructure thin films," *Journal of Applied Physics*, vol. 105, no. 11, Article ID 113508, 2009.
- [17] D. Schmidt, B. Booso, T. Hofmann, E. Schubert, A. Sarangan, and M. Schubert, "Generalized ellipsometry for monoclinic absorbing materials: determination of optical constants of Cr columnar thin films," *Optics Letters*, vol. 34, no. 7, pp. 992–994, 2009.
- [18] J. A. Woollam, *Ellipsometry, Variable Angle Spectroscopic*, Wiley Encyclopedia of Electrical and Electronics Engineering, 2000.
- [19] Y.-J. Jen, A. Lakhtakia, C.-W. Yu, and C.-T. Lin, "Vapor-deposited thin films with negative real refractive index in the visible regime," *Optics Express*, vol. 17, no. 10, pp. 7784–7789, 2009.
- [20] K. R. Beavers, N. E. Marotta, and L. A. Bottomley, "Thermal stability of silver nanorod arrays," *Chemistry of Materials*, vol. 22, no. 7, pp. 2184–2189, 2010.
- [21] *Interstitial Oxygen*, Sunedison, 2013.



## Research Article

# Formation and Evolution Mechanism of Plasmon Resonance from Single Ring-Shaped Nanotube to Dimer and Arrays

F. Q. Zhou,<sup>1</sup> Z. M. Liu,<sup>1,2</sup> H. J. Li,<sup>2</sup> Z. F. Liu,<sup>1</sup> B. Tang,<sup>3</sup> and X. Zhou<sup>4</sup>

<sup>1</sup> College of Sciences, East China Jiaotong University, Nanchang 330013, China

<sup>2</sup> College of Physics Science and Technology, Central South University, Changsha 410083, China

<sup>3</sup> School of Mathematics and Physics, Changzhou University, Changzhou 213164, China

<sup>4</sup> School of Sciences, Hunan University of Technology, Zhuzhou 412008, China

Correspondence should be addressed to Z. M. Liu; liuzhimin2006@163.com

Received 8 October 2013; Accepted 7 January 2014; Published 2 April 2014

Academic Editor: Clare C. Byeon

Copyright © 2014 F. Q. Zhou et al. This is an open access article distributed under the Creative Commons Attribution License, which permits unrestricted use, distribution, and reproduction in any medium, provided the original work is properly cited.

The formation and evolution mechanisms of plasmon resonance from single Ring-shaped nanotube to dimer and arrays are studied; an attempt has been made to bridge the gap between single-tube, dimer, and array. Results show that resonant modes can be divided into three types: quadrupole, hexapole, and octupole resonance from visible to near infrared region, and each mode maintains relatively stable resonant characteristics, but the optical transmission properties including redshift and blueshift of the modes and band gap are highly tunable by adjusting the number of nanotube and intertube spacing values. The field-interference mechanism has been suggested to explain the physical origin.

## 1. Introduction

Surface plasmon (SP) stems from the coupling between metallic nanostructures and light and great interest has been aroused for its rich physical phenomena, mechanisms, and potential application [1–4].

The studies on single metallic nanostructures include nanospheres [5], nanoprisms [6], nanorods [7], nanocubes [8], and shells [9]. The results show that the plasmonic properties depend strongly on the size and shape of the nanostructure and material properties of the surrounding medium.

Coupled metallic nanoparticle pairs are referred to as plasmonic “dimer” [10]. The effects of symmetry breaking on plasmon resonance of dimer have been analyzed in many works [11, 12], and the “hot spots” may be formed by the pair of closely spaced nanoparticles and caused by the strong coupling interactions between the near fields of two closely spaced nanoparticles [11, 13].

A nanosystem such as nanowire with nanoparticle [14, 15], nanoparticles array [16], and nanowires chain systems [17, 18] is interesting for the interactions of plasmon modes

between the individual nanostructures [19]. In addition, arrays of nanostructures can also be used as optical waveguides [20–22]. Many efforts focused on the optical transmission properties of simple nanoparticles such as spherical particles and nanotube arrays [23–28].

Single nanostructure, dimer, and arrays have been highly studied, respectively. And the above researched nanostructures such as circular-shell-core nanoparticle or nanotube are the common structure; the metallic Ring-shaped nanotube and its array have not been discussed comprehensively; and the existence of length  $L$  of the Ring-shaped nanotube (shape of nanotube) influences greatly the transmission spectrum and plasmon resonance. In addition, we want to research the formation and evolution mechanisms of plasmon resonance between single particle, dimer, and array.

Based on the above analysis, in this paper, we propose single Ring-shaped nanotube, dimer, and arrays and discuss its optical transmission properties by using Finite-Difference Time-Domain (FDTD) method. First, we make a simple comparison between the Circular-shaped and Ring-shaped nanotube arrays. Then, from the transmission spectra of the simulation results, we can see the formation and evolution

process of the regularly resonant transmission modes and band gap. A field-interference mechanism has been suggested and investigated. In addition, the transmission properties have been further characterized with various intertube spacing between adjacent nanotubes. The present study has led to an improved understanding of the formation and evolution of plasmon resonant modes in nanostructures, and the proposed models and results may have great potential applications in subwavelength near-field optics.

## 2. Model and Method

Figure 1 shows schematically two-dimensional Ring-shaped nanotube with infinite length along the  $z$  direction. Figure 1(a) is the single-tube, in the whole paper, the outer radius, inner radius, and the length of the Ring-shaped nanotube are fixed  $R_1 = 50$  nm,  $R_2 = 40$  nm, and  $L = 100$  nm, respectively. A nanodimer composed by two nanotube pairs is shown in Figure 1(b), and the intertube spacing between adjacent nanotubes can be changed by varying the parameter  $D$ . Further, the array of ten nanotubes is depicted in Figure 1(c). In addition, the metal is chosen to be Au. The relative permittivities of the gold are approximated by the Drude model, which is defined as  $\epsilon(\omega) = 1 - \omega_p^2/(\omega^2 + i\omega\gamma_p)$ , where  $\omega_p = 1.37 \times 10^{16} \text{ s}^{-1}$  is the bulk plasmon frequency and  $\gamma_p = 4.08 \times 10^{13} \text{ s}^{-1}$  represents the electron relaxation time [29]. The outside and inner-core outside dielectric medium of Ring-shaped nanotube are defined as air; the dielectric constant is  $\epsilon = 1$ .

We use two-dimensional FDTD [30] method to simulate the structure with a lattice of  $L_x \times L_y = 1800 \text{ nm} \times 300 \text{ nm}$  for single-tube, dimer, and array, and infinity along the  $z$  direction, and the spatial mesh and time steps are set as  $\Delta_x = \Delta_y = 1 \text{ nm}$  and  $\Delta t = \Delta x/2c$ , where  $c$  is the velocity of light in vacuum. The left and right surfaces of the calculated region along the  $x$  direction are truncated by perfectly matched layer (PML) absorbing boundary conditions, and due to the periodicity of the structure along  $y$  direction, the top and bottom boundaries along  $y$  direction are treated by periodic boundary conditions. A Gaussian single pulse of light with a wide frequency profile is sent along the  $x$  direction with TM polarization.

## 3. The Differences between the Circular-Shaped and Ring-Shaped Nanotube Arrays

Let us make a simple comparison between the Circular-shaped and Ring-shaped nanotube arrays. We fix the outer radius  $R_1 = 50$  nm, inner radius  $R_2 = 40$  nm, and separation distance of tubes  $D = 20$  nm both for Circular-shaped and Ring-shaped nanotube arrays and set length  $L = 100$  nm of the Ring-shaped nanotube.

The transmission spectrum of the band structure can be formed in both the Circular-shaped and the Ring-shaped nanotube arrays. From Figure 2(a), we can see that only one forbidden band has been formed in range from 428 nm to 577 nm, and it shows that the resonant peaks on the left side are dense and irregular, while the resonant peaks on

the right side are regular. While two forbidden bands form in-transmission spectrum of the Ring-shaped nanotube array, which is showed in Figure 2(b), the right forbidden band is very wide ranging from 680 nm to 1000 nm, the left forbidden band is narrow ranging from 370 nm to 500 nm, and five regular resonant peaks appear between the two forbidden bands. From the results, we can find that the existence of length  $L$  of the Ring-shaped nanotube influence greatly the transmission spectrum and plasmon resonance; the details of resonant properties of Ring-shaped nanotube are studied in next sections. This is why we choose this structure.

## 4. Numerical Results and Discussion: Formation and Evolution Mechanisms of Plasmon Resonance

First of all, we fix the outer radius  $R_1 = 50$  nm, inner radius  $R_2 = 40$  nm, and separation distance of tubes  $D = 20$  nm and discuss the effect of the tube number  $N$  on optical transmission properties and then study the formation and evolution mechanisms of plasmon resonance from single Ring-shaped nanotube to dimer and array. The transmission spectrum with different numbers  $N = 1, 2, 10$  are shown in Figures 3(a)–3(c), namely, the single-tube, dimer, and array, respectively. We find some features by comparing Figures 3(a)–3(c). First, the resonant modes can be grouped into three types. Type 1 is quadrupole resonance including the peaks of A1, A2, and A3, and the Type 2 peaks B1, B2, and B3 belong to hexapole resonance; the Type 3, C1, C2, and C3, is octupole resonance; we will discuss the multipole resonant properties by simulating the electric field distributions in next chapter. Second, from Figure 3, we can find that the properties of the three types of modes exhibit certain regularity with  $N$  increasing. When only the single-tube system is considered, the higher-order modes are excited in the visible and near infrared region, just like the resonant peaks B1 and C1, while the quadrupole resonance peak A1 stays away from this area and distributes in infrared region (not shown here). Then, we take into account the dimer system; due to the coupling effect between nanotube pairs, quadrupole resonance peak A2 gradually forms in near infrared region; we also consider that quadrupole resonance peak A2 blueshifts into near infrared region. At the same time, the higher-order modes B1 and C1, the dip between B1 and C1, and the dip on the right B1 redshift. It is more important that the transmission band begins to form; forbidden band can clearly be seen in the transmission spectra from Figure 3(b). As shown in Figure 3(c), due to the coupling effect between each nanotube, regular quadrupole resonance peak A3 and hexapole resonance peak B3 establish; for example, six hexapole resonance peaks B3 appear. In addition, two wide forbidden bands have been formed, the right forbidden band ranges from 680 nm to 1000 nm, the left band gap is smaller than the right, and it ranges from 380 nm to 500 nm. The formation and evolution process is similar to the forming process of band lines in photonic crystal, which can be used to design an optical filter.

In order to analyse the basic physical mechanisms for above phenomena, we plot the electric field distributions  $E_x$



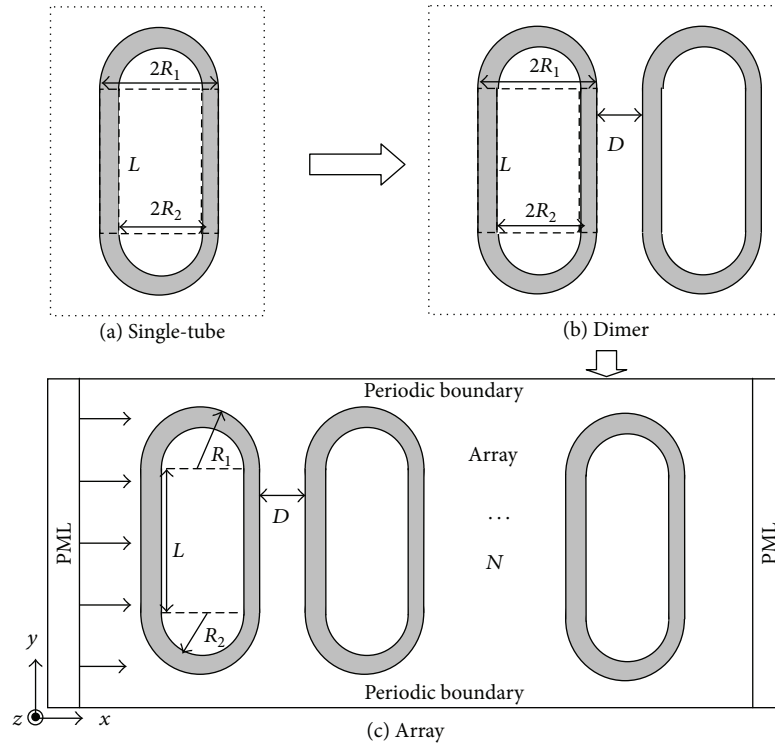


FIGURE 1: A unit cell of the Ring-nanotube (a) single-tube; (b) dimer; (c) array.

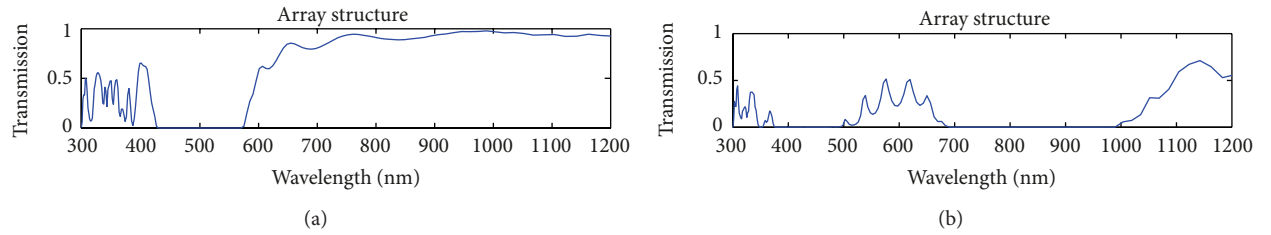


FIGURE 2: Transmission spectra through the Circular-shaped (a) and Ring-shaped (b) nanotube arrays as a function of wavelength.

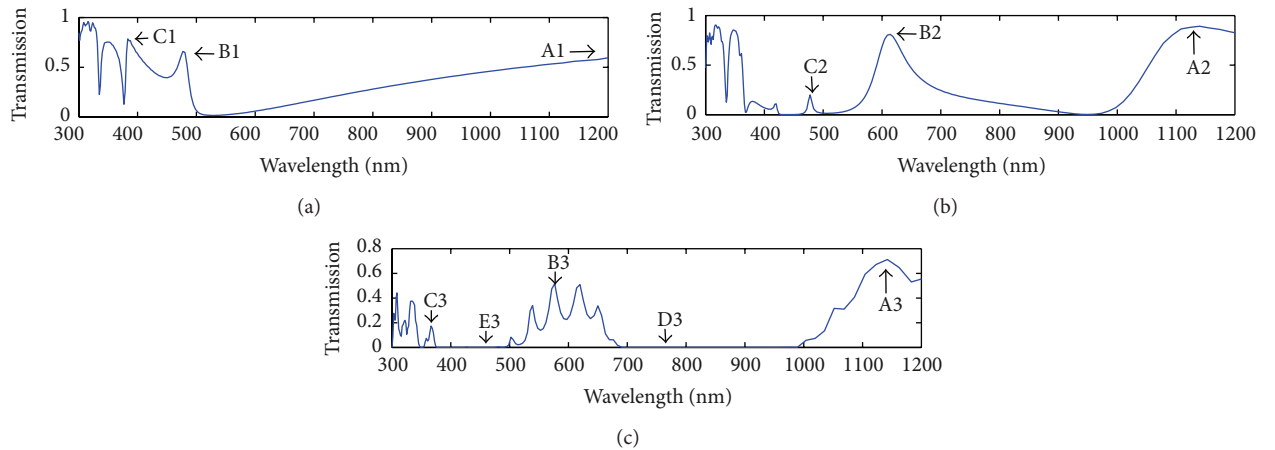


FIGURE 3: Transmission spectra for single-tube (a); dimer (b); array (c).

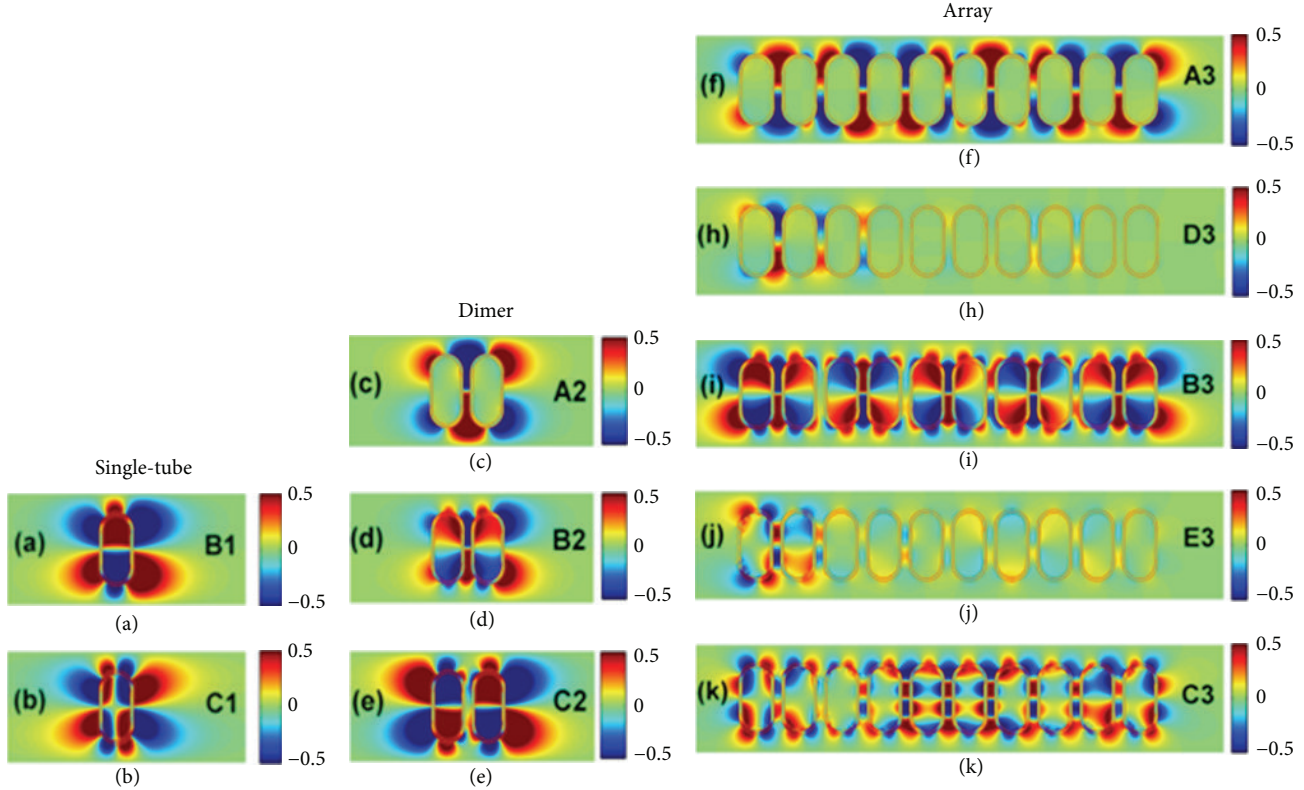


FIGURE 4: The field distributions of  $E_x$  at the transmission peaks and band gap (A, B, C, D, and E) are labeled in Figure 2, left column for single-tube, middle column for dimer, and right column for array.

at the transmission peaks B1 and C1 for single-tube in Figures 4(a) and 4(b); transmission peaks A2, B2, and C2 for dimer in Figures 4(c)–4(e) and transmission peaks A3, B3, and C3 and band gap D3 and E3 for array in Figures 4(f)–4(k) and the corresponding peaks have been labeled in Figure 3, respectively. We consider that red colored areas represent positive and blue means negative.

First, we can find that positive and negative electric field  $E_x$  spread alternately near the edges of the nanotube from the left column of Figures 4(a) and 4(b). Figure 4(a) shows that the left sign of  $E_x$  is the same of the right, while they are opposite on the top and bottom for single nanotube, and electric field also exists in the middle and inner of the tube; its sign is opposite to the left and right. We consider that it is a hexapole field distribution for the plasmon modes in the nanotubes. It is the reason that we regard this transmission peaks as the peaks of Type 2 hexapole resonance in Figure 2. In addition, Figure 4(b) depicts the octupole resonance at the Type 3 C1 in Figure 3, but the signs of the top and bottom, left and right, and outside and inner change alternately. Besides, we can see analogous hexapole and octupole resonant patterns in the dimer and array, which are shown in Figures 4(d) and 4(e) for B2 and C2 and Figures 4(i) and 4(k) for B3 and C3. The only difference is that some of the nanotubes form a group; this phenomenon is particularly evident in Figure 4(i) B3, where each of the two tubes forms a group, and five groups appear totally.

Second, Figure 4(c) for A2 and Figure 4(f) for A3 show the quadrupole resonance; the electric field  $E_x$  distributes nearly outside of the tube, and we could barely see the electric field inner of the tube. The signs of the surface charges at two sides of the gap are opposite; the electric fields between two nanotubes are coupled together closely and intensified, which is just in analogy with a simple capacity device, so the field distributions are mostly concentrated at every other gap between adjacent nanotubes [24–26]. The results indicate that the oscillation of charge density exists between the nanotubes. In other words, the surface plasmon wave really exists and propagates along the surface. Due to the nanotube with different lengths that may be used as chain waveguides, the understanding of the plasmonic behaviors in coupled nanotubes of arrays is especially important [24].

Last, we draw the spatial distributions of the  $E_x$  at wavelengths of band gap D3 and E3, which are depicted in Figures 4(h) and 4(j); electric field only emerges on left several tubes. No excitation of resonant mode exists owing to the forbidden band gap, and incident light cannot transmit.

Successively, we investigate the effect of different spacing intertube on transmission spectrum and electric field distributions.

Firstly, the transmission spectra varying intertube spacing between adjacent nanotubes for dimer is shown in Figure 5(a). The transmission spectra blueshift obviously with increasing of the intertube spacing; the peak intensities of A

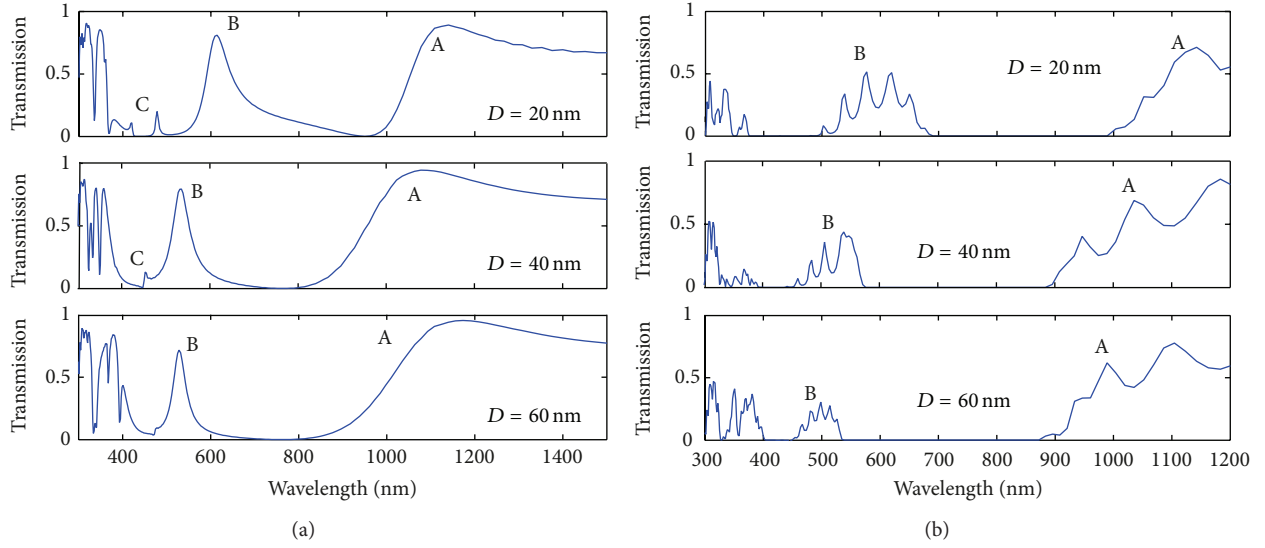


FIGURE 5: Transmission spectra with different intertube spacing in (a) dimer and (b) array.

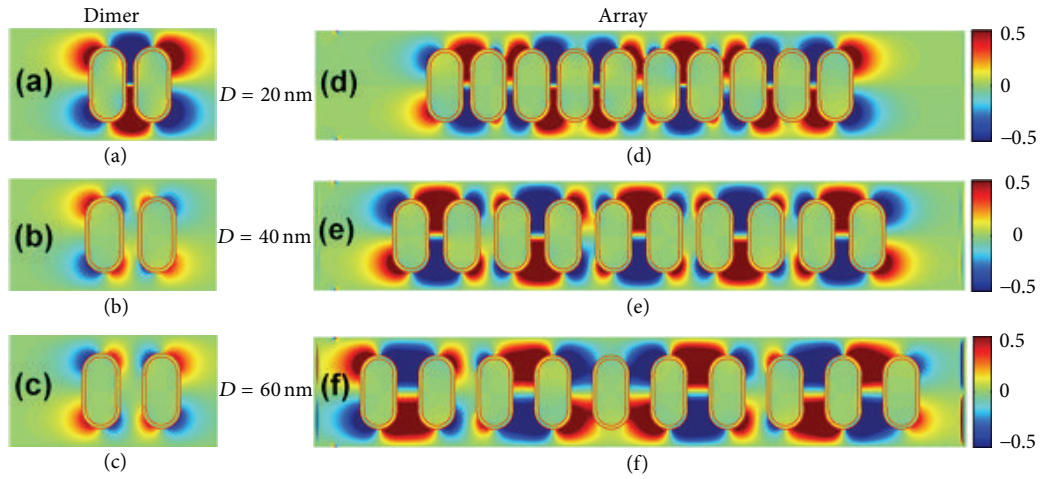


FIGURE 6: The calculated field distributions of  $E_x$  (left hand column for dimer, right hand column for array) for different intertube spacing values.

and B have no change, but the resonant peaks C decrease sharply until it disappears. At the same time, a broadband gap forms when the intertube spacing becomes  $D = 40$  nm and  $60$  nm. Besides, Figure 5(b) shows that the resonant peaks A and B are regular, while the peaks on the left side of the transmission spectra are dense and irregular for the array. As the intertube spacing increases, the transmission spectra move to the short wavelength. The number of the peaks A increases, while the number of the peaks B decreases; the width of the right band gap has no change, but the width of the left band gap is narrowed.

Secondly, the electric field  $E_x$  with different distance  $D = 20$  nm,  $40$  nm, and  $60$  nm are shown in Figure 6; the left hand column (a)–(c) is the distributions of dimer; the wavelengths  $\lambda$  of transmission peaks A labeled in Figure 5 are  $1140$  nm,  $1108$  nm, and  $1157$  nm, respectively, and the right hand column (d)–(f) is the distributions of array; the wavelengths

$\lambda$  of transmission peaks A labeled in Figure 5 are  $1134$  nm,  $1035$  nm, and  $989$  nm, respectively. During transmission peak A that is the quadrupole resonant peak, the field distributions of  $E_x$  only appear outside the nanotube. When separation distance is  $D = 20$  nm, similar to that of nanotube array [24–26], the opposing and uniform surface charges are aligned alternatively between the gap, so the field distributions are concentrated between adjacent nanotubes. As  $D = 40$  nm and  $60$  nm, the uniform surface charges are lessened due to less coupling between nanotubes. When the intertube distance gets farther apart, the uniform surface charges reduce further and the intensity of electrical field attenuates sharply. This phenomenon exists obviously in Figures 6(a)–6(c) for dimer. For the case of array, from Figures 6(d)–6(f), we can see that some of the nanotubes form a group when we increase the intertube spacing, this phenomenon is particularly evident in array, and five groups appear totally when  $D = 40$  nm, and

four groups form as  $D = 60$  nm. Due to the group formation, the electric fields  $E_x$  couple strongly with inner of each group, so we do not see that the intensity of electrical field inner of the group attenuates, but electrical field between the group attenuates evidently.

## 5. Conclusion

In conclusion, we proposed single Ring-shaped nanotube, dimer, and arrays and discussed its optical transmission properties; an attempt has been made to bridge the gap between single particle dimer, and array. Results show that the resonant modes can be divided into three types: quadrupole, hexapole, and octupole resonance from the visible to near infrared region, and each mode maintains relatively stable resonant characteristics, but the resonant transmission sensitively depends on the number of nanotubes; magnitude modification, redshift and blueshift of the resonance modes, and band gap are observed. From the transmission spectra and electric field distributions of the single nanotube to dimer and arrays, we can see the formation and evolution process of the regularly resonant transmission modes and band gap. In addition, the transmission properties of the dimer and array have been further characterized with various intertube spacing between adjacent nanotubes. The presented study not only sharpens our understanding of the formation and evolution of plasmon resonant modes in nanostructures but also provides a profound comprehension into the plasmonic interference. And we hope that the proposed models and results can be used to design structures with optimized nanophotonic devices.

## Conflict of Interests

The authors declare that there is no conflict of interests regarding the publication of this paper.

## Acknowledgments

This work was funded by the National Natural Science Foundation of China (Grants nos. 11164007, 61275174, and 61107055), the Natural Science Foundation of Jiangxi province (Grant no. 20132BAB212007), and Hunan Province of China (Grant no. 14JJ3122).

## References

- [1] P. K. Jain and M. A. El-Sayed, "Noble metal nanoparticle pairs: effect of medium for enhanced nanosensing," *Nano Letters*, vol. 8, pp. 4347–4352, 2008.
- [2] N. Felidj, J. Aubard, and G. Levia, "Optimized surface-enhanced Raman scattering on gold nanoparticle arrays," *Applied Physics Letters*, vol. 82, p. 3095, 2003.
- [3] C. Hagglund, M. Zach, G. Petersson, and B. Kasemo, "Electromagnetic coupling of light into a silicon solar cell by nanodisk plasmons," *Applied Physics Letters*, vol. 92, Article ID 053110, 2008.
- [4] C. B. Murray, S. Sun, H. Doyle, and T. Betley, "Monodisperse 3d transition-metal (Co, Ni, Fe) nanoparticles and their assembly into nanoparticle superlattices," *MRS Bulletin*, vol. 26, no. 12, pp. 985–991, 2001.
- [5] K. L. Kelly, E. Coronado, L. L. Zhao, and G. C. Schatz, "The optical properties of metal nanoparticles: the influence of size, shape, and dielectric environment," *Journal of Physical Chemistry B*, vol. 107, no. 3, pp. 668–677, 2003.
- [6] K. Munechika, J. M. Smith, Y. C. Chen, and D. S. Ginger, "Plasmon line widths of single silver nanoprisms as a function of particle size and plasmon peak position," *Journal of Physical Chemistry C*, vol. 111, no. 51, pp. 18906–18911, 2007.
- [7] W. H. Ni, X. S. Kou, Z. Yang, and J. F. Wang, "Tailoring longitudinal surface plasmon wavelengths, scattering and absorption cross sections of gold nanorods," *ACS Nano*, vol. 2, no. 4, pp. 677–686, 2008.
- [8] L. J. Sherry, S.-H. Chang, G. C. Schatz, R. P. Van Duyne, B. J. Wiley, and Y. Xia, "Localized surface plasmon resonance spectroscopy of single silver nanocubes," *Nano Letters*, vol. 5, no. 10, pp. 2034–2038, 2005.
- [9] C. M. Aguirre, T. R. Kaspar, C. Radloff, and N. J. Halas, "CTAB mediated reshaping of metallodielectric nanoparticles," *Nano Letters*, vol. 3, no. 12, pp. 1707–1711, 2003.
- [10] N. J. Halas, S. Lal, W.-S. Chang, S. Link, and P. Nordlander, "Plasmons in strongly coupled metallic nanostructures," *Chemical Reviews*, vol. 111, no. 6, pp. 3913–3961, 2011.
- [11] B. Yun, Z. Wang, G. Hu, and Y. Cui, "Theoretical studies on the near field properties of non-concentric core-shell nanoparticle dimers," *Optics Communications*, vol. 283, no. 14, pp. 2947–2952, 2010.
- [12] H. Q. Xu, H. J. Li, Z. M. Liu et al., "Effects of symmetry breaking on plasmon resonance in a noncoaxial nanotube and nanotube dimer," *Journal of the Optical Society of America A: Optics and Image Science, and Vision*, vol. 28, no. 8, pp. 1662–1667, 2011.
- [13] C. E. Talley, J. B. Jackson, C. Oubre et al., "Surface-enhanced Raman scattering from individual Au nanoparticles and nanoparticle dimer substrates," *Nano Letters*, vol. 5, no. 8, pp. 1569–1574, 2005.
- [14] H. E. Ruda and A. Shik, "Polarization and plasmon effects in nanowire arrays," *Applied Physics Letters*, vol. 90, no. 22, Article ID 223106, 2007.
- [15] H. S. Chu, W. B. Ewe, W. S. Koh, and E. P. Li, "Remarkable influence of the number of nanowires on plasmonic behaviors of the coupled metallic nanowire chain," *Applied Physics Letters*, vol. 92, no. 10, Article ID 103103, 2008.
- [16] F. Hao and P. Nordlander, "Enhanced tunability and linewidth sharpening of plasmon resonances in hybridized metallic ring/disk nanocavities," *Physical Review B*, vol. 76, Article ID 245417, 2007.
- [17] J. P. Kottmann and O. J. F. Martin, "Retardation-induced plasmon resonances in coupled nanoparticles," *Optics Letters*, vol. 26, no. 14, pp. 1096–1098, 2001.
- [18] Y.-F. Chau, H.-H. Yeh, and D. P. Tsai, "Near-field optical properties and surface plasmon effects generated by a dielectric hole in a silver-shell nanocylinder pair," *Applied Optics*, vol. 47, no. 30, pp. 5557–5561, 2008.
- [19] D. J. Wu, X. D. Xu, and X. J. Liu, "Optimization of silica-silver-gold layered nanoshell for large near-field enhancement," *Applied Physics Letters*, vol. 96, Article ID 151912, 2010.
- [20] Y.-F. Chau, H.-H. Yeh, C.-Y. Liu, and D. P. Tsai, "The optical properties in a chain waveguide of an array of silver nanoshell with dielectric holes," *Optics Communications*, vol. 283, no. 16, pp. 3189–3193, 2010.

- [21] R. Zia, J. A. Schuller, and M. L. Brongersma, "Near-field characterization of guided polariton propagation and cutoff in surface plasmon waveguides," *Physical Review B—Condensed Matter and Materials Physics*, vol. 74, no. 16, Article ID 165415, 2006.
- [22] A. F. Koenderink, R. De Waele, J. C. Prangsma, and A. Polman, "Experimental evidence for large dynamic effects on the plasmon dispersion of subwavelength metal nanoparticle waveguides," *Physical Review B—Condensed Matter and Materials Physics*, vol. 76, no. 20, Article ID 201403, 2007.
- [23] H. J. Li, Q. Liu, S. X. Xie, X. Zhou, H. Xia, and R. Zhou, "Particle plasmons resonant characteristics in arrays of strongly coupled gold nanoparticles," *Solid State Communications*, vol. 149, no. 5–6, pp. 239–242, 2009.
- [24] H. J. Li, S. L. Fu, S. X. Xie, S. Xie, X. Zhou, and J. Wu, "The optical transmission characteristics through coupled metallic nanotube arrays," *Optics Communications*, vol. 283, no. 20, pp. 3985–3988, 2010.
- [25] S. L. Fu, H. J. Li, and S. X. Xie, "Tuning of plasmonic behaviours in coupled metallic nanotube arrays," *Chinese Physics B*, vol. 20, no. 8, Article ID 087302, 2011.
- [26] Z. M. Liu, H. J. Li, H. Q. Xu, S. Xie, X. Zhou, and C. Wu, "Tunable optical transmission through square-core metallic nanotube arrays," *Optics Communications*, vol. 284, no. 13, pp. 3331–3334, 2011.
- [27] H. Q. Xu, H. J. Li, and G. Xiao, "Tunable plasmon resonance coupling in coaxial gold nanotube arrays," *Chinese Optical Letters*, vol. 11, Article ID 042401, 2013.
- [28] X. Zhou, J. S. Fang, D. W. Yang, and X. P. Liao, "Plasmon resonance coupling in strongly coupled gold nanotube arrays with structural defects," *Chinese Physical B*, vol. 21, no. 8, Article ID 084202, 2012.
- [29] E. D. Palik, *Handbook of Optical Constants in Solids*, Academic Press, Boston, Mass, USA, 1982.
- [30] A. Taflov and S. C. Hagness, *Computational Electrodynamics: The Finite-Difference-Time-Domain Method*, Artech House, Boston, Mass, USA, 2nd edition, 2000.



## Research Article

# Effects of Hydrogen on the Optical and Electrical Characteristics of the Sputter-Deposited $\text{Al}_2\text{O}_3$ -Doped ZnO Thin Films

Fang-Hsing Wang,<sup>1</sup> Cheng-Fu Yang,<sup>2</sup> Jian-Chiun Liou,<sup>3</sup> and In-Ching Chen<sup>1</sup>

<sup>1</sup> Department of Electrical Engineering and Graduate Institute of Optoelectronic Engineering, National Chung Hsing University, Taichung 402, Taiwan

<sup>2</sup> Department of Chemical and Materials Engineering, National University of Kaohsiung, Kaohsiung 811, Taiwan

<sup>3</sup> Electronics and Optoelectronics Research Laboratories, Industrial Technology Research Institute, Hsinchu 310, Taiwan

Correspondence should be addressed to Cheng-Fu Yang; [cfyang@nuk.edu.tw](mailto:cfyang@nuk.edu.tw)

Received 22 October 2013; Accepted 13 January 2014; Published 9 March 2014

Academic Editor: Hong Seok Lee

Copyright © 2014 Fang-Hsing Wang et al. This is an open access article distributed under the Creative Commons Attribution License, which permits unrestricted use, distribution, and reproduction in any medium, provided the original work is properly cited.

In this study, AZO thin films were deposited on glass by using a 98 mol% ZnO + 1 mol%  $\text{Al}_2\text{O}_3$  (AZO, Zn : Al = 98 : 2) ceramic target and a r.f. magnetron sputtering system. At first, the effects of different  $\text{H}_2$  flow rates ( $\text{H}_2/(\text{H}_2 + \text{Ar}) = 0\% \sim 9.09\%$ , abbreviated as  $\text{H}_2$ -deposited AZO thin films, deposition temperature was  $200^\circ\text{C}$ ) added during the deposition process on the physical and electrical properties of AZO thin films were investigated. The optical transmittance at 400 nm~700 nm is more than 80% for all AZO thin films regardless of  $\text{H}_2$  flow rate and the transparency ratio decreased as the  $\text{H}_2$  flow rate increased. The Burstein-Moss shift effect was used to prove that the defects of AZO thin films decreased with increasing  $\text{H}_2$  flow rate. Also, the 2%  $\text{H}_2$ -deposited AZO thin films were also treated by the  $\text{H}_2$  plasma at room temperature for 60 min (plasma-treated AZO thin films). The value variations in the optical band gap ( $E_g$ ) values of the  $\text{H}_2$ -deposited and plasma-treated AZO thin films were evaluated from the plots of  $(\alpha h\nu)^2 = c(h\nu - E_g)$ , and the  $E_g$  values increased with increasing  $\text{H}_2$  flow rate. The  $E_g$  values also increased as the  $\text{H}_2$ -plasma process was used to treat on the  $\text{H}_2$ -deposited  $\text{Al}_2\text{O}_3$ -doped ZnO (AZO) thin films.

## 1. Introduction

Zinc oxide (ZnO), which is an n-type oxide semiconductor with a wurtzite crystal structure, is a novel II–VI compound semiconductor with various electrical, optical, acoustic, and chemical properties because of its wide direct band gap of 3.40 eV at room temperature. ZnO-based thin films are also good candidates to substitute for indium tin oxide (ITO) and tin oxide ( $\text{SnO}_2$ ) thin films in amorphous silicon ( $\alpha$ -Si) solar cells because they are stable in the hydrogen plasma, whereas ITO and  $\text{SnO}_2$  produce a metallic layer in the reducing plasma [1]. Additionally, in the case of  $\text{CuInSe}_2$ - and  $\text{CuInGaSe}_2$ -based heterojunction solar cells [2], ZnO coatings used as window layers have been found to enhance the current more than the standard CdS (or ZnS) coatings, due to ZnO's higher band gap. Nonstoichiometric, undoped ZnO thin films have usually shown low resistivity due to the oxygen vacancies and zinc interstitials [3]. Hydrogen almost

never occurs as an electrically neutral impurity inside a semiconductor or insulator. Invariably, it either (i) gives up its electron, becoming positively charged and acting as a donor in p-type semiconductors, or (ii) acquires an additional electron, becoming negatively charged and acting as an acceptor in n-type semiconductors. Therefore, hydrogen has the properties of an amphoteric impurity, when it is used as the atmosphere during the deposition process or used as the plasma after the films deposition, it will change the conductivity of formed thin films [4].

However, hydrogen is exclusively in a positively charged state when calculations show, and only the positively charged state occurs in ZnO. Thus, hydrogen can only act as a dopant, and other charge states cannot be stabilized in ZnO-based semiconductors [5]. In the past, several methods had been studied to improve the properties of ZnO-based thin films. Oh et al. reported the effects of different substrate temperatures on the crystallization behavior and optical properties of

ZnO and AZO thin films [6]. Strzemechny et al. reported on how the crystallization behavior and optical properties of AZO thin films were affected by the addition of hydrogen during the deposition process [7]. In this study, a 98 mol% ZnO + 1 mol% Al<sub>2</sub>O<sub>3</sub> (AZO, Zn:Al = 98:2) compound was used as the target, and radio frequency (RF) magnetron sputtering was developed as a viable fabrication technique to deposit AZO thin films. In the past, the deposition temperature of AZO thin films was changed from room temperature to 300°C. We had studied the effect of deposition temperature on the physical and electrical properties of AZO thin films [8]. In this study, hydrogen (H<sub>2</sub>) was used during the deposition process and as plasma gas of AZO thin films. We would further investigate the effects of H<sub>2</sub> on the physical and electrical properties of AZO thin films. At first, different H<sub>2</sub> flow rates (H<sub>2</sub>/(H<sub>2</sub> + Ar) = 0~9.09%) were added in Argon during the deposition process (abbreviated as the H<sub>2</sub>-deposited AZO thin films). Next, the deposited AZO thin films were treated by the H<sub>2</sub> plasma (abbreviated as plasma-treated AZO thin films). The effects of H<sub>2</sub> flow rates and H<sub>2</sub> plasma on the properties of AZO thin films were compared by observing the crystallization, resistivity and optical transmission spectrum. Optical transmission parameters were also used to investigate the effects of H<sub>2</sub> flow rate and H<sub>2</sub> plasma on the optical band gap of AZO thin films.

## 2. Experimental Details

AZO powder (ZnO:Al<sub>2</sub>O<sub>3</sub> = 98:2, mole ratio) was calcined at 1100°C and sintered at 1350°C to prepare the ceramic target. AZO thin films were deposited on 25 mm × 25 mm × 2 mm Corning 1737 glass substrates by using the r.f. magnetron sputtering system. The argon or argon-hydrogen were introduced into the chamber and the pressure was controlled at  $5 \times 10^{-2}$  Torr, under the 30 sccm with the different H<sub>2</sub>/(H<sub>2</sub> + Ar) flow rates (0%~9.09%, abbreviated as H<sub>2</sub>-deposited AZO thin films). The r.f. power was 100 W and the deposition temperature (200°C) was controlled by a thermocouple gauge. All AZO thin films had a thickness of about 120 nm by controlling the deposition time. After deposition, the plasma enhanced chemical vapor deposition (PECVD) hydrogen (H<sub>2</sub>) was treated on the as-deposited AZO thin films (plasma-treated AZO thin films) for 60 min. The working pressure was maintained at 1 Torr under the 300 sccm H<sub>2</sub> flow rate and the used power was 10 W. The chemical bonding states of oxygen, aluminum, and zinc in AZO thin films were investigated using an X-ray photoelectron spectroscopy (XPS) (ULVAC-PHI, PHI 5000 Versaprobe). The electrical resistivity was measured using a four-point probe, the optical transmittance spectrum was recorded using a Hitachi U-3300 UV/Vis spectrophotometer in the 300–800 nm wavelength range.

## 3. Results and Discussion

Surface images of the as-deposited and plasma-treated AZO thin films are shown in Figure 1. It is evident that H<sub>2</sub> flowing rate and plasma-treated process have large effects on the

films' surface morphologies. At first, the grain sizes increase with increasing H<sub>2</sub> flowing rate and reach the maximum at 2%, then the grain sizes decrease as the H<sub>2</sub> flowing rate is further increased. However, as Figures 1(a)–1(d) show, AZO thin films deposited at different H<sub>2</sub> flowing rate samples yielded rough and rugged surfaces. Also, as the H<sub>2</sub> flowing rate is increased, the roughness is apparently lessened because larger particle coalescence is observable causing major grain growth. When the H<sub>2</sub> plasma is used to treat on the deposited AZO thin films, the roughness is apparently improved, as Figures 1(e)–1(h) show. From the surface morphologies shown in Figure 1, the H<sub>2</sub> flowing rate and plasma-treated process will have the large effects on the physical and electrical properties of AZO thin films.

The XRD patterns of the Ar-deposited, 2% H<sub>2</sub>-deposited, and plasma-treated 2% H<sub>2</sub>-deposited AZO thin films were investigated, and the results are shown in Figure 2. The (002) peaks of the Ar-deposited, 2% H<sub>2</sub>-deposited, and plasma-treated 2% H<sub>2</sub>-deposited AZO thin films are situated at around  $2\theta = 34.61^\circ$ ,  $34.37^\circ$ , and  $34.27^\circ$ , respectively. These results imply that the parameter of lattice constant  $c$  decreases as H<sup>+</sup> ions are used in the fabrication process. The H<sup>+</sup> ions doping into AZO thin films and having smaller ion radius can cause these results. The full width at half maximum (FWHM) values for the (002) peak are 0.33, 0.24, and 0.28 for the Ar-deposited, 2% H<sub>2</sub>-deposited, and plasma-treated 2% H<sub>2</sub>-deposited AZO thin films, respectively. These results suggest that the H<sub>2</sub>-deposited and plasma-treated 2% H<sub>2</sub>-deposited AZO thin films have the better crystalline structure.

Figure 3 shows the transmittance spectra of the H<sub>2</sub>-deposited AZO thin films plotted against the different H<sub>2</sub> flow rate and wavelengths in the region of 300–800 nm. As Figure 3 shows, the optical transmittance at 400 nm~700 nm is more than 80% for all AZO thin films regardless of H<sub>2</sub> flow rate. The transparency ratio of the H<sub>2</sub>-deposited AZO thin films decreased as the H<sub>2</sub> flow rate increased. This result is due to the crystallization and the density of AZO thin films decrease. In the transmission spectra of the H<sub>2</sub>-deposited AZO thin films, the optical band edges are shifted to a shorter wavelength and a greater sharpness is noticeable in the curves of absorption edges as compared with those of Ar-deposited AZO thin films. Those results mean that as the H<sub>2</sub> flow rate increases, the absorption edge of AZO thin films is blue-shifted. In the past, determination of the optical band gap ( $E_g$ ) was often necessary to develop the electronic band structure of a thin-film material. However, using extrapolation methods, the  $E_g$  values of thin films can be determined from the absorption edge for direct interband transition, which can be calculated using the relation in (3) as follows:

$$(\alpha h\nu)^2 = c(h\nu - E_g), \quad (1)$$

where  $\alpha$  is the optical absorption coefficient,  $c$  is the constant for direct transition,  $h$  is Planck's constant, and  $\nu$  is the frequency of the incident photon [9]. The linear dependence of  $(\alpha h\nu)^2$  on  $h\nu$  indicates that AZO thin films are direct transition type semiconductors. In accordance with (3), the calculated optical band gap of the H<sub>2</sub>-deposited AZO thin



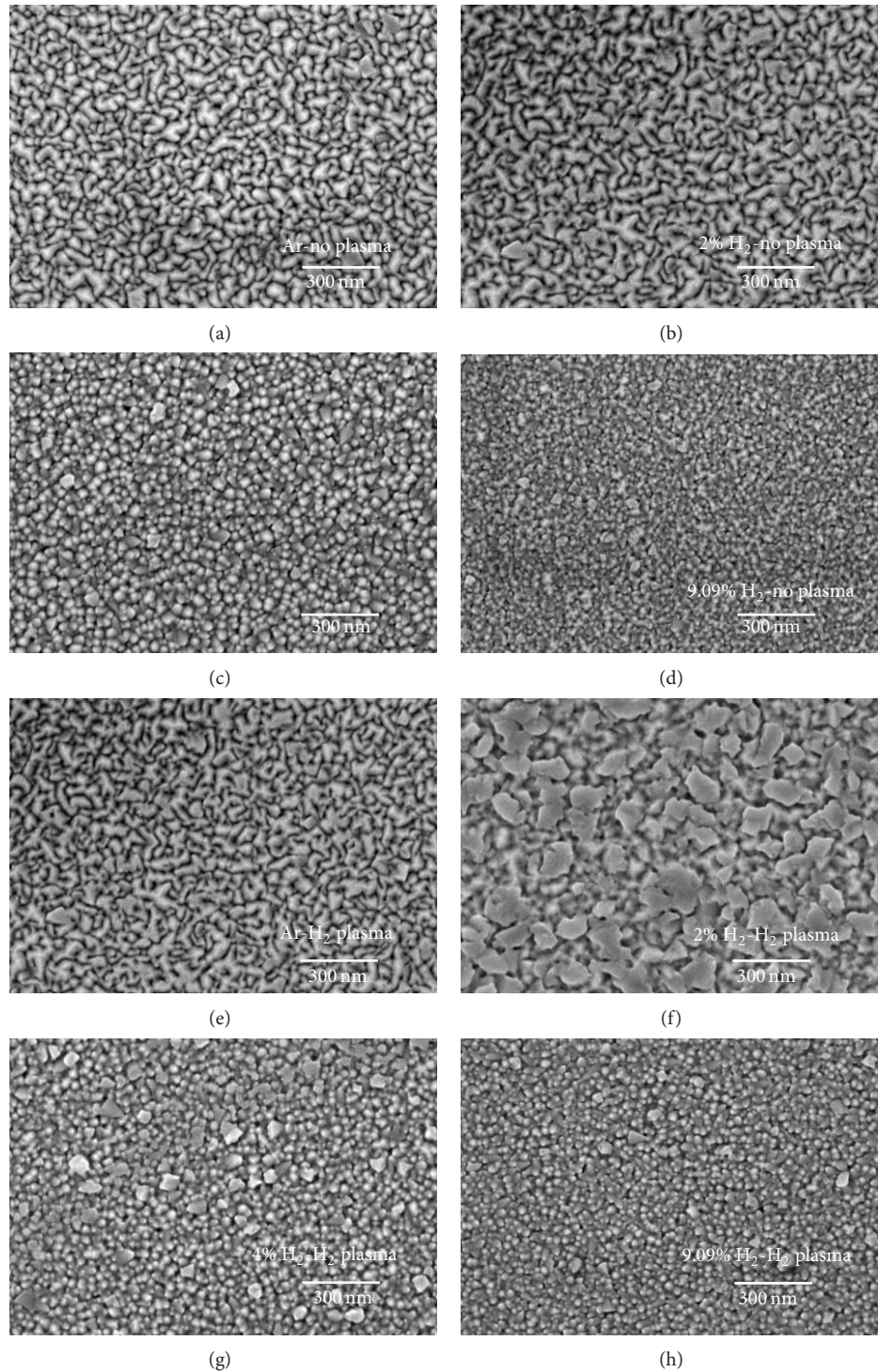


FIGURE 1: SEM observations of AZO thin films as a function of  $H_2/(H_2 + Ar)$  flowing rate, for the as-deposited samples (a) 0%, (b) 2%, (c) 4%, and (d) 9.09%, and for the as-deposited and plasma-treated samples (e) 0%, (f) 2%, (g) 4%, and (h) 9.09%.

films increased from 3.74 to 3.82 eV as  $H_2$  flowing rate increased.

Figure 4 shows the energy band gap of the plasma-treated AZO thin films plotted against wavelengths in the region of 300–800 nm. In the transmission spectra of the plasma-treated 2%  $H_2$ -deposited AZO thin films, the optical band

edge is also shifted to a shorter wavelength and a greater sharpness is also noticeable in the curves of the absorption edge as compared with those of the  $H_2$ -deposited AZO thin films shown in Figure 3. The plasma-treated 2%  $H_2$ -deposited AZO thin films are also the optimal  $H_2$  content, because they have the minimum resistivity (Figure 6). The calculated

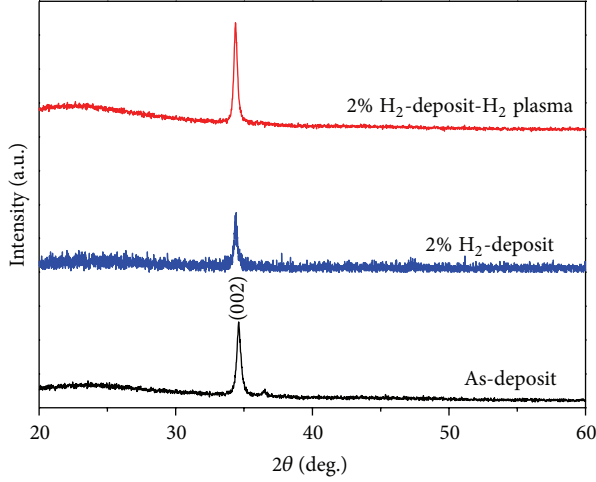


FIGURE 2: XRD patterns of the Ar-deposited, 2%  $H_2$ -deposited, and plasma-treated 2%  $H_2$ -deposited AZO thin films.

optical band gap of the plasma-treated 2%  $H_2$ -deposited AZO thin films also increased from 3.77 to 3.83 eV as the  $H_2$  flow rate increased. The optical transmittance at 400 nm~700 nm is more than 83% for all thin films regardless of  $H_2$  flow rate.

This blue-shift can be explained by the Burstein-Moss shift, a shift of Fermi level into the conduction band, which enhances the optical band gap by the energy, as follows [10, 11]:

$$\Delta E_g^{BM} = \frac{\hbar^2 k_F^2}{2} \left( \frac{1}{m_e} + \frac{1}{m_h} \right) = \frac{\hbar^2 k_F^2}{2m_{vc}^*}, \quad (2)$$

where the  $k_F$  stands for the Fermi wave vector,  $m_e$  is the effective mass of electrons in the conduction band, and  $m_h$  is the effective mass of holes in the valence band, which can be simplified as  $m_{vc}^*$ ; the Burstein-Moss shift  $\Delta E_g^{BM}$  can be rewritten by inducing  $k_F$  for the carrier concentration  $n_e$  as follows:

$$\Delta E_g^{BM} = \frac{h^2}{8m_{vc}^*} \left( \frac{3n_e}{\pi} \right)^{2/3}, \quad (3)$$

where  $h$  is the Planck's constant. Equation (3) shows the important relationship between the Burstein-Moss shift and the carrier concentration  $n_e$ . The shift of the absorption edge to the shorter wavelength region is due to the increase in carrier concentration. When the wavelength is equal to 300 nm, the visible light absorbed by the thin films is due to a quantum phenomenon called band edge absorption. Burstein indicated that an increase of the Fermi level in the conduction band of a degenerated semiconductor leads to the energy band widening effect [10, 11]. For that, the movement of the absorption edge to the shorter wavelength region is the Burstein-Moss shift.

From (3), we know that the shift of the optical band edge is caused by the increase in carrier concentration. This is because the Fermi level inside the conduction band moves upward with increasing donor concentration due to the filling of conduction band by the increase of carrier concentration

[12]. Those results suggest that the addition of  $H_2$  in the Ar as the deposition atmosphere can increase the carrier concentration. The absorption edge shifts monotonically to the shorter wavelength region as the hydrogen flow rate increases. This is because the Fermi level inside the conduction band moves upward with increasing donor concentration due to the filling of conduction band by the increase of carrier concentration [12].

The  $E_g$  value of ZnO thin films is about 3.40 eV and, in general, the measured  $E_g$  values of AZO thin films are consistent with and should be larger than that of ZnO thin films, because the  $E_g$  value of  $Al_2O_3$  is about 6.55 eV. As the 98 mol% ZnO + 1 mol%  $Al_2O_3$  composition is used as the target to deposit AZO thin films, the  $E_g$  value of AZO thin films can be calculated as

$$E_g = 0.98 \times 3.40 + 0.02 \times 6.55 = 3.46. \quad (4)$$

The blue-shift ( $\Delta E_g$ ) values are calculated from the difference between 3.46 eV and the  $E_g$  values obtained in Figures 3 and 4. Figure 5 shows the  $\Delta E_g$  values of the  $H_2$ -deposited and the plasma-treated 2%  $H_2$ -deposited AZO thin films as a function of carrier concentration. It is found that the  $\Delta E_g$  values are approximately proportional to  $n_e$ , and AZO thin films deposited at higher  $H_2$  content exhibit a stronger blue-shift phenomenon. These results show that when the  $H_2$  is used in the deposition processes, the  $E_g$  values become larger. This means that the blue-shift in the plasma-treated process has the same phenomenon, because  $H_2$  will cause the growth of AZO thin films. Those results also suggest that the  $H_2$  atoms also provide the electronic influences of AZO thin films, resulting in the increase of carrier concentration, however causing a blue-shift phenomenon.

To estimate the relation between  $\Delta E_g$  and  $n_e$  quantitatively, set  $m^* = 0.28 m_0$ , where  $m_0$  is the free electron mass, and substitute measured values of  $\Delta E_g$  and  $n_e$  into (3). The calculated corresponding exponent is about 0.64 for all the AZO thin films regardless of  $H_2$  addition and  $H_2$  plasma treatment. Oh et al. [13] also reported that the exponent is 0.655 from their Burstein-Moss shift measurement of AZO thin films, and other researches [14, 15] show that the exponents are in the range from 1/3 to 2/3. They explained that the electronic state of the thin films can be calibrated by electron-electron or electron-impurity scattering as the thin films have a high carrier concentration ( $\sim 10^{20} \text{ cm}^{-3}$ ), namely, the many-body effect such as Coulomb interaction or exchange interaction which makes the band gap values decrease [14]. Obviously, such a scattering phenomenon is slight in the AZO thin films developed in this study.

Figure 6 shows the resistivity of the  $H_2$ -deposited and plasma-treated 2%  $H_2$ -deposited AZO thin films. The higher conductivity of transparent conduction oxide (TCO) thin films results mainly from deviations in stoichiometric compositions due to dopants or substitution atoms. The resistivity of transparent conduction oxide (TCO) thin films is proportional to the reciprocal of the product of carrier concentration  $N$  and mobility  $\mu$  as follows:

$$\rho = \frac{1}{Ne\mu}. \quad (5)$$

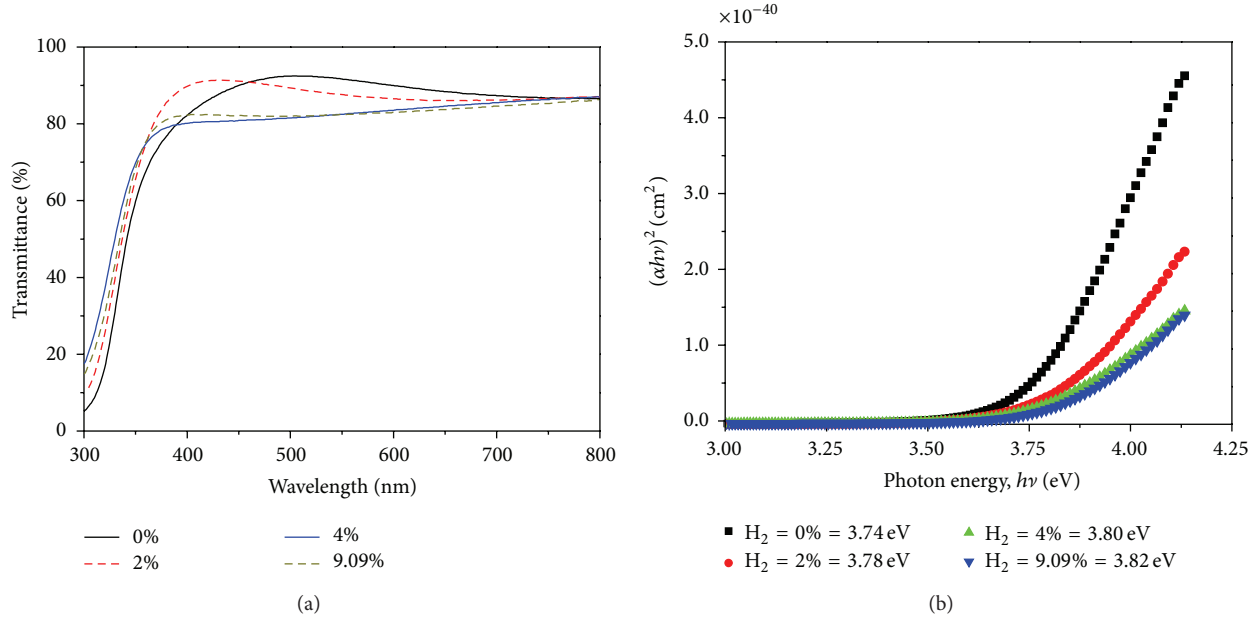


FIGURE 3: (a) Transmittance and (b)  $(\alpha h\nu)^2$  versus  $h\nu - E_g$  plots of the H<sub>2</sub>-deposited AZO thin films as a function of H<sub>2</sub> flowing rate.

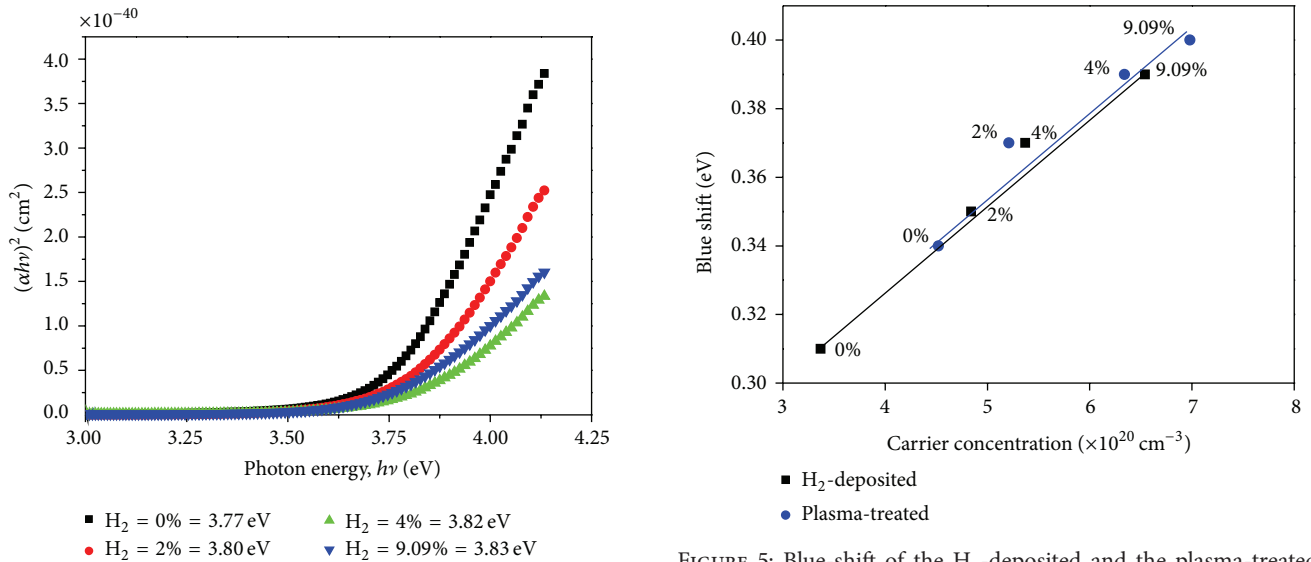


FIGURE 4:  $(\alpha h\nu)^2$  versus  $h\nu - E_g$  plots of the plasma-treated AZO thin films as a function of H<sub>2</sub> flowing rate.

Electrons generated from oxygen vacancies and Zn interstitial atoms resulting from the dopant primarily determine the conduction properties of TCO thin films. Therefore, the electrical conductivity of AZO thin films will have large variations due to introducing H<sub>2</sub> in Ar during the sputtering deposition process.

The resistivity of AZO thin films deposited in pure Ar ambient was  $25.2 \times 10^{-4} \Omega\text{-cm}$ . However, the resistivity of the 2% H<sub>2</sub>-deposited AZO thin films was  $13.72 \times 10^{-4} \Omega\text{-cm}$  deposition atmosphere, and the minimum resistivity of

$12.67 \times 10^{-4} \Omega\text{-cm}$  existed in the plasma-treated 2% H<sub>2</sub>-deposited AZO thin films. As the H<sub>2</sub> rate was increased to 4%, the resistivity of the H<sub>2</sub>-deposited AZO under H<sub>2</sub> + Ar atmosphere was beyond that of Ar-deposit ones. When AZO thin films are deposited on a glass substrate, many defects result and inhibit electron movement. In addition, too many oxygen vacancies may lead to an increase in scattering centers and a resultant decrease in mobility. The resistivity of AZO thin films decreases with the effects of hydrogen flow rate and hydrogen plasma, probably because the number of defects declines as the crystallization improves with H<sup>+</sup> ions for the crystal structure which boosts the deposition atoms' mobility.



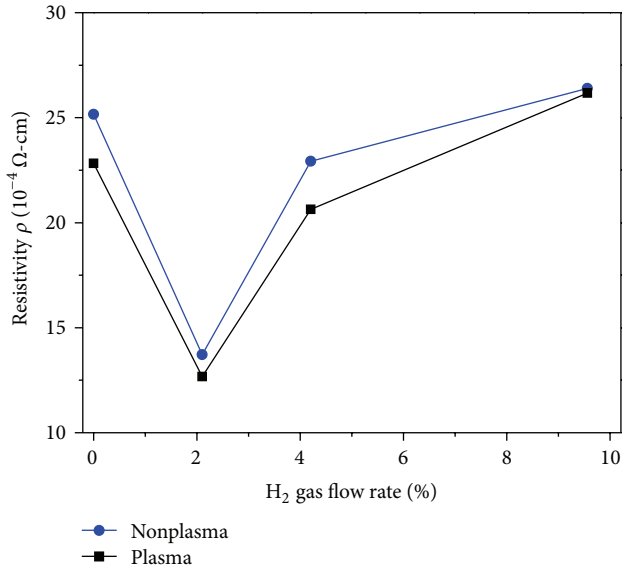


FIGURE 6: Resistivity ( $\rho$ ) of the as-deposited and the plasma-treated AZO thin films as a function of  $H_2$  flowing rate.

There are two kinds of donors contributing in AZO thin films' conductive mechanism. One is the native donor including interstitial Zn or oxygen vacancy and the other is substitutional Al atom. As 2%  $H_2$  flow rate is used, a strong influence on oxygen extracts it from AZO thin films, which results in more vacancies to enhance the carrier concentration, and the conductivity has been improved. There are some scattering mechanisms occurring in AZO thin films which mainly include the neutral and ionized impurities and the grain boundaries scattering. When  $H_2$  flow rate is more than 2%,  $H_2$  creates more oxygen vacancies and generates more defects and free carriers, both of the neutral and ionized impurities scattering centers should increase. Besides, a small quantity of hydrogen atoms situates in the Zn–O bond center to relax the surrounding atoms. For that, as the  $H_2$  flow rate is more than 2%, the resistivity increases with increasing  $H_2$  flow rate. In this study, 2% is the optimal  $H_2$  content, because AZO thin films have the minimum resistivity.

To clarify the mechanism of improvement in resistivity, the chemical structures of the Ar-deposited,  $H_2$ -deposited, and plasma-treated AZO thin films were investigated by XPS. Figure 7 shows the XPS spectra for their Gaussian-resolved components of O 1s. As shown in Figure 7, a shoulder was visible on the high-energy side of the Ar-doped AZO thin films, indicating that at least two different bonds exist. The bonding state of O 1s spectrum of the Ar-doped AZO thin films is resolved into two components centered at 530.55 eV and 532.55 eV, respectively. The low bonding energy component centered at 530.55 eV is attributed to  $O^{2-}$  ions on the wurtzite structure of the hexagonal  $Zn^{2+}$  ion array, surrounded by Zn atoms with their full complement of nearest neighbor  $O^{2-}$  ions [15]. The high bonding energy component centered at 532.55 eV is attributed to the existence of adsorbed  $O_2$  on the surfaces of the AZO thin films [16, 17]. For the 2%  $H_2$ -deposited AZO thin films, the O 1s peak slightly shifted

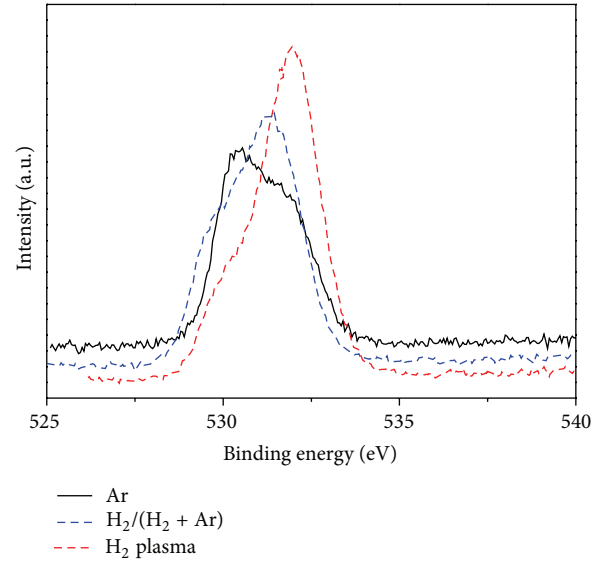


FIGURE 7: XPS spectra and their Gaussian-resolved components of O 1s of the as-deposited and the plasma-treated AZO thin films as a function of  $H_2$  flowing rate.

to the high energy side and was located at 531.95 eV. After plasma treatment, the O 1s peak of the 2%  $H_2$ -deposited AZO thin films shifted to the low energy side and was located at 531.25 eV. Unfortunately, these contributions from the surface cannot be separated from the main signal and might differ between samples. Binding energies from 531 eV to 532 eV are found for hydroxides and bonding energies from 530 eV to 530.8 eV are found for oxides. However, a Gauss-Lorentz fits of the 2%  $H_2$ -deposited and plasma-treated AZO thin films yield the main peaks at 531.25 eV and 531.95 eV for  $Zn(OH)_2$ . Our attributions are feasible and lie in the range of values found in other literature. From the XPS measurements, it can be concluded that the  $Zn(OH)_2$  is found in the 2%  $H_2$ -deposited and plasma-treated AZO thin films, because the  $H_2$  is existed from the surface into the crystal [18].

#### 4. Conclusions

The effects of different hydrogen ( $H_2/(H_2 + Ar)$ , 0%~9.09%) flow rates (deposition temperature was 200°C) added during the deposition process of AZO thin films were investigated. The Burstein-Moss shift effects were measured and used to prove that the defects in AZO thin films decreased with increasing  $H_2$  flow rate. The value variations in the optical band gap ( $E_g$ ) of the  $H_2$ -deposited and plasma-treated AZO thin films were evaluated from the plots of  $(\alpha h\nu)^2 = c(h\nu - E_g)$ , and the  $E_g$  values increased with increasing hydrogen flow rate. As the hydrogen flow rate increased from 0 to 9.09%, the calculated  $E_g$  values increased from 3.74 eV to 3.82 eV, and the  $E_g$  values of the plasma-treated AZO thin films increased from 3.77 eV to 3.83 eV. From the XPS measurements, it could be concluded that  $Zn(OH)_2$  was formed in the  $H_2$ -deposited and plasma-treated AZO thin films. The resistivity of AZO thin films decreased with

increasing hydrogen flow rate and reached a minimum value of  $13.56 \times 10^{-4} \Omega\text{cm}$  at a  $\text{H}_2$  flow rate of 2%, the minimum resistivity of  $12.67 \times 10^{-4} \Omega\text{-cm}$  existed in the plasma-treated 2%  $\text{H}_2$ -deposited AZO thin films.

## Conflict of Interests

The authors declare that there is no conflict of interests regarding the publication of this paper.

## Acknowledgments

The authors acknowledge the financial support of NSC 101-2221-E-005-065, NSC 102-2622-E-390-002-CC3, and NSC 102-2221-E-390-027.

## References

- [1] S. Major, S. Kumar, M. Bhatnagar, and K. L. Chopra, "Effect of hydrogen plasma treatment on transparent conducting oxides," *Applied Physics Letters*, vol. 49, no. 7, pp. 394–396, 1986.
- [2] L. Stolt, J. Hedström, J. Kessler, M. Ruckh, K. Velthaus, and H. Schock, "ZnO/CdS/CuInSe<sub>2</sub> thin-film solar cells with improved performance," *Applied Physics Letters*, vol. 62, no. 6, pp. 597–599, 1993.
- [3] D. H. Zhang and D. E. Brodie, "Effects of annealing ZnO films prepared by ion-beam-assisted reactive deposition," *Thin Solid Films*, vol. 238, no. 1, pp. 95–100, 1994.
- [4] J. Chevallier, B. Theys, A. Lusson, C. Grattapain, A. Deneuville, and E. Gheeraert, "Hydrogen-boron interactions in p-type diamond," *Physical Review B—Condensed Matter and Materials Physics*, vol. 58, no. 12, pp. 7966–7969, 1998.
- [5] C. G. van de Walle, "Hydrogen in semiconductors and insulators," *Journal of Alloys and Compounds*, vol. 446–447, pp. 48–51, 2007.
- [6] B. Y. Oh, M. C. Jeong, and J. M. Myoung, "Stabilization in electrical characteristics of hydrogen-annealed ZnO:Al films," *Applied Surface Science*, vol. 253, no. 17, pp. 7157–7161, 2007.
- [7] Y. M. Strzhemechny, H. L. Mosbacker, D. C. Look et al., "Remote hydrogen plasma doping of single crystal ZnO," *Applied Physics Letters*, vol. 84, no. 14, pp. 2545–2547, 2004.
- [8] F. H. Wang, H. P. Chang, C. C. Tseng, and C. C. Huang, "Effects of  $\text{H}_2$  plasma treatment on properties of ZnO:Al thin films prepared by RF magnetron sputtering," *Surface and Coatings Technology*, vol. 205, no. 23–24, pp. 5269–5277, 2011.
- [9] T. S. Moss, "The interpretation of the properties of indium antimonide," *Proceedings of the Physical Society B*, vol. 67, no. 10, pp. 775–782, 1954.
- [10] E. Burstein, "Anomalous optical absorption limit in InSb," *Physical Review*, vol. 93, no. 3, pp. 632–633, 1954.
- [11] I. Hamberg, C. G. Granqvist, K. F. Berggren, B. E. Sernelius, and L. Engström, "Band-gap widening in heavily Sn-doped  $\text{In}_2\text{O}_3$ ," *Physical Review B—Condensed Matter and Materials Physics*, vol. 30, no. 6, pp. 3240–3249, 1984.
- [12] N. Serpone, D. Lawless, and R. Khairutdinov, "Size effects on the photophysical properties of colloidal anatase  $\text{TiO}_2$  particles: size quantization or direct transitions in this indirect semiconductor?" *The Journal of Physical Chemistry*, vol. 99, no. 45, pp. 16646–16654, 1995.
- [13] B. Y. Oh, M. C. Jeong, W. Lee, and J. M. Myoung, "Properties of transparent conductive ZnO:Al films prepared by co-sputtering," *Journal of Crystal Growth*, vol. 274, no. 3–4, pp. 453–457, 2005.
- [14] K. H. Kim, K. C. Park, and D. Y. Ma, "Structural, electrical and optical properties of aluminum doped zinc oxide films prepared by radio frequency magnetron sputtering," *Journal of Applied Physics*, vol. 81, no. 12, pp. 7764–7772, 1997.
- [15] B. H. Choi, H. B. Im, J. S. Song, and K. H. Yoon, "Optical and electrical properties of  $\text{Ga}_2\text{O}_3$ -doped ZnO films prepared by r.f. sputtering," *Thin Solid Films*, vol. 193–194, part 2, pp. 712–720, 1990.
- [16] M. Chen, X. Wang, Y. H. Yu et al., "X-ray photoelectron spectroscopy and auger electron spectroscopy studies of Al-doped ZnO films," *Applied Surface Science*, vol. 158, no. 1, pp. 134–140, 2000.
- [17] H. Sato, T. Minami, S. Takata, T. Mouri, and N. Ogawa, "Highly conductive and transparent ZnO:Al thin films prepared on high-temperature substrates by d.c. magnetron sputtering," *Thin Solid Films*, vol. 220, no. 1–2, pp. 327–332, 1992.
- [18] W. Eisele, A. Ennaoui, P. Schubert-Bischoff et al., "XPS, TEM and NRA investigations of  $\text{Zn}(\text{Se},\text{OH})/\text{Zn}(\text{OH})_2$  films on  $\text{Cu}(\text{In},\text{Ga})(\text{S},\text{Se})_2$  substrates for highly efficient solar cells," *Solar Energy Materials and Solar Cells*, vol. 75, no. 1–2, pp. 17–26, 2003.

## Research Article

# Tunable Band Gap Energy of Mn-Doped ZnO Nanoparticles Using the Coprecipitation Technique

**Tong Ling Tan, Chin Wei Lai, and Sharifah Bee Abd Hamid**

*Nanotechnology & Catalysis Research Centre (NANOCAT), Deputy Vice Chancellor (Research & Innovation),  
Institute of Graduate Studies, University of Malaya, 50603 Kuala Lumpur, Malaysia*

Correspondence should be addressed to Sharifah Bee Abd Hamid; [sharifahbee@um.edu.my](mailto:sharifahbee@um.edu.my)

Received 14 October 2013; Accepted 17 December 2013; Published 28 January 2014

Academic Editor: Clare C. Byeon

Copyright © 2014 Tong Ling Tan et al. This is an open access article distributed under the Creative Commons Attribution License, which permits unrestricted use, distribution, and reproduction in any medium, provided the original work is properly cited.

A simple coprecipitation technique was introduced to form manganese (Mn) doped on zinc oxide (ZnO) nanoparticles effectively. Based on our morphological studies, it was revealed that mean particle size was increased while bigger agglomeration of nanoparticles could be observed as the amount of concentration of Mn was increased. Interestingly, it was found that the position of the absorption spectra was shifted towards the lower wavelength (UV region) as correlated with the increasing of Mn dopants concentration into ZnO nanoparticles. This result inferred that optimum content of Mn doped into the ZnO nanoparticles was crucial in controlling the visible/UV-responsive of samples. In the present study, 3 mol% of Mn dopants into the ZnO nanoparticles exhibited the better UV as well as visible light-responsive as compared to the other samples. The main reason might be attributed to the modification of electronic structure of ZnO nanoparticles via lattice doping of Mn ions into the lattice, whereas excessive Mn dopants doped on ZnO nanoparticles caused the strong UV-responsive due to the more 3d orbitals in the valence band.

## 1. Introduction

Nowadays, most countries are facing environmental pollution problems and thus the awareness of people upon this matter was increased tremendously. Water is an essential source for human beings and it was shown that the demand of clean and safe drinking water is rising; therefore, the use of the nano semiconductor material on photocatalytic oxidation for oxidizing the toxic pollutant has become of great interest in recent material research field [1].

Zinc oxide (ZnO) is an essential semiconductor with direct band gap of 3.3 eV and high excitant binding energy of 60 meV. Due to its potential application in many areas such as optoelectronic devices, solar cells, chemical sensor, and photocatalyst hence, it has attracted the attention of more and more researchers and scientists to develop ZnO in the field of science and technology. In addition, ZnO is lower in cost and is environmental friendly as compared to other metal oxides [2]. Normally, ZnO is studied in nanoscale; this is probably due to the fact that the high surface area to mass ratio of nanoparticles could enhance the adsorption of organic pollutants on the surface of particles as compared to the bulk materials [1].

However, undoped ZnO nanoparticles have certain limitation on light absorption catalytic activity. It was revealed that ZnO has a large band gap energy of about 3.3 eV which can only absorb light within UV region. In addition, the fast recombination rate of photogenerated electron-hole pairs will also contribute to the limitation of photocatalytic activity. Thus, in order to enhance the optical, magnetic, and electrical properties of ZnO, the transition metal-doped ZnO nanoparticles have been introduced. The modification of ZnO nanoparticles with impurity incorporation leads to possible application in UV optoelectronic and spin electronics [3]. Among the transition elements, Mn shows the maximum magnetic behaviors with electron effective mass  $\sim 0.3m_e$  ( $m_e$  = free electron mass); a doping of Mn into the ZnO semiconductor host lattice may result in large injected spins and carrier which make it suitable to be applied as diluted magnetic semiconductor (DMSs) [4].

Actually, the term “doped” is used to modify the optical or magnetic properties of the host by adding impurities ions against the host lattice. The doping with 3d metals such as Mn, Ni, Fe, Co, and Cr will increase the surface area and reduce the particle size of ZnO nanoparticles [5]. Mn is preferred for

TABLE 1: Amounts of reactant required to prepare nanoparticles with different manganese concentrations.

	Amounts added in mmol for mol% of $\text{Zn}(\text{OAc})_2 \cdot 2\text{H}_2\text{O}$ , $\text{Mn}(\text{OAc})_2 \cdot 4\text{H}_2\text{O}$ and NaOH					
Chemicals	0	3	5	10	15	20
$\text{Zn}(\text{OAc})_2 \cdot 2\text{H}_2\text{O}$	2.00	1.94	1.90	1.80	1.70	1.60
$\text{Mn}(\text{OAc})_2 \cdot 4\text{H}_2\text{O}$	0.00	0.06	0.10	0.20	0.30	0.40
NaOH	2.00	2.00	2.00	2.00	2.00	2.00

the doping of ZnO due to the fact that the d electron of Mn at  $t_{2g}$  level can easily overlap with the ZnO's valence bond as compared with other transition elements. There are various studies which showed, that Mn-doped semiconductors have influenced the physical, chemical, and structural properties of undoped ZnO nanoparticles. For example, the optical properties of undoped ZnO nanoparticles especially on the tuning of the band gap can be greatly improved at the nanoscale by optimum content of Mn doping [6, 7].

Currently, the synthesis of Mn-doped ZnO nanoparticles can be through various types of methods such as wet-chemical, sol-gel, coprecipitate, solid-thermal, and spray pyrolysis. In order to enhance the optical properties and obtain a small particle size, a search for alternative synthesis methods for efficiency Mn doping with ZnO nanoparticles has become the major interest of studies. The purpose of this work was to synthesize band gap energy tunable of Mn-doped ZnO nanoparticles with high surface area for better photocatalytic performance using coprecipitation method. Zinc acetate ( $\text{Zn}(\text{ac})_2 \cdot 2\text{H}_2\text{O}$ ) and manganese acetate ( $\text{Mn}(\text{ac})_2 \cdot 4\text{H}_2\text{O}$ ) act as precursors and absolute ethanol was used as a solvent to synthesis Mn-doped ZnO nanoparticles. Basically, the synthesis of electrostatically stable Mn-doped ZnO nanoparticles was performed in an alcoholic solution in order to avoid the formation of ZnOH [8].

## 2. Experimental

**2.1. Materials.** All the chemicals used were analytical grade and were used in this experiment without further purification. The chemicals used were zinc acetate dehydrate ( $\text{Zn}(\text{OAc})_2 \cdot 2\text{H}_2\text{O}$ ), >99.5%, from Fluka), manganese acetate tetrahydrate, ( $\text{Mn}(\text{OAc})_2 \cdot 4\text{H}_2\text{O}$ , >98%), sodium hydroxide (NaOH, 98%), and absolute ethanol ( $\text{C}_2\text{H}_5\text{OH}$ , >99%).

**2.2. Synthesis Procedures of Mn-Doped ZnO Nanoparticles.** Mn-doped ZnO nanoparticle was prepared by using sol-gel method [8]. Mn-doped ZnO nanoparticles were synthesized by the reaction of  $\text{Zn}^{2+}$ ,  $\text{Mn}^{2+}$ , and  $\text{OH}^-$  in an alcoholic medium (ethanol). For 5 mol% of Mn-doped ZnO nanoparticles, there were generally three solutions that needed to be prepared. The first solution contained 20 mM of zinc acetate dehydrate ( $\text{Zn}(\text{ac})_2 \cdot 2\text{H}_2\text{O}$ ) in 10 mL of ethanol. The second solution consisted of 1.0 mM of manganese acetate tetrahydrate ( $\text{Mn}(\text{ac})_2 \cdot 4\text{H}_2\text{O}$ ) in 10 mL of ethanol. Then, the next solution consisted of 20 mM of NaOH in 10 mL of ethanol. These three solutions at first were heated to 50°C. After heating, zinc acetate solution was poured into round bottom flask and then manganese acetate solution was added to it.

Zinc acetate and manganese acetate solution was again heated to 80°C with constant stirring for 30 minutes. Then, NaOH solution was added dropwise into the solution containing  $\text{Zn}(\text{ac})_2 \cdot 2\text{H}_2\text{O}$  and  $\text{Mn}(\text{ac})_2 \cdot 4\text{H}_2\text{O}$  along with reflux. The solutions were again heated to 60–65°C with magnetic stirring for 2 h. After this, the solution was cooled to room temperature. The precipitate was formed and was washed several times with distilled water and then followed by ethanol. The purpose of washing precipitate with ethanol was to remove the unwanted salt and impurities.

To investigate the effect of different concentrations of Mn dopant ions on the physical, chemical, and optical properties of Mn-doped ZnO nanoparticles, the same procedures as stated above were carried out for 3 mol%, 10 mol%, 15 mol%, and 20 mol% of Mn-doped ZnO nanoparticles. Table 1 below shows the amount of reactant required to prepare nanoparticles with different manganese concentrations.

**2.3. Characterization.** The effects of Mn/ZnO on the composition, morphology, and optical properties of Mn-doped ZnO nanoparticles were determined by various techniques. Elemental and chemical composition of Mn-doped ZnO nanoparticles were carried out using a Scanning Electron Microscope-Energy Dispersive X-ray (SEM-EDX). Surface morphologies of Mn-doped ZnO nanoparticles were carried out using a Scanning Electron Microscope (SEM). The SEM images are shown in the magnification of 10,000. FTIR analysis was performed using a FTIR spectroscopy Perkin Elmer spectrum GX model to obtain information about the chemical bonding and molecular structure in a sample. The optical absorption spectra of Mn-doped ZnO nanoparticles were carried out using a UV-visible Spectrophotometer operating at a wavelength range of 300 nm to 500 nm. Fluorescence spectrophotometer, CARY Eclipse, and Varian model were used to investigate the effect of different Mn-doped contents on the optical emission properties of Mn-doped ZnO nanoparticles.

## 3. Results and Discussion

**3.1. Morphological Studies.** The influence of different percentage of Mn (3, 5, 10, 15, and 20 mol%) on the surface morphologies of Mn-doped ZnO nanoparticles was studied by SEM which is shown in Figure 1. It can be seen that as the percentage of Mn doped increases, the grain size of the ZnO nanoparticles is also increasing (Table 2). From the SEM images, it can be seen that with above 15 mol%, the agglomeration increases. This may probably be related to the kinetic equilibrium process where the high concentration of Mn



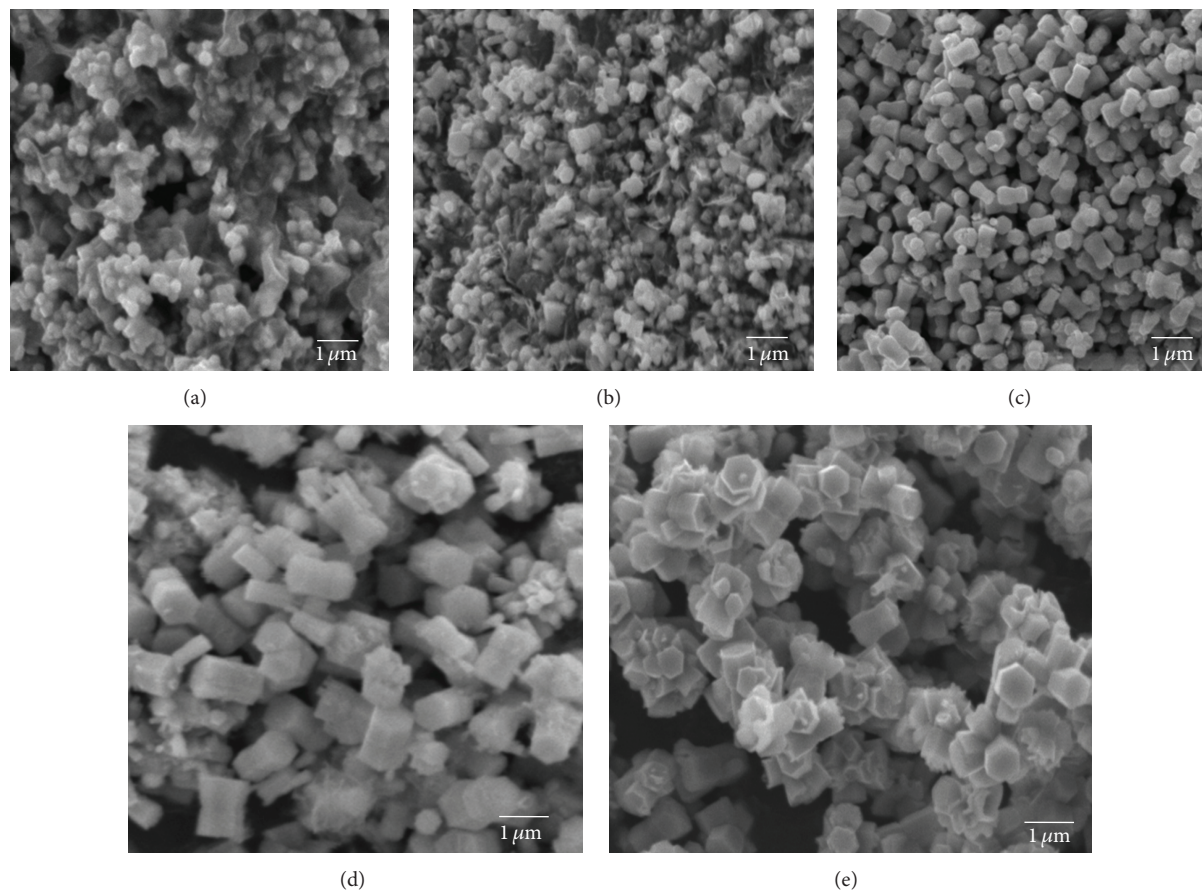


FIGURE 1: SEM images of Mn-doped ZnO nanoparticles with (a) 3 mol%, (b) 5 mol%, (c) 10 mol%, (d) 15 mol%, and (e) 20 mol%.

TABLE 2: The mean size obtained from different percentage of Mn doping in ZnO nanoparticles.

Manganese dopant concentration (mol%)	Mean particle size (nm)
3	157
5	187
10	245
15	432
20	509

dopants could be nucleated with oxygen ions by itself and form bigger particles. Hence, it could be difficult for the Mn to be incorporated into ZnO lattice in higher concentration. As a conclusion, a lower dopant concentration of Mn-doped ZnO nanoparticles showed lower agglomeration and well-ordered and small particles size distribution than the higher Mn dopant concentration [9].

**3.2. Elemental and Chemical Composition Analysis.** Figure 2 shows the EDX spectrum of 3 mol%, 5 mol%, 10 mol%, 15 mol%, and 20 mol% of Mn-doped ZnO nanoparticles. From the EDX spectrum, it can be seen that the amount of Mn element in the samples increased depending on the increasing Mn incorporation in the ZnO nanoparticles. The area of

the corresponding spectral K lines gives the quantitative results of the Mn/Zn ratio [10]. The elemental analysis for O, Mn, and Zn for each sample (3 mol%, 5 mol%, 10 mol%, 15 mol%, and 20 mol%) was shown in Table 3.

**3.3. FTIR Analysis.** Various peaks corresponding to the main absorption bands can be seen from the FTIR spectrum on Figure 3. The broad absorption peak around  $3376\text{ cm}^{-1}$ ,  $3377\text{ cm}^{-1}$ , and  $3378\text{ cm}^{-1}$  represents the O–H stretching of the hydroxyl group. The peak around  $2900\text{ cm}^{-1}$  was due to C–H (acetate) stretching [11]. Two absorption peaks are observed between  $1650$  and  $1400\text{ cm}^{-1}$ , corresponding to the asymmetric and symmetric stretching of the carboxyl group (C=O).

From the studies, the stretching mode of undoped ZnO is at  $431\text{ cm}^{-1}$ . In this work, for  $\text{Zn}_{1-x}\text{Mn}_x\text{O}$  ( $x = 0.03, 0.05, 0.10, 0.15$ , and  $0.20$ ), the values of absorption were found to be blueshifted at  $443, 450, 462, 470$ , and  $481\text{ cm}^{-1}$ , respectively. Undoubtedly, this can prove that the Zn–O–Zn network was perturbed by the presence of Mn in its environment with the change in the peak position of the ZnO absorption bands [12].

**3.4. Optical Studies.** In this work, we obtained the wavelength for undoped ZnO and 3 mol%, 5 mol%, 10 mol%, and 15 mol% Mn-doped ZnO nanoparticles. It was observed that

TABLE 3: Mass % of O, Mn, and Zn as determined by EDX analysis.

Element	Mass %				
	3 mol%	5 mol%	10 mol%	15 mol%	20 mol%
O	23.48	33.73	7.60	43.31	53.34
Mn	3.26	4.66	9.51	15.23	20.97
Zn	73.25	61.62	82.89	41.46	25.69

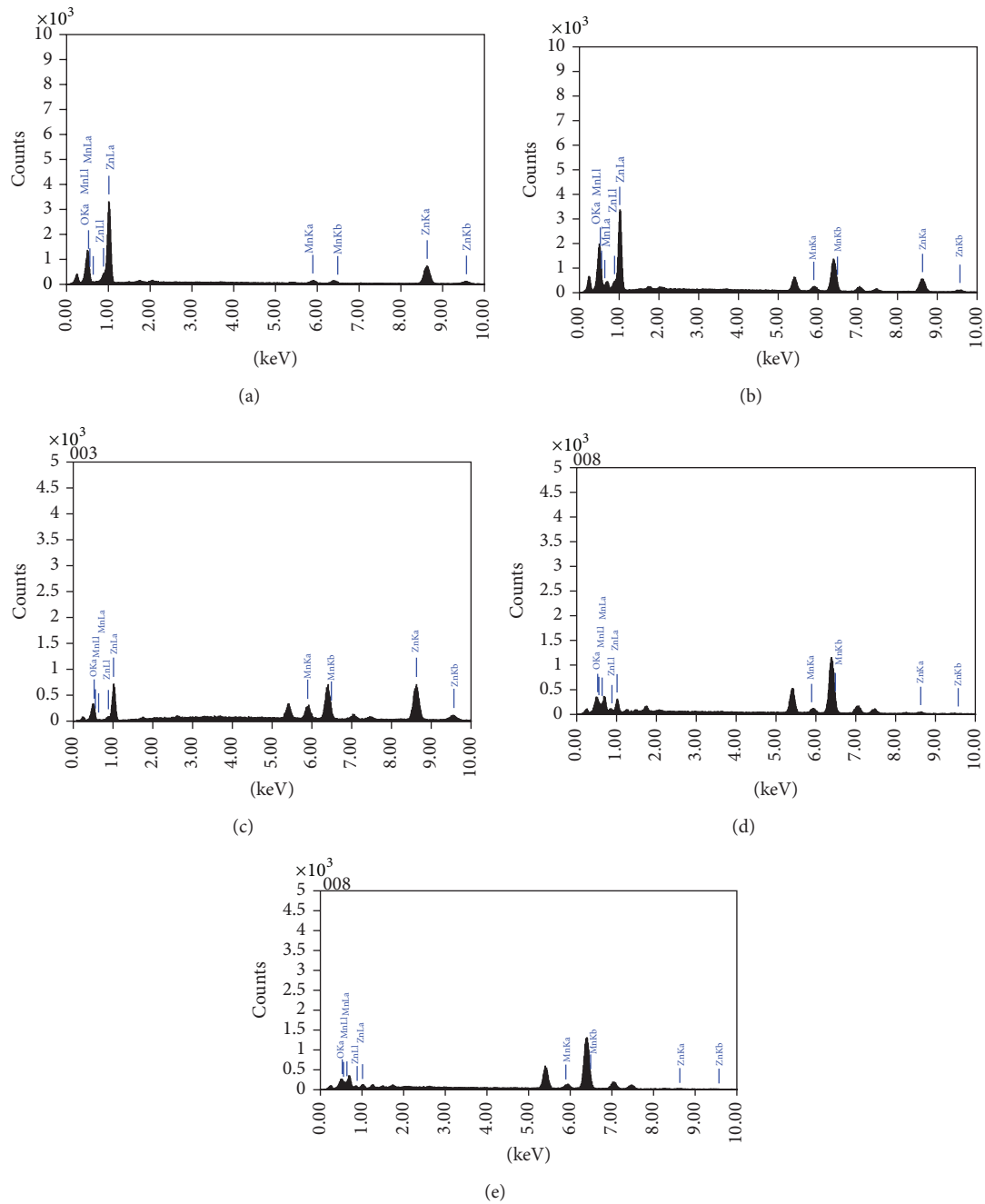


FIGURE 2: EDX spectrum of Mn-doped ZnO nanoparticles with (a) 3 mol%, (b) 5 mol%, (c) 10 mol%, (d) 15 mol%, and (e) 20 mol%.

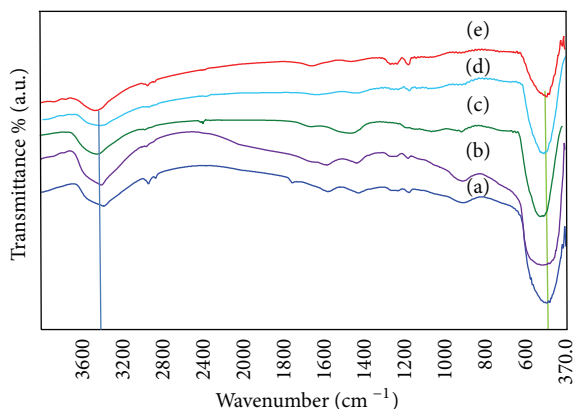


FIGURE 3: FTIR spectrum of Mn-doped ZnO nanoparticles with (a) 3 mol%, (b) 5 mol%, (c) 10 mol%, (d) 15 mol%, and (e) 20 mol% of Mn dopant concentrations.

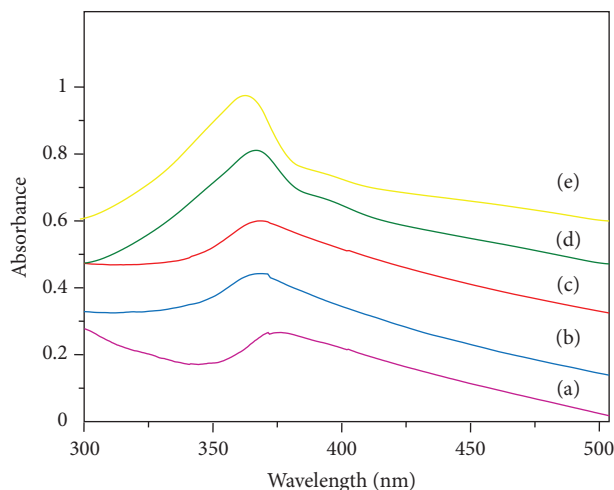


FIGURE 4: Absorbance spectrum of Mn-doped ZnO nanoparticles with (a) pure ZnO, (b) 3 mol%, (c) 5 mol%, (d) 10 mol%, and (e) 15 mol%.

the absorption edges of undoped ZnO and 3 mol%, 5 mol%, 10 mol% and 15 mol% of Mn doping are 374.5, 370, 367, 365, and 362.5 nm as shown in Figure 4.

With the increasing of Mn concentration in ZnO nanoparticles, the position of the absorption spectra is shifted towards the lower wavelength side or known as blue-shifted which is correlated to the change in the optical band gap value. The band gap energy of undoped and Mn-doped ZnO nanoparticles could be determined using the following formula:  $E_{bg} = hc/\lambda$ , where  $E_{bg}$  is the band gap energy,  $h$  is Planck's constant ( $4.135667 \times 10^{-15}$  eV s),  $c$  is the velocity of light ( $2.997924 \times 10^8$  m/s), and  $\lambda$  is the absorption wavelength (nm) [11]. The value of the band gap obtained for undoped ZnO is 3.31 eV and it starts increasing for 3, 5, 10, and 15 mol% samples as 3.35, 3.38, 3.40, and 3.42 eV, respectively.

Generally, blueshifted in the band gap was due to Mn doping in ZnO nanoparticles with the replacement of  $Zn^{2+}$  ions in the ZnO lattice by  $Mn^{2+}$  ions. This indicates that the band gap of ZnO nanoparticles increases with the increasing doping concentration of  $Mn^{2+}$  ion. Furthermore, the blueshifted

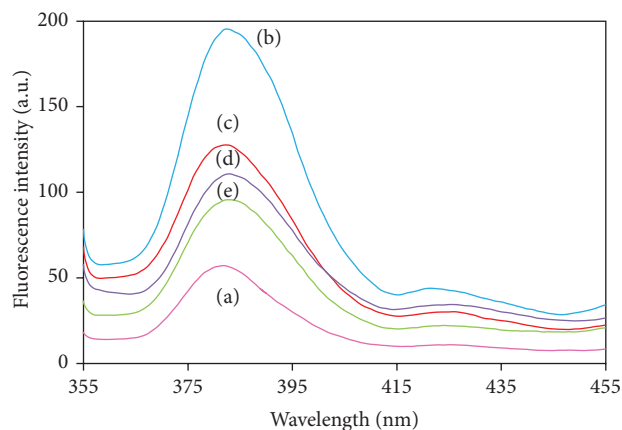


FIGURE 5: Fluorescence spectra of Mn-doped ZnO nanoparticles with (a) pure ZnO, (b) 3 mol%, (c) 5 mol%, (d) 10 mol%, and (e) 15 mol%.

in the band gap energy with increasing the amount of Mn doping concentration can be defined as the separation in energy between the top of the valence band and the unoccupied energy states in the conduction band [13].

The fluorescence spectrum of undoped ZnO nanoparticles was taken into account for the comparison of fluorescence intensity between the undoped and Mn-doped ZnO nanoparticles. From the studies, it was known that ZnO tends to produce intrinsic defects such as interstitial zinc and oxygen vacancy and these defects will certainly affect the fluorescence behaviour of ZnO. The fluorescence emission peak shifts are found to be size dependent due to quantum size effect. The shift from the top of the valence band and the bottom of conduction band is contributed as a function of fluorescence emission peaks shift. Normally, it was indicated that a redshift of UV emission as the particle size increases [14]. The intrinsic luminescence properties of ZnO rely upon the concentration of Mn doping and thus the fluorescence intensity decreases with the increasing of Mn dopant concentration and the spectrum related to a Mn dopant concentration of 3 mol% shows the maximum of fluorescence intensity which is shown in Figure 5. The increase of fluorescence intensity indicates that the incorporation of  $Mn^{2+}$  ion into ZnO nanoparticles may suppress some non-radiative recombination of free excitation that is near band-edge emission. Moreover, on doping with Mn, the surface traps are eventually quenched which is correlated to the reduction in the surface traps. Moreover, higher concentration of Mn may induce a high density of defects and thus reduces the intensity of emitted light [15].

#### 4. Conclusion

Mn-doped ZnO nanoparticles have been successfully synthesized through coprecipitation method. The effects of manganese dopant concentrations (3 mol%, 5 mol%, 10 mol%, 15 mol%, and 20 mol%) on the composition, morphologies and optical properties of Mn-doped ZnO nanoparticles have been investigated through EDX, FTIR, SEM, UV-visible spectroscopy, and fluorescence spectra.

## Conflict of Interests

The authors declare that they have no conflict of interests regarding the publication of this paper.

## Acknowledgment

The authors would like to thank the University of Malaya for sponsoring this work under the University Malaya Research Grant (UMRG RP022-2012A) and the Bright Sparks Program.

## References

- [1] H. D. Raval and J. M. Gohil, "Nanotechnology in water treatment: an emerging trend," *International Journal of Nuclear Desalination*, vol. 4, no. 2, pp. 184–188, 2010.
- [2] J. Iqbal, X. Liu, A. Majid, and R. Yu, "Synthesis and physical properties of Mn doped ZnO dilute magnetic semiconductor nanostructures," *Journal of Superconductivity and Novel Magnetism*, vol. 24, no. 1-2, pp. 699–704, 2011.
- [3] L. W. Wang, Z. Xu, F. J. Zhang, S. L. Zhao, and L. F. Lu, "Structure, optical, and magnetic properties of Mn-doped ZnO films prepared by sputtering," *International Journal of Minerals, Metallurgy and Materials*, vol. 17, no. 4, pp. 475–480, 2010.
- [4] W. Shi-Wei, Z. Ming-Yuan, Z. Min et al., "Effects of pulsed magnetic field on Mn-doped ZnO diluted magnetic semiconductor prepared by hydrothermal method," *Acta Physica Sinica*, vol. 61, no. 19, Article ID 198103, 2012.
- [5] X. X. Yan and G. Y. Xu, "Effect of sintering atmosphere on the electrical and optical properties of  $(\text{ZnO})_{1-x}(\text{MnO}_2)_x$  NTCR ceramics," *Physica B*, vol. 404, no. 16, pp. 2377–2381, 2009.
- [6] Y. Abdollahi, A. Abdullah, Z. Zainal, and N. Yusof, "Synthesis and characterization of Manganese doped ZnO nanoparticles," *International Journal of Basic and Applied Sciences*, vol. 11, no. 4, pp. 62–69, 2011.
- [7] B. Soni, M. P. Deshpande, S. Bhatt, N. Garg, N. Pandya, and S. H. Chaki, "Influence of Mn doping on optical properties of ZnO nanoparticles synthesized by microwave irradiation," *Journal of Optics*, vol. 42, no. 4, pp. 328–334, 2013.
- [8] O. D. Jayakumar, H. G. Salunke, R. M. Kadam, M. Mohapatra, G. Yaswant, and S. K. Kulshreshtha, "Magnetism in Mn-doped ZnO nanoparticles prepared by a co-precipitation method," *Nanotechnology*, vol. 17, no. 5, pp. 1278–1285, 2006.
- [9] M. Yang, Z. X. Guo, K. H. Qiu et al., "Synthesis and characterization of Mn-doped ZnO column arrays," *Applied Surface Science*, vol. 256, no. 13, pp. 4201–4205, 2010.
- [10] S. Senthilkumaar, K. Rajendran, S. Banerjee, T. K. Chini, and V. Sengodan, "Influence of Mn doping on the microstructure and optical property of ZnO," *Materials Science in Semiconductor Processing*, vol. 11, no. 1, pp. 6–12, 2008.
- [11] M. Y. Hao, S. Y. Lou, S. M. Zhou, R. J. Yuan, G. Y. Zhu, and N. Li, "Structural, optical, and magnetic studies of manganese-doped zinc oxide hierarchical microspheres by self-assembly of nanoparticles," *Nanoscale Research Letters*, vol. 7, no. 100, pp. 1–13, 2012.
- [12] D. Wu, Z. Huang, G. Yin et al., "Preparation, structure and properties of Mn-doped ZnO rod arrays," *CrystEngComm*, vol. 12, no. 1, pp. 192–198, 2010.
- [13] R. Viswanatha, S. Sapra, S. S. Gupta et al., "Synthesis and characterization of Mn-doped ZnO nanocrystals," *Journal of Physical Chemistry B*, vol. 108, no. 20, pp. 6303–6310, 2004.
- [14] L. Irimpan, V. P. N. Nampoori, P. Radhakrishnan, A. Deepthy, and B. Krishnan, "Size dependent fluorescence spectroscopy of nanocolloids of ZnO," *Journal of Applied Physics*, vol. 102, no. 6, Article ID 063524, 2007.
- [15] F. I. Ezema and U. O. A. Nwankwo, "Effect of concentration of Mn dopant ions on the structural and optical properties of zinc oxide crystals," *Digest Journal of Nanomaterials and Biostructures*, vol. 6, no. 1, pp. 271–278, 2011.



## Research Article

# Electroluminescent Devices Based on Junctions of Indium Doped Zinc Oxide and Porous Silicon

**F. Severiano,<sup>1</sup> G. García,<sup>2</sup> L. Castañeda,<sup>3</sup> J. M. Gracia-Jiménez,<sup>1</sup>  
Heberto Gómez-Pozos,<sup>4</sup> and J. A. Luna-López<sup>2</sup>**

<sup>1</sup> Instituto de Física, Benemérita Universidad Autónoma de Puebla, Apartado Postal J-48, 72570 Puebla, PUE, Mexico

<sup>2</sup> CIDS-ICUAP, Benemérita Universidad Autónoma de Puebla, 14 Sur y Avenida San Claudio, Edificio 137, 72570 Puebla, PUE, Mexico

<sup>3</sup> Escuela Superior de Ingeniería Mecánica y Eléctrica Unidad Ticomán, Instituto Politécnico Nacional, 07340 México, DF, Mexico

<sup>4</sup> Área Académica de Computación, ICBI, Universidad Autónoma del Estado de Hidalgo, Mineral de la Reforma, Hidalgo, Apartado Postal 42000, Mexico

Correspondence should be addressed to F. Severiano; [pacosco@ifuap.buap.mx](mailto:pacosco@ifuap.buap.mx)

Received 23 September 2013; Revised 11 November 2013; Accepted 6 December 2013; Published 6 January 2014

Academic Editor: Gon Namkoong

Copyright © 2014 F. Severiano et al. This is an open access article distributed under the Creative Commons Attribution License, which permits unrestricted use, distribution, and reproduction in any medium, provided the original work is properly cited.

Electroluminescent devices (ELD) based on junctions of indium doped zinc oxide (ZnO:In) and porous silicon layers (PSL) are presented in this work. PSL with different thicknesses and photoluminescent emission, around 680 nm, were obtained by anodic etching. PSL were coated with a ZnO:In film which was obtained by ultrasonic spray pyrolysis technique. Once obtained, this structure was optically and electrically characterized. When the devices were electrically polarized they showed stable electroluminescence (EL) which was presented as dots scattered over the surface. These dots can be seen with the naked eye. The observed EL goes from the 410 to 1100 nm, which is formed by different emission bands. The EL emission in the visible region was around 400 to 750 nm, and the emission corresponding to the infrared part covers the 750 to 1150 nm. The electrical characterization was carried out by current-voltage curves (*I-V*) which show a rectifying behavior of the devices. Observed electroluminescent dots are associated with the electron-hole injection into quantized states in PS as well as the emission from the ZnO:In film.

## 1. Introduction

Crystalline silicon (c-Si) has been a vital material for the development of the microelectronics industry; however, it is an indirect band semiconductor so that it limits its application to the optoelectronics industry. Nevertheless, the discovery of visible luminescence at room temperature of the porous silicon (PS) has reopened the possibility to obtain electroluminescent silicon based devices [1–3]. The discovery of photoluminescence [1] in PS and the understanding of the growth of nanostructures [2] opened the field to a large amount of work on this material. For practical applications, the electroluminescence (EL) is the crucial point. The development of electroluminescent devices (ELD) in PS technology faces some specific problems. The material has a large internal surface; therefore, it shows a tendency to undergo

a chemical change when it is exposed to air. Furthermore, nanoporous silicon shows a very low electrical conductivity which causes problems for the EL efficiency. However, ELD with wet contacts [4, 5] have proved to be efficient. This shows that, in principle, PS is a good material to get EL. Most of the ELD present a simple integrated structure of a porous layer and a contact layer on top. For contact, thin metals such as gold, indium tin oxide (ITO), silicon carbide, and conductive polymers are used. An advanced structure has p-n junction within the porous region. For this work, we propose to use a ZnO:In film. ELD with this kind of structure (ZnO:In/SP) has been obtained before but this is the first time that the different components are obtained with techniques of low cost equipment (ultrasonic spray pyrolysis (USP) and anodic etching). Zinc oxide (ZnO) is classified as a semiconductor n-type because it generally has an excess of zinc [6]. ZnO has



an attractive direct gap (3.37 eV) which can be modified to be applied to electrical and optical devices [7]. ZnO:In exhibits both a high optical transmittance in the visible region of the spectrum (between 60 and 80%) and a low resistivity (on the order of  $2\text{E-}10\ \Omega\text{-cm}$ ) [8] making it an important material in the manufacture of heat mirrors used on gas stoves and also as conductive coating that prevents ice formation on aircraft windows and electrodes in solar cells based on amorphous silicon [9, 10]. The zinc oxide, used in this work, was obtained by ultrasonic spray pyrolysis technique. This method is highly reproducible and can be used at room temperature and for coating large substrates although it does not require a vacuum system. The doped films are stable even when the temperature changes (25–400°C) in the presence of air [11]. Furthermore, ZnO:In thin films do not require extra postannealing treatments in order to obtain low resistivity values in the range of  $5 \times 10^{-3}\ \Omega\text{-cm}$  [12]. Due to the characteristics exhibited in these films, we used them as a coating of the PSL.

In this paper, we report fundamental characteristics of a ZnO:In/PS/p-Si diode in terms of the relation between the EL intensity and the operating variables (operation, current density, and thickness of the porous layer) as well as the relation between the EL and PL spectra. This investigation about the EL properties of this kind of structure will help to clarify the EL mechanism of PS-based devices.

## 2. Experimental Details

PSL were obtained by anodic etching. This process was carried out in a teflon cell designed so that the electrolyte which consists of hydrofluoric acid (HF) and ethanol ( $\text{CH}_3\text{-CH}_2\text{-OH}$ ) has contact with the c-Si top surface to be attacked. The cathode is formed by a platinum mesh similar in size to the area of the c-Si exposed to the electrolyte. Moreover, the anode is formed by an aluminum (Al) plate. PSL were obtained of c-Si p-type with a resistivity of 2–4  $\Omega\text{-cm}$ . The used electrolyte was composed of a mixture of hydrofluoric acid (HF) (Merck 40% by volume) and ethanol ( $\text{CH}_3\text{-CH}_2\text{-OH}$ ) (Alfa-Aesar 99.98% by volume) in a ratio 1:2, respectively. The current density to obtain the PSL was  $6.49\ \text{mA/cm}^2$ ; the time of etching was 10, 20, and 30 min.

A laser with a wavelength of 405 nm and 40 mW of power was used to excite the sample in PL measurements of the PSL; the range detected by the monochromator was from 400 to 1100 nm. The thickness of the PSL was estimated by gravimetry; the thickness obtained by this method was compared with physical measurements performed by profilometry.

The thickness of the PSL was obtained by the expression [13, 14]

$$E = \frac{m_1 - m_2}{\rho A_a}, \quad (1)$$

where  $m_1$  is the mass of the wafer of c-Si before the attack,  $m_2$  is the mass of the same wafer after removing the porous layer,  $\rho$  is the density of the c-Si (in  $\text{g/cm}^3$ ), and  $A_a$  is the attacked area during the anodization (in  $\text{cm}^2$ ).

The thickness of the PSL was measured by a Dektak 150 profilometer (this equipment allows measuring film

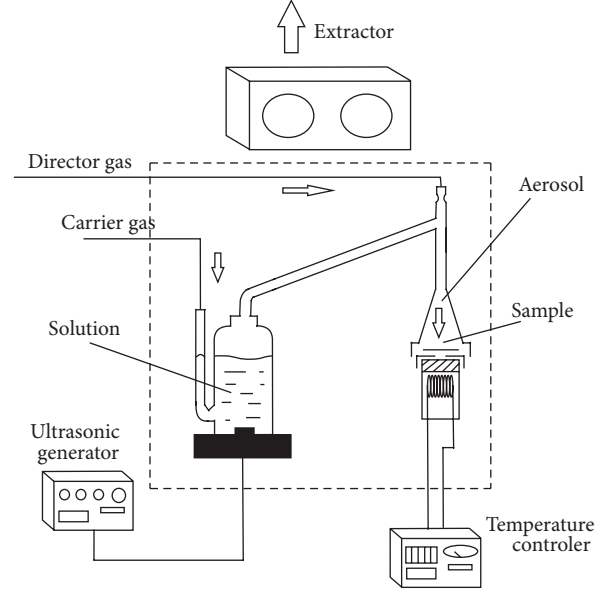


FIGURE 1: Schematic diagram of the experimental setup used for depositing the ZnO:In thin films.

thicknesses below 100 Å). This analysis was conducted after the porous layer was removed using a solution of NaOH.

ZnO:In thin solid films were prepared using the ultrasonic spray pyrolysis (USP) technique which is a versatile technique that can be used to produce nanoscale sized powders and thin solid films. The deposition system used to obtain the ZnO:In thin film presented in this work includes a piezoelectric transducer which operates at variable frequency and that was set to 1.2 MHz and the ultrasonic power at 120 W. ZnO:In thin films were deposited from a 0.2 M solution of zinc acetate ( $[\text{Zn}(\text{O}_2\text{CCH}_3)_2]$  from Alfa, 98%), dissolved in a mix of deionized water, acetic acid ( $[\text{CH}_3\text{CO}_2\text{H}]$  from Baker, 95%), and methanol ( $[\text{CH}_3\text{OH}]$  from Baker, 98%). Separately, a 0.2 M solution of indium acetate ( $[\text{In}(\text{CH}_3\text{CO}_2)_3]$  from Alfa, 98%) dissolved in a mix of deionized water and acetic acid (1:1, volume proportion) was prepared in order to be used as a doping solution. The substrate temperature ( $T_s$ ) was kept constant at 430°C. Pure  $\text{N}_2$  (from PRAXAIR, 99.997%) was used as solution carrier and a director gas with flow rates of 3.5 and  $0.5\ \text{L}\cdot\text{min}^{-1}$ , respectively. Figure 1 shows a schematic diagram of the experimental setup used for depositing the ZnO:In thin films (ultrasonic spray pyrolysis: USP).

The thickness of the ZnO:In thin films was measured by a KLA profilometer (Tencor model P15 with a resolution of 1.5 nm) from a step formed during deposition. All the samples were grown with a film thickness value of 600 nm approximately. The microcrystalline structure of the samples was studied with X-ray diffraction analysis, obtained in a Siemens D5000 diffractometer by using the Cu-K1 ( $\lambda = 0.154056\ \text{nm}$ ) radiation and the  $\theta$ -2 $\theta$  technique. The optical transmittance spectra at normal incidence of the ZnO:In film were obtained by a double-beam Shimadzu 2401 PC spectrophotometer in the UV-Vis region (350–1000 nm) without glass substrate correction. Electrical sheet resistance of the ZnO:In was

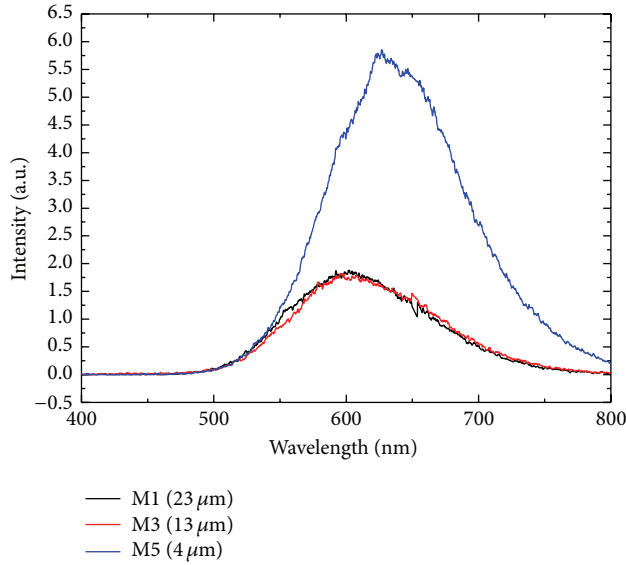


FIGURE 2: PL spectra for the PSL utilized to get the ELD.

measured by the conventional four-aligned probe method (Veeco equipment) with the appropriate geometric correction factors.

The optical characterization of the ELD was obtained with a monochromator model iHR320 HORIBA brand Jobin Yvon which is coupled to a CCD detector model iHR320 brand Synapse; the range detected by the monochromator was from 300 to 1100 nm. The resolution of this equipment is 0.06 nm, whereas the scanning speed is 160 nm/seg and an accuracy of 0.20 nm wavelength. EL spectra were obtained by applying different currents of operation to the device. The electrical characterization was carried out with a Keithley 2000 multimeter through which variable current was applied to ELD; the data were monitored by a LabTracer program through which current-voltage ( $I$ - $V$ ) curves were obtained.

### 3. Results and Discussions

**3.1. PL of PS.** We proceeded to get three samples with different thicknesses to obtain the ELD and carry out the proposed study. Figure 2 shows the result of the optical analysis performed. The used electrochemical etching current was of  $6.49 \text{ mA/cm}^2$ ; this current was selected because it had shown the highest PL intensity in previous analyses. The obtained sample with this current density showed the highest PL intensities because this current favors the obtaining of silicon filaments that are emitted in the visible region. The etching times were 10, 20, and 30 min, corresponding to thickness of 4(M5), 13(M3), and 23(M1)  $\mu\text{m}$ , respectively. Figure 2 shows that, by increasing the anodized time, the maxima of the curves show a shift to higher energies and it is observed that the peaks intensity decreases. This shift goes from 650 to 600 nm. This is due to the reduction of the emitting silicon filaments size present in the PS structure [15], and the intensity decrease is the result of the oxidation process which takes place in the PSL [16]. This process reduces the filament

TABLE 1: Thickness of the PSL obtained by gravimetry and profilometry.

Sample	Thickness ( $\mu\text{m}$ )	Profilometry ( $\mu\text{m}$ )
M1	23	21
M3	13	12
M5	4	3.5

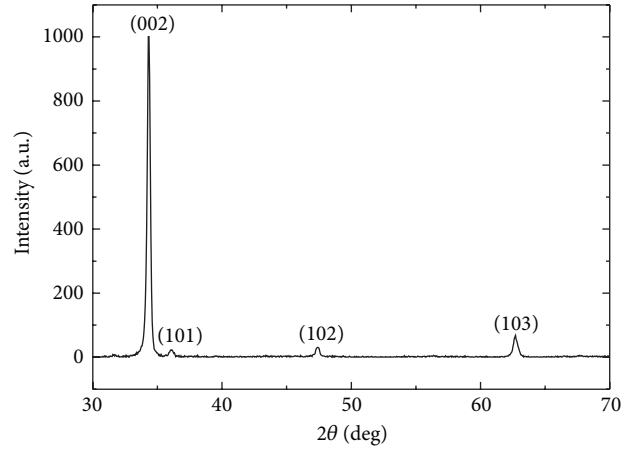


FIGURE 3: Diffraction pattern of the ZnO:In film deposited at  $430^\circ\text{C}$ .

size until the filaments lose their capacity to emit light. As it can be seen the samples show an increase in the PL inversely proportional to the thickness of the PSL. This is the typical behavior of this kind of samples. These three samples were used in obtaining the devices.

**3.2. Thickness of the PSL.** Table 1 shows the thicknesses of the PSL (obtained with a current density of  $6.49 \text{ mA/cm}^2$ ) calculated by (1) and the profilometry results. We can see that the results between gravimetry and profilometry show good agreement ( $\pm 5\%$ ).

**3.3. ZnO:In Characterization.** ZnO:In film was obtained from the precursor solution as it was described before, the  $T_s$  was kept constant at  $430^\circ\text{C}$ , and time growth was 10 minutes in all cases. This is the temperature of the PSL when the ZnO:In film was deposited to get the devices. X-ray diffraction patterns obtained from ZnO:In thin films show polycrystalline characteristics and the corresponding peaks fit well to a hexagonal ZnO:In wurtzite type structure. Figure 3 shows the pattern of ZnO:In thin films.

The crystallite size was estimated using the (002) and (100) diffraction peaks from the XRD data in accordance with the Debye-Scherrer formula [17]. According to the results, the crystallite size of the ZnO:In thin films is around 23 to 36 nm.

Figure 4 shows the optical transmittance spectra of ZnO:In thin film deposited on soda-lime glass substrate. No substrate correction was made to the corresponding measurement. Average transmittance of the obtained film is suited for transparent conductive oxide (TCO) application. Optical band gap was calculated from the plot of  $(\alpha h\nu)^2$  as a function

TABLE 2: ZnO:In films electric resistivity.

Sample	Average thickness (nm) $\pm 5.0\%$	Average transmittance (400–700 nm) (%)	Electrical resistivity $\times 10^{-3}$ ( $\Omega\text{cm}$ ) $\pm 5.0\%$	Band gap (eV) $\pm 5.0\%$
ZnO:In/SLGS	685	53.11	2.05	3.44

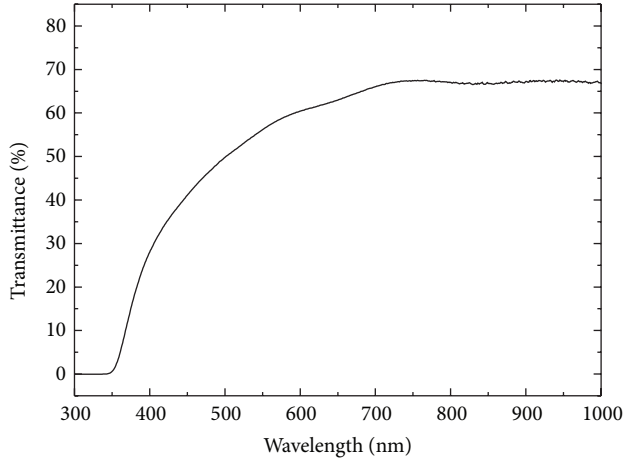
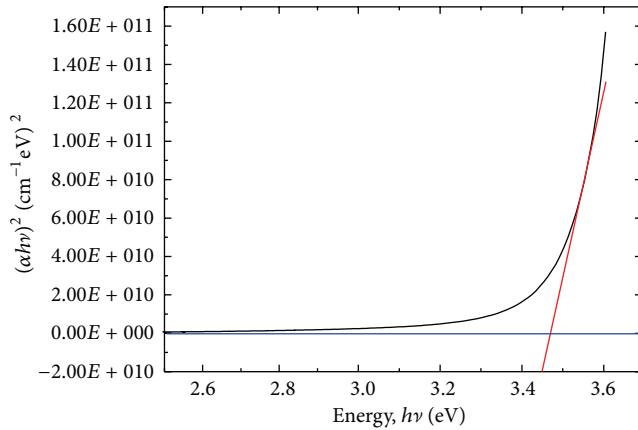


FIGURE 4: The optical transmittance is about 53%.

FIGURE 5: Plot of  $(\alpha h\nu)^2$  versus  $h\nu$  and estimate of the band gap.

of  $h\nu$ , where  $\alpha$  is the optical absorption coefficient and  $h\nu$  is the energy of the incident photons. From these curves, the optical band gap ( $E_g$ ) values can be estimated by the extrapolation of straight line to  $(\alpha h\nu) = 0$ . Figure 5 shows band gap value (3.44 eV).

Table 2 shows the electrical resistivity value and the principal characteristics for ZnO:In thin film deposited on soda-lime glass substrate (SLGS). Electrical sheet resistance of the sample was measured by the conventional four-aligned probe method.

Both optical and electrical characterization show that the ZnO:In films possess the necessary properties to be used as an electrical contact and as a transparent coating to get ELD based on PSL.

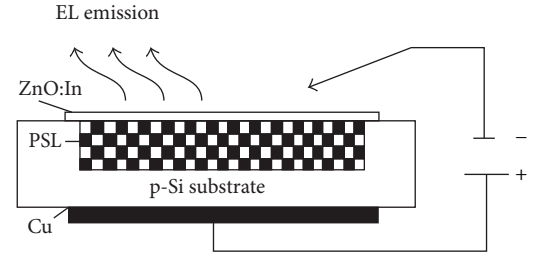


FIGURE 6: Schematic diagram of the ELD structure.

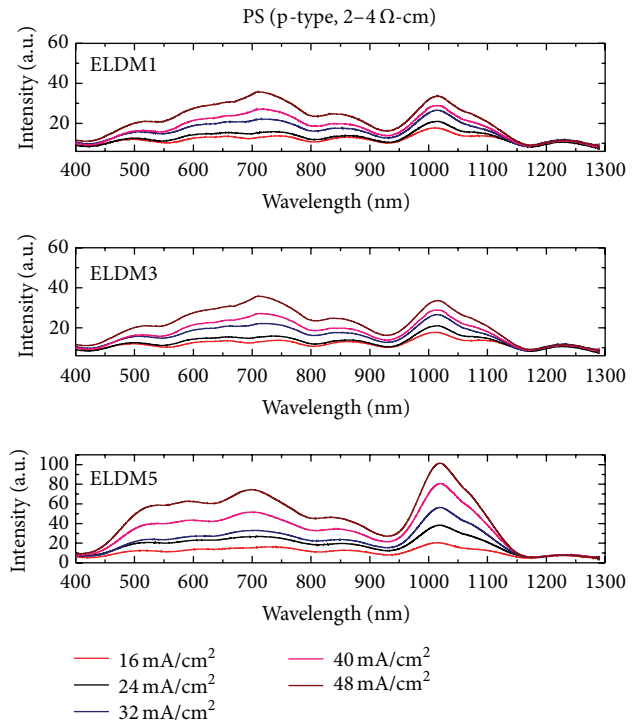


FIGURE 7: EL spectra obtained from the ELD. We can see the response of the device with different current densities.

#### 4. Results and Discussion of ELD

Figure 6 shows the distribution of the components of the ELD. EL responses were obtained from devices taken by applying DC current. The negative terminal was connected to the ZnO:In film through a needle probe (we say that our device is forward polarized); the device presented luminescent spots on the surface which were visible to the naked eye.

Figure 7 shows the EL spectra of the ELD labeled ELDM1, ELDM3, and ELDM5 which have thicknesses of 23, 13 and 4  $\mu\text{m}$ , respectively. In the spectra we can see that the EL

emission goes from 400 to 1100 nm for all samples and the EL intensity increases with the increasing of the operating current density. Based on the spectra and the images taken from the devices, the emitted light is white. The sample that showed the best performance in the visible and infrared part was the sample labeled as ELDM5 ( $4\ \mu\text{m}$ ). In the visible part of the spectra three principal peaks centered at 500, 600, and 710 nm are seen, and in the infrared region one principal peak centered at 1020 nm is observed. The emissions observed in the visible region are attributed to the PS and the ZnO:In film. The emission centered at 600 nm is due to the presence of silicon filaments which have different diameters (nanosized) and that are present in the PS as we can see in the PL characterization. This changes their bandwidth and thereby the wavelength that is emitted [18–21]. The emission centered at 500 is the characteristic blue-green (BG) emission band (broad fluorescence band) typically observed in ZnO films, and it is due to the transition from the conduction band to the  $O_{\text{zn}}$  level [22]. The peak at 710 nm might be due to the emission from a level caused by oxygen interstitials attributed to ZnO:In; the measure of the peaks associated with the ZnO film was performed by Castañeda in previous works [22]. The emission that is observed in the IR might be due to the crystalline silicon substrate, since there are reports which say that the silicon is emitted in that region [18, 23]. This would explain the fact that the corresponding emission to this region is increased to reduce the thickness of the porous film, allowing the contribution of the substrate to be observed in a better way when the device is polarized. Comparing the obtained results of PL and EL, we can conclude that the intensity of the EL emission of the devices is directly related to the PL than the PSL present. This is evident since the EL intensity is directly related to the PL behavior; as it can be seen in Figure 2, the sample with the highest PL intensity is the same sample with higher EL intensity. The sample that showed the best PL and EL was the sample with a thickness of  $4\ \mu\text{m}$ ; this is due to the high concentration of emitting filaments present in this sample which is reflected in the intensity of the spectra obtained. Through the analysis of the obtained results, we can observe that in order to improve the functioning of this kind of devices, we have to find the way to improve the PL of PS.

**4.1. Comparison between PL and EL.** Figure 8 shows a comparison between the PL and EL spectra obtained from ELDM5 device. This gives us evidence to explain the origin of emissions in the devices. In the PL spectra of the ELD, emissions that are from 400 to 800 nm are related to the PS and the ZnO:In film. Figure 2 shows that the main peak of PS emission is around the 600 nm, and as we said before there are works that report emissions from ZnO:In in 500 and 710 nm. This explains the observed peaks in the PL spectra of the ELD (black in Figure 8). Now if we compare the PL and the EL spectra of the ELD, the EL spectra show a main peak around 1020 nm. We related this emission to the silicon substrate. The IR band cannot be observed in the PL because the laser penetrates only slightly in the sample [24]; moreover, the electric current goes through the entire sample, exciting

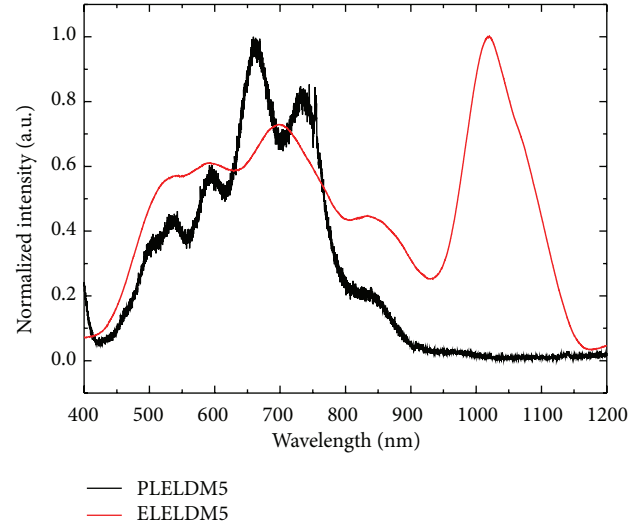


FIGURE 8: Comparison between PL and EL spectra of the ELD.

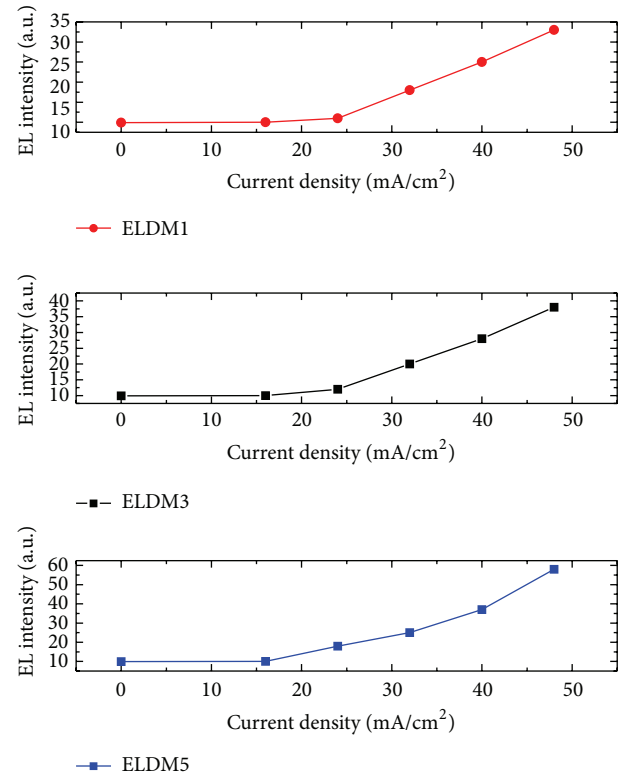


FIGURE 9: Plot of EL versus operation current density. We can see two regions which exhibit a linear relationship.

also the substrate; for this reason the silicon substrate can only be appreciated in the EL spectra.

#### 4.2. EL Analysis

**4.2.1. Relation between EL Intensity and Current Density.** Figure 9 shows the behavior of the EL as a function of the



operating current density applied to the obtained devices. The graph shows that the EL intensity increases when increasing the operation current density; this behavior is observed in all the studied samples.

We can see two regions which exhibit a linear relationship; the first region goes from 0 to 15 mA/cm<sup>2</sup> and the second region goes from 15 to 48 mA/cm<sup>2</sup>. This denies the direct excitation of luminescence centers by accelerated carriers as the EL principal excitation mechanism. This suggests that the localized electron-hole pairs are responsible for the visible EL which is created by trapping an electron and hole from the conduction and the valence band, respectively [25]. The deviation from the linear relationship at low current densities implies that there is some current component which does not directly contribute. In other words, a significant amount of current precedes the onset of EL.

**4.3. EL Source.** On the basis of the PL and EL spectra, and the relation between EL intensity and current density analysis, we can conclude that the observed white EL is a combination of red emission from the PS and blue light from the ZnO:In layer when it is excited by the operating current density. In the PS, each emitting filament is supposed to be surrounded by a wide band gap region since it behaves like a quantum dot [26]. The wide gap region may be composed of oxides, hydrides, amorphous Si, or simply a Si nanostructure of smaller dimensions. Thus, the microscopic structure of PS along the direction of current flow can be understood as if the Si nanocrystallites are connected together via wider gap interface regions. When a bias voltage is applied to this ensemble, a stronger electric field may build up preferentially in the wide-gap regions because of their expected lower dielectric constant and higher resistivity. Then, the conduction and valence band edges of the nanocrystallites become shifted with respect to those of respective neighboring ones. This band shift increases when the applied voltage rises. Therefore, under a sufficient high voltage bias, a critical situation would appear locally: the energy position of the valence-band edge of a crystallite becomes comparable with that of the conduction band edge of the neighboring one. In this situation, either of the following two phenomena is expected to occur. First, hot electrons injected from the conduction band of the neighboring one are so energetic that they can create electron-hole pairs by an impact process (process 1). Second, electron-hole pairs can be created also by the tunneling of electrons from the valence band of a crystallite into the conduction band of the next one (process 2). Progress of these processes should significantly increase the number of carriers in the PSL and consequently let a sharp increase in current density at the corresponding voltage. This is similar to the electrical breakdown in reverse biased p-n junctions. Otherwise the electric current excites the oxygen interstitials in the ZnO:In film which originates the blue light that can be seen in the PL and EL spectra.

**4.4. Electrical Characteristics of the DEL.** Figure 10 shows the obtained *I-V* curves from the devices. This is a typical *I-V* curve for a ZnO:In/PS/p-Si structure which shows

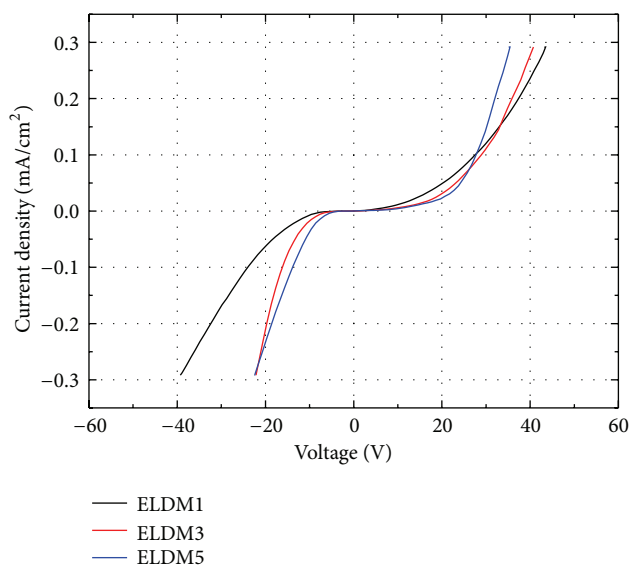


FIGURE 10: *I-V* curves for devices obtained. This is a typical *I-V* curve that shows rectification behavior.

characteristic rectification behavior. The forward direction corresponds to a negative potential on the ZnO:In film. From a forward voltage of around 15 V, spots of white light could be seen by the naked eye in a dimly lit room which merged together as the bias was increased. Closer examination of the EL at lower potentials (approximately 10–15 V) revealed that in addition to the white light small spots on the surface, they emitted red light. At higher current densities, only white light was observed; however, it was not possible to ascertain whether this was due to the previously red spots now emitting white light or if the more intense white light from other regions was simply masking the colored EL from these areas. No light emission was observed under reverse bias.

## 5. Conclusions

ELD from structures based on ZnO:In/SP which exhibit emission in the visible and infrared region of the electromagnetic spectrum were obtained. We demonstrated stable white light emission from ZnO:In/PS structures through EL and PL spectra. The device presented luminescent spots on the surface which were visible to the naked eye. It was shown that the EL emission is related to the PL behavior of the PSL used to obtain the devices. It was proved that the EL emission is integrated by the emission of ZnO:In, PS, and the silicon substrate. Also the results indicate that the thickness of the porous layer is very important in the electrical behavior because the devices tend to behave as a diode.

## Conflict of Interests

The authors declare that there is no conflict of interests regarding the publication of this paper.



## Acknowledgments

F. Severiano thanks CONACyT for its support through 33741 studentship. Heberto Gómez-Pozos acknowledges financial support from the Programa de Mejoramiento del Profesorado from the SEP México through Project no. PROMEP/103.5/11/0144. The authors also acknowledge S & C Associates for proof-reading of the paper.

## References

- [1] L. T. Canham, "Silicon quantum wire array fabrication by electrochemical and chemical dissolution of wafers," *Applied Physics Letters*, vol. 57, no. 10, pp. 1046–1048, 1990.
- [2] V. Lehmann and U. Gösele, "Porous silicon formation: a quantum wire effect," *Applied Physics Letters*, vol. 58, no. 8, pp. 856–858, 1991.
- [3] C. Pickering, M. I. J. Beale, D. J. Robbins, P. J. Pearson, and R. Greef, "Optical studies of the structure of porous silicon films formed in p-type degenerate and non-degenerate silicon," *Journal of Physics C*, vol. 17, no. 35, pp. 6535–6552, 1984.
- [4] J. C. Vial, A. Bsiesy, F. Gaspard et al., "Mechanisms of visible-light emission from electro-oxidized porous silicon," *Physical Review B*, vol. 45, no. 24, pp. 14171–14176, 1992.
- [5] A. Bsiesy, F. Muller, M. Ligeon et al., "Optical properties of low dimensional silicon structures," in *Proceedings of the NATO Advanced Research Workshop*, Meylan, France, 1993.
- [6] T. Okamura, Y. Seki, S. Nagakari, and H. Okushi, "Junction properties and gap states of ZnO thin film prepared by sol-gel process," *Japanese Journal of Applied Physics*, vol. 31, pp. 3218–3220, 1992.
- [7] L. Castañeda, A. García-Valenzuela, E. P. Zironi, J. Cañetas-Ortega, M. Terrones, and A. Maldonado, "Formation of indium-doped zinc oxide thin films using chemical spray techniques: the importance of acetic acid content in the aerosol solution and the substrate temperature for enhancing electrical transport," *Thin Solid Films*, vol. 503, no. 1–2, pp. 212–218, 2006.
- [8] A. Guillen-Santiago, M. D. L. L. Olvera, and A. Maldonado, "Películas delgadas de ZnO:F depositadas por rocío químico: efecto de la temperatura de sustrato sobre las propiedades físicas," *Superficies y Vacío*, vol. 13, pp. 77–79, 2001.
- [9] K. L. Chopra, S. Major, and D. K. Pandya, "Transparent conductors—a status review," *Thin Solid Films*, vol. 102, no. 1, pp. 1–46, 1983.
- [10] M. A. Martínez, J. Herrero, and M. T. Gutiérrez, "Deposition of transparent and conductive Al-doped ZnO thin films for photovoltaic solar cells," *Solar Energy Materials and Solar Cells*, vol. 45, no. 1, pp. 75–86, 1997.
- [11] P. S. Patil, "Versatility of chemical spray pyrolysis technique," *Materials Chemistry and Physics*, vol. 59, no. 3, pp. 185–198, 1999.
- [12] J. F. Guillemoles, D. Lincot, P. Cowache, and J. Vedel, "Solvent effect on ZnO thin films prepared by spray pyrolysis," in *Proceedings of the 10th European Photovoltaic Solar Energy Conference*, A. Luque, G. Sal, W. Pals, G. dos Santos, and P. Helm, Eds., pp. 609–612, Lisbon, Portugal, 1991.
- [13] J. J. Yon, K. Barla, R. Herino, and G. Bomchil, "The kinetics and mechanism of oxide layer formation from porous silicon formed on p-Si substrates," *Journal of Applied Physics*, vol. 62, no. 3, pp. 1042–1048, 1987.
- [14] Z. Fekin, F. Z. Otmani, N. Ghellai, and N. E. Chabanne-Sari, "Characterization of the porous silicon layers," *The Moroccan Journal of Condensed Matter*, vol. 7, no. 1, pp. 35–37, 2006.
- [15] P. Kumar, "Effect of silicon crystal size on photoluminescence appearance in porous silicon," *ISRN Nanotechnology*, vol. 2011, Article ID 163168, 6 pages, 2011.
- [16] R. Herino, "Luminescence of porous silicon after electrochemical oxidation," in *Porous Silicon Science and Technology*, pp. 53–66, 1995.
- [17] B. E. Warren, *X-Ray Diffraction*, Dover, New York, NY, USA, 1990.
- [18] T. P. Pearsall, J. C. Adams, J. N. Kidder Jr. et al., "Bright visible photoluminescence in thin silicon films," *Thin Solid Films*, vol. 222, no. 1–2, pp. 200–204, 1992.
- [19] W. Lang, P. Steiner, and F. Kozlowski, "Porous silicon electroluminescent devices," *Journal of Luminescence*, vol. 57, pp. 341–349, 1993.
- [20] G. Hu, S. Q. Li, H. Gong et al., "White light from an indium zinc oxide/porous silicon light-emitting diode," *The Journal of Physical Chemistry C*, vol. 113, no. 2, pp. 751–754, 2009.
- [21] Y. Zhao, D. Yang, L. Lin, and D. Que, "Blue light emission of porous silicon subjected to RTP treatments," *Chinese Science Bulletin*, vol. 51, no. 22, pp. 2696–2699, 2006.
- [22] L. Castañeda, O. G. Morales-Saavedra, J. C. Cheang-Wong et al., "Influence of indium concentration and substrate temperature on the physical characteristics of chemically sprayed ZnO:In thin films deposited from zinc pentanedionate and indium sulfate," *Journal of Physics Condensed Matter*, vol. 18, no. 22, pp. 5105–5120, 2006.
- [23] S. S. Iyer and Y.-H. Xie, "Light emission from silicon," *Science*, vol. 40, pp. 40–46, 1993.
- [24] N. Koshida, H. Koyama, Y. Suda et al., "Optical characterization of porous silicon by synchrotron radiation reflectance spectra analyses," *Applied Physics Letters*, vol. 63, pp. 2774–2776, 1993.
- [25] T. Oguro, H. Koyama, T. Ozaki, and N. Koshida, "Mechanism of the visible electroluminescence from metal/porous silicon/n-Si devices," *Journal of Applied Physics*, vol. 81, no. 3, pp. 1407–1412, 1997.
- [26] S. Schuppler, S. L. Friedman, M. A. Marcus et al., "Dimensions of luminescent oxidized and porous silicon structures," *Physical Review Letters*, vol. 72, no. 16, pp. 2648–2651, 1994.

## Research Article

# The Effect of Thermal Annealing Processes on Structural and Photoluminescence of Zinc Oxide Thin Film

Huai-Shan Chin and Long-Sun Chao

*Department of Engineering Science, National Cheng Kung University, 1 University Road, Tainan, Taiwan*

Correspondence should be addressed to Long-Sun Chao; [lschao@hflow.es.ncku.edu.tw](mailto:lschao@hflow.es.ncku.edu.tw)

Received 24 September 2013; Revised 28 November 2013; Accepted 29 November 2013

Academic Editor: Hong Seok Lee

Copyright © 2013 H.-S. Chin and L.-S. Chao. This is an open access article distributed under the Creative Commons Attribution License, which permits unrestricted use, distribution, and reproduction in any medium, provided the original work is properly cited.

This study used radio frequency sputtering at room temperature to prepare a zinc oxide (ZnO) thin film. After deposition, the thin film was placed in a high-temperature furnace to undergo thermal annealing at different temperatures (300, 400, 500, and 600°C) and for different dwelling times (15, 30, 45, and 60 min). The objective was to explore the effects that the described process had on the thin film's internal structure and luminescence properties. A scanning electron microscope topographic image showed that the size of the ZnO crystals grew with increases in either the thermal annealing temperature or the dwelling time. However, significant differences in the levels of influence caused by increasing the thermal annealing temperature or dwelling time existed; the thermal annealing temperature had a greater effect on crystal growth when compared to the dwelling time. Furthermore, the crystallization directions of ZnO (002), (101), (102), and (103) can be clearly observed through an X-ray diffraction analysis, and crystallization strength increased with an increase in the thermal annealing temperature. The photoluminescence measurement spectra showed that ultraviolet (UV) emission intensity increased with increases in thermal annealing temperature and dwelling time. However, when the thermal annealing temperature reached 600°C or when the dwelling time reached 60 min, even exhibited a weak green light emission peak.

## 1. Introduction

Because the international community has focused on energy conservation and global warming prevention, white light-emitting diodes (LEDs), which are energy-efficient, environmentally friendly, and safe, have become the new light source of the twenty-first century. This phenomenon has created a substantial market opportunity for white LEDs, and they have gradually become a mainstream product in the market. Although high quality manufacturing technology and stable procedural parameters currently exist for white LEDs, high production costs, operational difficulties related to alternating current (AC), and the inability to provide white-light illumination for large areas highlight the application deficiencies of white LEDs. Consequently, the industry targets these deficiencies as directions for improvement. Thick-film dielectric electroluminescence (TDEL) technology, which comprises electroluminescence components, is currently used by research authorities to actively develop

white light excitation. The TDEL structure is self-emitting, flat, large, and applicable to AC, and it emits uniform light. Consequently, it can ameliorate white LED application insufficiencies, becoming a new-generation white lighting product. If the TDEL technology can replace a part of the white LED market, its future market potential is limitless.

Electroluminescence is a phenomenon of energy emission where high voltages are applied to electrodes on both sides of a phosphor; subsequently, the phosphor is excited and emits light, and electricity is converted into light energy. The emission does not create heat; thus, it is also called "cold light." This type of emission, which uses the electron transition between valence and conduction bands or the collision of high energy electrons with the activator inside a phosphor layer and the luminescent center to excite and emit energy, is different from an LED, which employs the recombination of the electron-hole pair near the p-n junction to emit light. Because the TDEL structures have the advantages of being large-size, low-cost, and non-heat-producing and produce

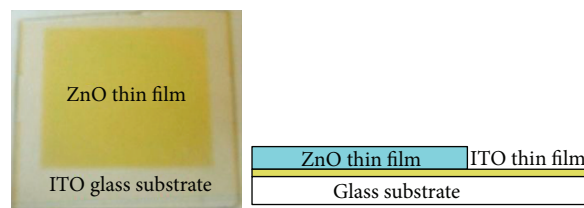


FIGURE 1: The ZnO thin film sample and structure schematic drawing.

uniform emission, they are suitable as fully solidified, large-size emission products, and have great developmental potential for future lighting equipment as an alternative to LCD backlights.

Because ZnO demonstrates abundant sources, low prices, nontoxic characteristics, radiation resistance, high temperature resistance, and chemical stability, it has become an extremely important photoelectric thin film material. Common ZnO thin film production methods include spray pyrolysis [1], metal organic chemical vapor deposition [2, 3], sputtering methods [4–6], thermal oxidation [7], and sol-gel methods [8–10]. Because the sputtering method is nonpolluting and exhibits superior thin film adhesion, flexibility in changing the partial pressure ratio of reactive gases, and stoichiometric qualities that effectively control thin film growth, it is currently the most commonly studied ZnO thin film preparation method.

Because ZnO at room temperature has an optical band gap of 3.3 eV and an extremely large exciton binding energy of 60 meV [11–13], it can potentially be used as an ultraviolet (UV) light source. This study focuses on the exploration of the fluorescent material ZnO:Zn, which is known for its high efficiency and low voltage excitation. To avoid contamination by impurities of traditional electrophoretic deposition or screen printing, which decreases the fluorescent material's emitted luminosity and lifespan, radio frequency (RF) sputtering was employed at room temperature to deposit ZnO thin film (ZnO:Zn). The exploration of the ZnO thin film's internal structure and changes in UV emission properties were conducted by changing thermal annealing procedural parameters.

## 2. Experimental Procedure

This study employed RF sputtering to deposit a ZnO:Zn thin film on an indium tin oxide (ITO) glass substrate at room temperature. Different thermal annealing parameters were used to explore changes in the thin film's structural organization and constituent properties and how these changes influence the ZnO thin film's UV emission properties. Prior to the experiment, the substrate was ultrasonically cleaned with acetone, isopropanol, and deionized water separately for 30 min and then dried. A sputtering system was then employed to deposit a ZnO thin film on the substrate. This experiment used a 99.99% pure Zn target and introduced oxygen ( $O_2$ ) and argon (Ar) during the preparation process as the reactive gases for sputtering. The sputtering parameters comprised a fixed sputtering power of 100 W, 30%  $O_2$

concentration, sputtering pressure of  $5 \times 10^{-3}$  torr, and a deposition time of 30 min. The completed ZnO thin film sample is as shown in Figure 1.

After deposition, the ZnO thin film was placed in a high-temperature furnace under atmospheric conditions. A  $10^\circ\text{C}/\text{min}$  temperature heating rate was used to raise the temperature to  $300^\circ\text{C}$ ,  $400^\circ\text{C}$ ,  $500^\circ\text{C}$ , and  $600^\circ\text{C}$  for thermal annealing. A dwelling time of 15 min, 30 min, 45 min, and 60 min was adopted in the experiment. These analyses were employed for an in-depth exploration of how different thermal annealing parameters affected the ZnO thin film's internal structure and UV emission properties.

## 3. Results and Discussion

Figure 2 is an SEM surface and cross section topographical image of a ZnO thin film without thermal annealing. The image clearly shows that the surface of the as-deposited ZnO thin film is flat, the thin film's internal structure is loose, and crystals did not grow significantly. This is because the low- $O_2$ , low-pressure sputtering environment created by the 30%  $O_2$  concentration and  $5 \times 10^{-3}$  torr sputtering pressure caused the thin film deposition rate to accelerate, and because the rapid stacking of the atoms easily caused the thin film's interior to exhibit an amorphous morphology of small particle accumulation.

Figure 3 shows the XRD diffraction analysis of the as-deposited ZnO thin film. These results reveal that not only the ZnO peaks but also a Zn (101) peak. This is because  $O_2$  (atomic weight: 15.999) is a lighter particle, and in the low-pressure sputtering environment, an  $O_2$  atmosphere can easily be pulled out, leaving a higher quantity of the heavier Ar gas (atomic weight: 39.948). An insufficient  $O_2$  concentration in the chamber not only increases the rate of thin film deposition but also causes the sputtered Zn atoms to form a ZnO thin film with a high Zn content (ZnO:Zn) [14] because of insufficient oxidization. This result can be confirmed through an EDS analysis (Figure 4). The figure shows a significant difference in Zn: $O_2$  ratio, which indicates that low- $O_2$ , low-pressure sputtering can easily lead to a higher Zn content in the ZnO thin film.

Figures 5(a), 5(b), 5(c), and 5(d) are SEM topographical profiles for thermal annealing at  $300^\circ\text{C}$ ,  $400^\circ\text{C}$ ,  $500^\circ\text{C}$ , and  $600^\circ\text{C}$ , under atmospheric conditions, and for 30 min. The images clearly show that the thin film thickness increased with an increase in thermal annealing temperature. The crystals in the thin film also show a tendency to increase in size. When the ZnO thin film (ZnO:Zn) prepared in the

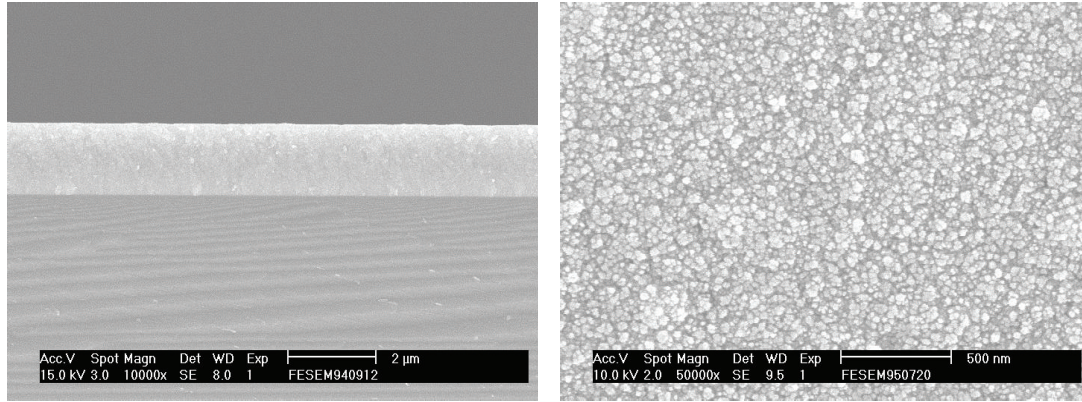


FIGURE 2: SEM surface and cross section topographical image of the as-deposited ZnO thin film.

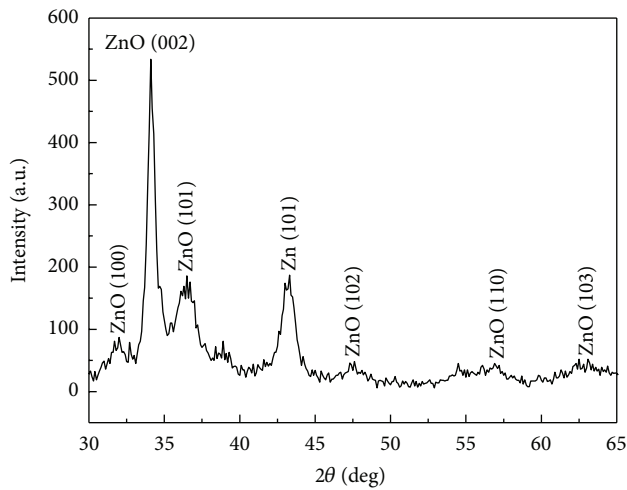


FIGURE 3: XRD diffraction analysis of the as-deposited ZnO thin film.

experiment was thermally annealed at 300°C, it exhibited a morphology of small particle accumulation in the internal structure because of the low temperature that resulted in limited reaction of the excess Zn. This was similar to the ZnO thin film structure that has not been thermally annealed. When the thermal annealing temperature increased to 400°C, the thin film's internal structure began to exhibit a molten state. When the thermal annealing temperature approached the Zn melting point (419.58°C), a portion of the excess Zn in the thin film melted. At a 500°C thermal annealing temperature, the thin film's internal crystal growth was significant and exhibited many holes because the high-temperature thermal annealing caused the Zn in the thin film to dissipate. When thermal annealing temperature reached 600°C, because the temperature was higher, not only was the crystal growth more apparent, but the Zn dissipation was also more severe, resulting in a greater number of holes.

Figure 6 is the PL spectrogram for different thermal annealing temperatures, where the excitation light source was a 325 nm wavelength helium-neon laser. The testing parameters ranged between 350 nm and 620 nm. The testing

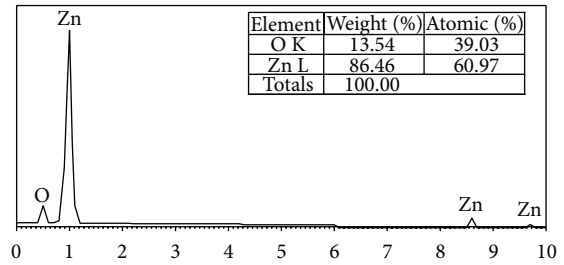


FIGURE 4: EDS analysis of the as-deposited ZnO thin film.

results showed that the UV emission center was located approximately at the 376 nm wavelength. By using the emitting wavelength and band gap conversion formula (1), the calculations clarified that after thermal annealing; the ZnO thin film prepared in this experiment had a band gap of approximately 3.3 eV. Consider

$$\alpha h\nu = A(h\nu - E_g)^n. \quad (1)$$

In addition, with an increase in the thermal annealing temperature, the PL intensity showed an increasing trend. However, when the temperature reached 600°C, a 523 nm visible light (green) emission peak appeared simultaneously. Because ZnO materials can concurrently possess visible and invisible light (UV) emission properties, after discounting the self-emitting UV, the visible light emission is considered to result from an internal thin film defect, which is caused by electrons colliding with the luminescent center under high voltages. Vanheusden et al. [15–17] asserted that the green light's luminescent center, which is situated between 510 nm and 525 nm, is related to an O<sub>2</sub> vacancy (V<sub>O</sub>). According to their experimental results, high-temperature annealing consumes large quantities of O<sub>2</sub> in the air, increasing V<sub>O</sub> in the thin film and subsequently caused the intensity of the green light emission to increase. The experimental results in this study exhibit the same emission trend. Thus, it is inferred that the reduction of UV emission intensity and the appearance of a green light emission peak in the ZnO thin film are related to high-temperature thermal annealing, which generated internal thin film defects.



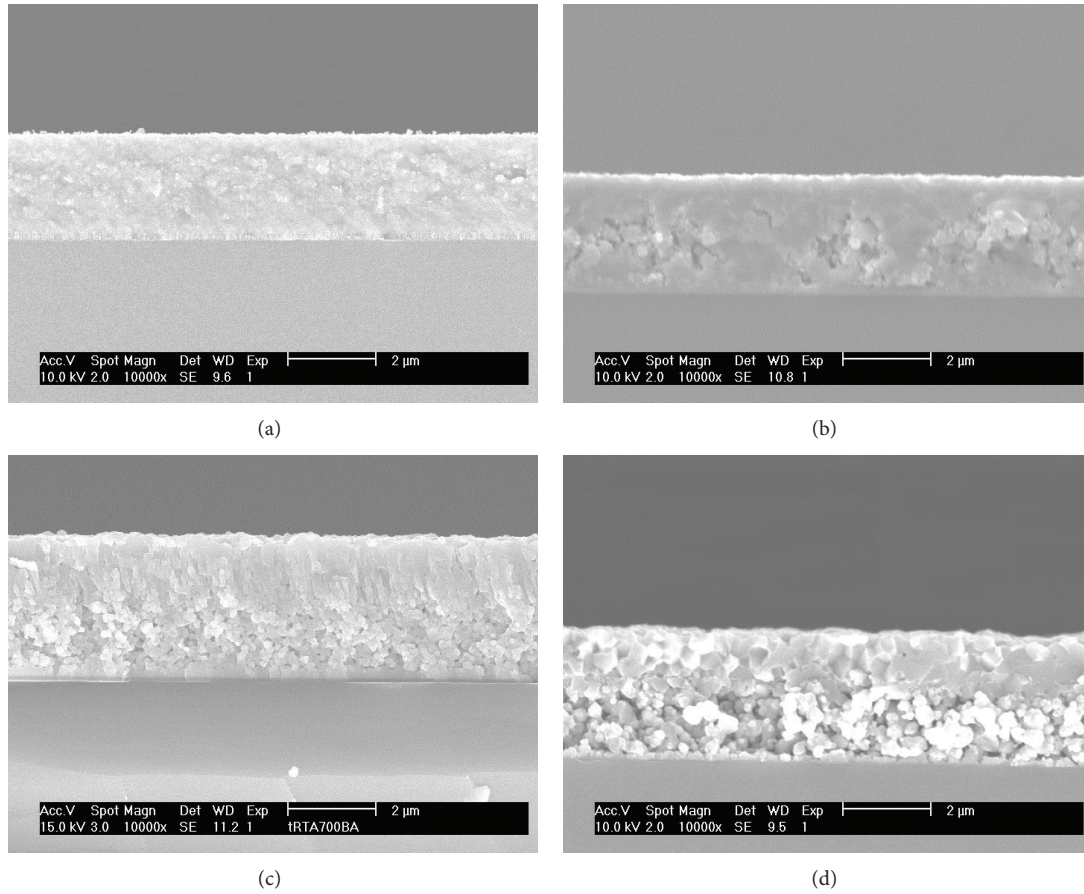


FIGURE 5: SEM cross section morphologies of ZnO thin film annealing under different temperatures: (a) 300°C, (b) 400°C, (c) 500°C, and (d) 600°C.

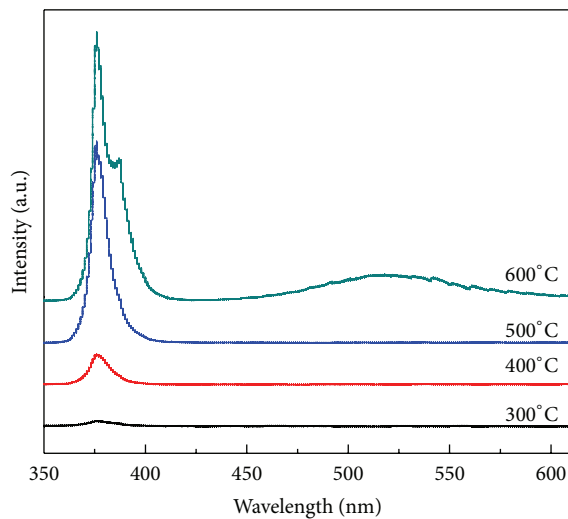


FIGURE 6: PL spectra of ZnO thin film annealing under different temperatures (dwelling time: 30 min).

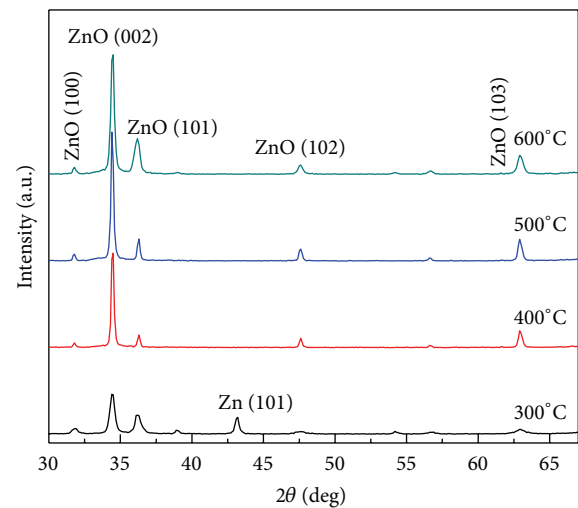


FIGURE 7: XRD diffraction peaks of ZnO thin film annealing under different temperatures.

Because the change in the UV emission intensity is related to the crystallization of the thin film during thermal annealing, this experiment conducted an XRD measurement

analysis to discover how they could be linked. The XRD diffraction analysis diagram for different thermal annealing temperatures (Figure 7) clearly shows that with an increase



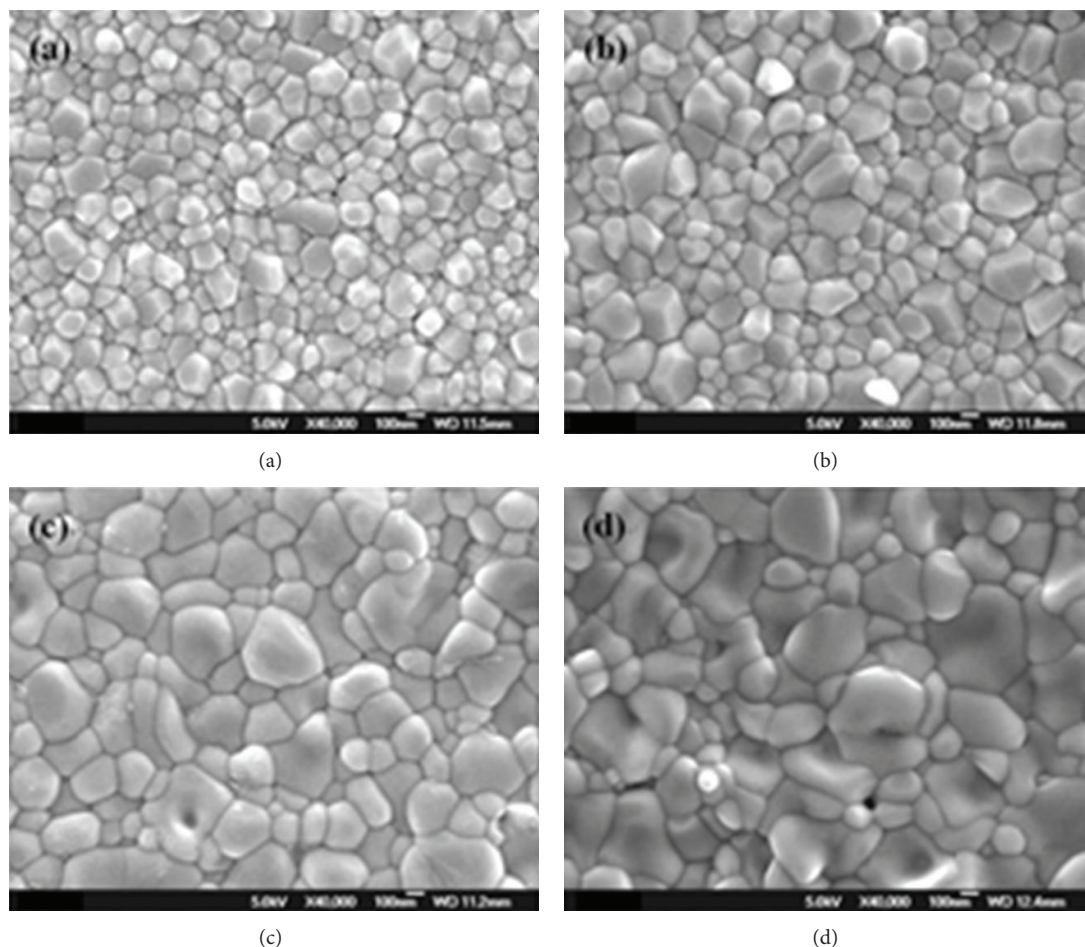


FIGURE 8: SEM surface morphologies of ZnO thin film annealing under different dwelling time: (a) 15 min, (b) 30 min, (c) 45 min, and (d) 60 min.

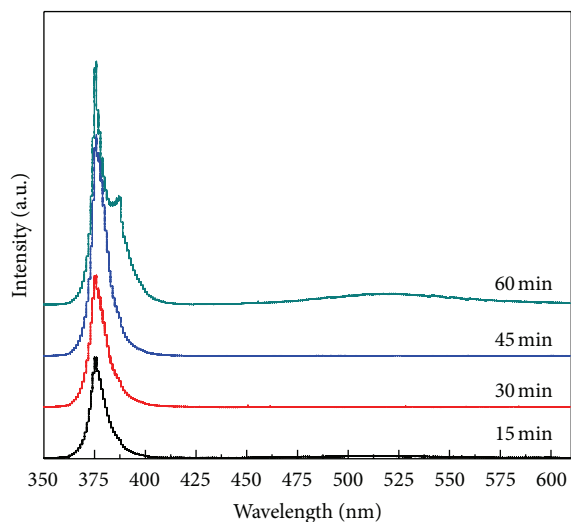


FIGURE 9: PL spectra of ZnO thin film annealing under different dwelling time (annealing temperature: 500°C).

in thermal annealing temperature, ZnO (002) exhibited an increasing degree of preferred *C*-axis orientation. This indicates that high-temperature thermal annealing can improve

crystallization in the ZnO thin film. However, after 300°C thermal annealing of the ZnO thin film, the image not only showed crystalline phase peak of ZnO (002) and ZnO (101) but also showed a diffraction peak of Zn (101). This is because the 300°C thermal annealing temperature had not reached the melting point of Zn; thus, the excess Zn in the thin film could not completely react. By increasing the thermal annealing temperature, the *C*-axis orientation of ZnO gradually increased. However, the peaks of other ZnO phases also progressively increased. When the temperature reached 600°C, the *C*-axis orientation began to reduce. Conversely, the increases in the ZnO (101), (102), and (103) peaks became more significant. This is because the ZnO thin film prepared in this experiment contained more Zn, and the Zn recombined with the O<sub>2</sub> in the air during thermal annealing, forming ZnO. The ZnO crystals with poor crystallization then formed in various directions, thus exhibiting a ZnO thin film structure with polycrystal patterns.

Figure 8 shows the SEM surface images of the thin film at a fixed thermal annealing temperature of 500°C, under atmospheric conditions, and for 15 min, 30 min, 45 min, and 60 min. The figure shows that the length of dwelling time affected the crystal growth. A longer dwelling time provides more reaction time and thermal energy that is required for

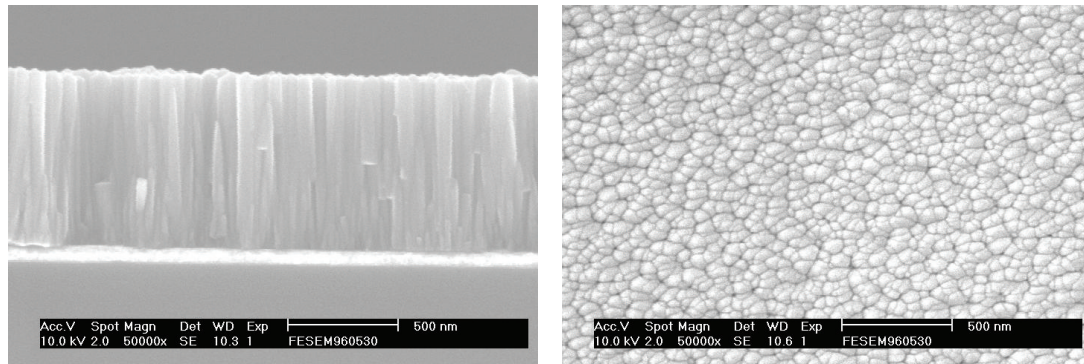


FIGURE 10: SEM surface and cross section topographical images of the ZnO thin film deposited on low- $O_2$  and low-pressure sputtering environment.

crystal growth and recrystallization. Therefore, the crystal size increases with an increase in the dwelling time. After maintaining the temperature for 45 min, the resulting crystal morphology appeared similar to that for 60 min. The primary reason is that the excess Zn in the thin film has almost completely reacted with the  $O_2$  in the air and formed ZnO; consequently, the Zn source for recrystallization was reduced, leading to decelerated crystal growth.

Figure 9 is the PL spectrogram for different dwelling times. In the figure, the UV emission intensity increased as the dwelling time was extended. The size of the crystals and the intensity of the UV emission were positively correlated. However, when the dwelling time reached 60 min, the PL image also began to show the emission peak of visible light (green). This indicates that thermal annealing not only allowed the crystals to grow and improved the thin film's internal crystallization but also highlighted the existing defects in the thin film with an increase in the dwelling time. Consequently, the PL image produced a visible light emission peak.

Figure 10 is the SEM surface and cross section topographical images of the ZnO thin film by 60%  $O_2$  concentration and  $20 \times 10^{-3}$  torr sputtering pressure, under atmospheric conditions. The image clearly shows that the surface of the ZnO thin film is flat; the thin film's internal structure is dense, because sufficient  $O_2$  concentration in the environment induced the thin film deposition rate to retard and exhibit a well hexagonal wurtzite structure.

Figure 11 is the XRD diffraction analysis diagram of ZnO thin film. It can be observed from Figure 11, it exhibited only the ZnO (002) peak. This is because the high- $O_2$ , high-pressure sputtering environment caused the zinc ion completely oxidized, to be increased the thin film's internal crystallization. Figure 12 is the PL spectrogram of ZnO thin film. The results showed only a weak 376 nm UV emission peak without the other visible light peak.

ZnO thin films with thermal annealing at 500°C (for 45 min) and atmospheric conditions exhibited a sharp (002) peak and small value of FWHM (full width at half maximum), as shown in Figure 13. Figure 14 presents the PL spectrogram for ZnO thin films with thermal annealing processes. The results shows a more obvious 376 nm UV emission peak

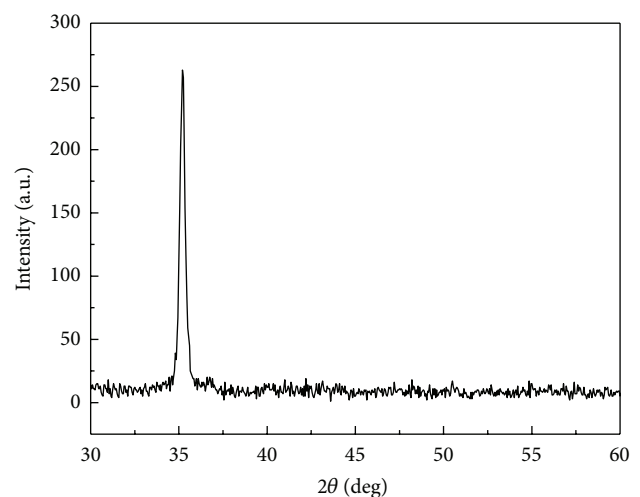


FIGURE 11: XRD diffraction analysis of the ZnO thin film deposited on low- $O_2$  and low-pressure sputtering environment.

because the thermal annealing processes increase the internal grain size of ZnO thin films.

#### 4. Conclusion

This study employed RF sputtering at room temperature to deposit a ZnO thin film on an ITO glass substrate. By varying the thermal annealing temperatures and dwelling times, this study explored changes in the thin film's internal structure and UV emission properties. The results showed that a low- $O_2$ , low-pressure sputtering environment readily forms a ZnO thin film with high Zn content. The excess Zn exhibited influences of differing levels on crystal growth and emission properties when different thermal annealing parameters were applied. The experiment showed that an increase in thermal annealing temperature or dwelling time resulted in gradual growth of crystal size, and when specific parameters were applied, the UV emission intensity increased with the crystal growth. However, when the thermal annealing temperature was at 600°C or when the dwelling time reached 60 min,

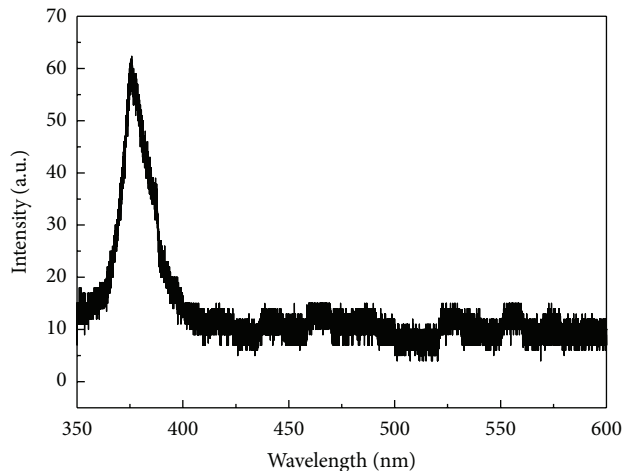


FIGURE 12: PL spectra of ZnO thin film deposited on low-O<sub>2</sub> and low-pressure sputtering environment.

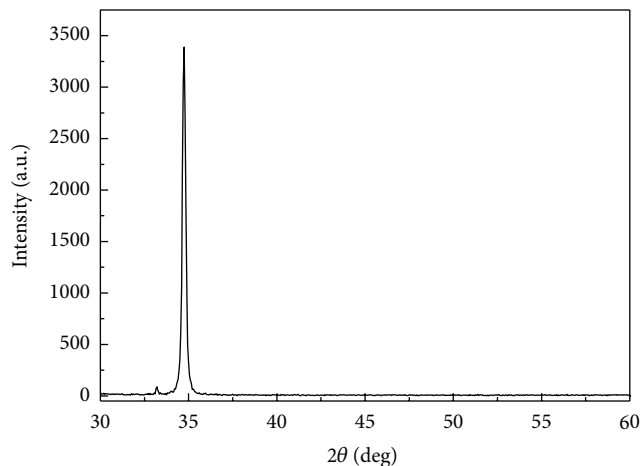


FIGURE 13: XRD diffraction analysis of the ZnO thin film deposited on low-O<sub>2</sub> and low-pressure sputtering environment with thermal annealing process.

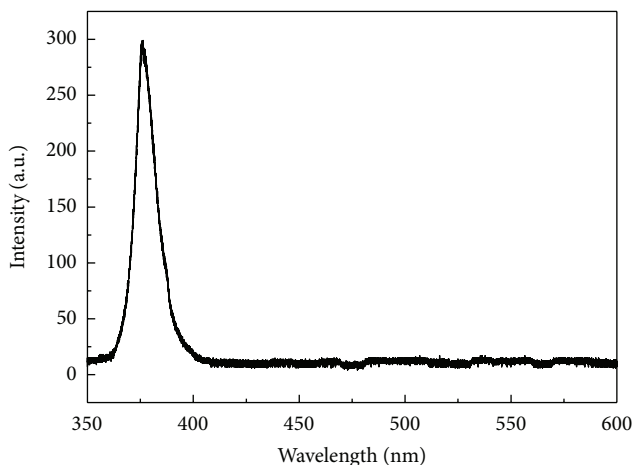


FIGURE 14: PL spectra of ZnO thin film deposited on low-O<sub>2</sub> and low-pressure sputtering environment with thermal annealing process.

actually exhibited a weak green light emission peak. This indicates that the thermal annealing process increased the thin film's internal crystallization and simultaneously enhanced the defects in the thin film and the growth of other crystalline phases. This is evidenced by the PL spectrogram and XRD diffraction analysis results. Consequently, ZnO luminescence is a type of defective emission caused by the V<sub>O</sub> in the thin film. Thus, the width of ZnO band gap determines the wavelength position of the UV emission center, and the grain size dominates the intensity of UV emission. In order to obtain the well UV emission, the Zn:O<sub>2</sub> ratio must be controlled with thermal annealing processes to improve the crystallization and grain size.

## References

- [1] U. Alver, T. Kiliç, E. Bacaksiz, and S. Nezir, "Temperature dependence of ZnO rods produced by ultrasonic spray pyrolysis method," *Materials Chemistry and Physics*, vol. 106, no. 2-3, pp. 227-230, 2007.
- [2] J. Ye, S. Gu, S. Zhu et al., "The growth and annealing of single crystalline ZnO films by low-pressure MOCVD," *Journal of Crystal Growth*, vol. 243, no. 1, pp. 151-156, 2002.
- [3] Z. Fu, B. Lin, and J. Zu, "Photoluminescence and structure of ZnO films deposited on Si substrates by metal-organic chemical vapor deposition," *Thin Solid Films*, vol. 402, no. 1-2, pp. 302-306, 2002.
- [4] Q. P. Wang, D. H. Zhang, Z. Y. Xue, and X. J. Zhang, "Mechanisms of green emission from ZnO films prepared by rf magnetron sputtering," *Optical Materials*, vol. 26, no. 1, pp. 23-26, 2004.
- [5] W. Lin, R. Ma, W. Shao, B. Kang, and Z. Wu, "Properties of doped ZnO transparent conductive thin films deposited by RF magnetron sputtering using a series of high quality ceramic targets," *Rare Metals*, vol. 27, no. 1, pp. 32-35, 2008.
- [6] D. Kim, T. Shimomura, S. Wakaiki, T. Terashita, and M. Nakayama, "Photoluminescence properties of high-quality ZnO thin films prepared by an RF-magnetron sputtering method," *Physica B*, vol. 376-377, no. 1, pp. 741-744, 2006.
- [7] S. H. Bae, S. Y. Lee, H. Y. Kim, and S. Im, "Effects of post-annealing treatment on the light emission properties of ZnO thin films on Si," *Optical Materials*, vol. 17, no. 1-2, pp. 327-330, 2001.
- [8] P. T. Hsieh, Y. C. Chen, K. S. Kao, M. S. Lee, and C. C. Cheng, "The ultraviolet emission mechanism of ZnO thin film fabricated by sol-gel technology," *Journal of the European Ceramic Society*, vol. 27, no. 13-15, pp. 3815-3818, 2007.
- [9] S. Hwangbo, Y.-J. Lee, and K.-S. Hwang, "Photoluminescence of ZnO layer on commercial glass substrate prepared by sol-gel process," *Journal of Crystal Growth*, vol. 290, pp. 341-344, 2006.
- [10] P. Sagar, P. K. Shishodia, R. M. Mehra, H. Okada, A. Wakahara, and A. Yoshida, "Photoluminescence and absorption in sol-gel-derived ZnO films," *Journal of Luminescence*, vol. 126, no. 2, pp. 800-806, 2007.
- [11] S. J. Pearton, D. P. Norton, K. Ip, Y. W. Heo, and T. Steiner, "Recent advances in processing of ZnO," *Journal of Vacuum Science and Technology B*, vol. 22, no. 3, pp. 932-948, 2004.
- [12] F. Bertram, D. Forster, J. Christen, N. Oleynik, A. Dadgar, and A. Krost, "Microscopic spatial distribution of bound excitons in high-quality ZnO," *Journal of Crystal Growth*, vol. 272, no. 1-4, pp. 785-788, 2004.

- [13] V. Srikant and D. R. Clarke, "On the optical band gap of zinc oxide," *Journal of Applied Physics*, vol. 83, no. 10, pp. 5447–5451, 1998.
- [14] K. H. Yoon, J.-W. Choi, and D.-H. Lee, "Characteristics of ZnO thin films deposited onto Al/Si substrates by r.f. magnetron sputtering," *Thin Solid Films*, vol. 302, no. 1-2, pp. 116–121, 1997.
- [15] K. Vanheusden, W. L. Warren, C. H. Seager, D. R. Tallant, J. A. Voigt, and B. E. Gnade, "Mechanisms behind green photoluminescence in ZnO phosphor powders," *Journal of Applied Physics*, vol. 79, no. 10, pp. 7983–7990, 1996.
- [16] H. S. Kang, J. S. Kang, S. S. Pang, E. S. Shim, and S. Y. Lee, "Variation of light emitting properties of ZnO thin films depending on post-annealing temperature," *Materials Science and Engineering B*, vol. 102, no. 1–3, pp. 313–316, 2003.
- [17] B. Lin, Z. Fu, Y. Jia, and G. Liao, "Defect photoluminescence of undoping ZnO films and its dependence on annealing conditions," *Journal of the Electrochemical Society*, vol. 148, no. 3, pp. G110–G113, 2001.



## Research Article

# Symmetric Negative Differential Resistance in a Molecular Nanosilver Chain

Tae Kyung Kim,<sup>1</sup> Hoi Ri Moon,<sup>1</sup> and Byung Hoon Kim<sup>2</sup>

<sup>1</sup> Interdisciplinary School of Green Energy, Ulsan National Institute of Science and Technology (UNIST), Ulsan 689-798, Republic of Korea

<sup>2</sup> Department of Physics, Incheon National University, Incheon 406-772, Republic of Korea

Correspondence should be addressed to Byung Hoon Kim; [khh37@incheon.ac.kr](mailto:khh37@incheon.ac.kr)

Received 22 October 2013; Accepted 30 October 2013

Academic Editor: Mun Seok Jeong

Copyright © 2013 Tae Kyung Kim et al. This is an open access article distributed under the Creative Commons Attribution License, which permits unrestricted use, distribution, and reproduction in any medium, provided the original work is properly cited.

The electrical transport properties of the molecular nanosilver chain have been investigated. We observed the symmetric negative differential resistance (NDR) in the current-voltage characteristics. The peak voltage ( $V_p$ ) increased but the peak current ( $I_p$ ) decreased upon cooling. The self-capacitance effect of the silver chain crystal is suggested to explain this unconventional NDR phenomenon.

## 1. Introduction

Negative differential resistance (NDR) has attracted much interest due to its applications for switch, memory, and high-speed logic devices. NDR explained by a resonance tunneling diode has been shown in various materials, such as germanium p-n junction [1], various heterostructures [2–6], semiconductor superlattices [7], self-assembled layered nanostructures [8], carbon atomic wires [9], mesoscopic manganite structures [10], and molecular electronics device systems [11–13]. The NDR has also been observed in graphene nanoribbon with unsaturated edges due to the strong current polarization [14] and due to the interaction between the narrow density of state of doped sites and the discrete states in the scattering region [15]. In addition, Ag-based materials, such as Ag/Si nanowires on silicon carbide, exhibited NDR as well [16]. NDR phenomena in general, including those mentioned above, exhibited asymmetric current-voltage ( $I$ - $V$ ) characteristics with respect to the applied voltage.

Recently, Moon et al. reported a stair-shaped  $\text{Ag}^0$  coordination compound without bridging ligands (nanosilver chain) [17]. This nanosilver chain (NSC) consists of Ag atoms linked by covalent bonds and pyridine molecules. Herein, we report the abnormal  $N$ -shaped NDR phenomenon of the single crystalline NSC and temperature-dependent NDR behavior that cannot be interpreted by previously reported

mechanisms. The  $I$ - $V$  characteristics in the backward voltage sweep were symmetric to that in the forward voltage sweep. Hysteretic behavior was manifested as well. The peak voltage ( $V_p$ ) increased and the peak current ( $I_p$ ) decreased as the temperature decreased. We suggest that the NDR phenomenon of the NSC may be caused by a capacitance effect of the NSC itself.

## 2. Materials and Methods

The  $I$ - $V$  characteristics were measured with the conventional 2-probe method. Silver paint (DuPont 4929N) and carbon paint (Dotite XC-12) contacts were made to 0.01 inch diameter gold wires. The  $I$ - $V$  characteristics were doubly checked using semiconductor characterization systems (Keithley 4200-SCS) and electrometer (Keithley 6517A). The voltage sweep rate was 10 mV/sec. The temperature-dependent  $I$ - $V$  characteristics were investigated with a cryogenic dilplex-osp.

## 3. Results and Discussion

The (001) and (010) planes of the single crystalline NSC are shown in Figure 1(a). The  $I$ - $V$  characteristics of the NSC crystal at room temperature measured in air right after mounting



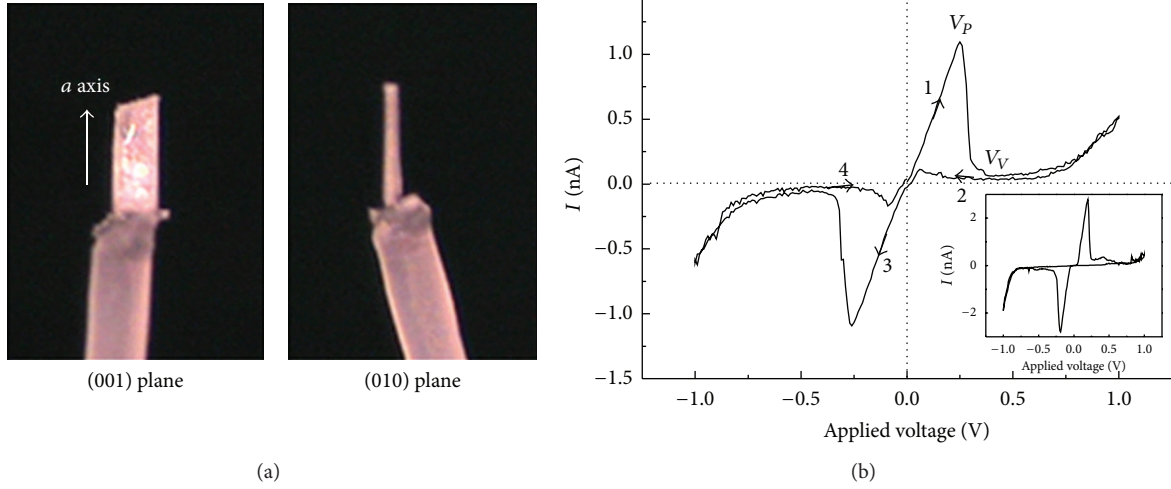


FIGURE 1: NDR behavior at room temperature. (a) An NSC single crystal is shown in the white box. (b)  $I$ - $V$  curve is measured in air at 300 K by the conventional 2-probe method with DuPont, silver composition 4929N paint.  $I_P$  is a peak current.  $V_P$  and  $V_V$  are voltages corresponding to the peak and the valley of the current, respectively. The number shows the voltage sweep procedure. The  $I$ - $V$  curve with a carbon paint contact is shown in the inset.

the sample were the same as those measured in a vacuum after loading the sample in the displax cryogenic system. This implies that the NSC crystal lost pyridine molecules as soon as it was exposed to air [17] for the measurements.  $N$ -type NDR was observed for  $V > V_P$  (0.25 V) as shown in Figure 1(b). Here,  $V_P$  and  $V_V$  are voltages corresponding to the peak and the valley of the current, respectively. The  $I$ - $V$  curve was linear in the low voltage region ( $0 < V < V_P$ ). The current abruptly dropped at  $V_P$  revealing NDR and started to increase gradually for  $V > V_V$  (process “1”). In the backward sweep from high to low voltage, the current followed the same curve as that in the forward sweep for  $V > V_V$ . However, it exhibited a big hysteresis for  $0 < V < V_V$  with a significantly reduced NDR peak (process “2”). The  $I$ - $V$  characteristics of the negative voltage region (processes “3” and “4”) were symmetrical with those of the positive voltage region. To check the contact effect, the identical experiment with a carbon paint contact was also done. The  $I$ - $V$  characteristics with carbon paint were the same with a silver paint contact although the details were not identical (the inset of Figure 1). This symmetric NDR with respect to the applied voltage has never been reported. It will be discussed later.

The temperature-dependent  $I$ - $V$  characteristics of the NSC crystal from 230 K to 300 K are shown in Figure 2. All  $I$ - $V$  curves showed the symmetric NDR behavior and the data were reproducible for 3–5 cycles of  $I$ - $V$  measurements at each temperature. The peak current ( $I_P$ ) decreased but  $V_P$  increased upon cooling. This is another unusual behavior in NDR phenomena. The resistivity ( $\rho$ ) at each temperature was obtained from the slope of the  $I$ - $V$  curve in the linear region ( $V < V_P$ ) (Figure 3(a)). The resistivity at 300 K is  $\rho_{300\text{ K}} \approx 1.5 \times 10^5 \Omega \text{ cm}$ , which is in the range of resistivity for ionic solids. The various Ag-based materials follow ionic conduction [18–21]. Although no mobile ions are reportedly expected to exist in the NSC crystal [17], it is possible for

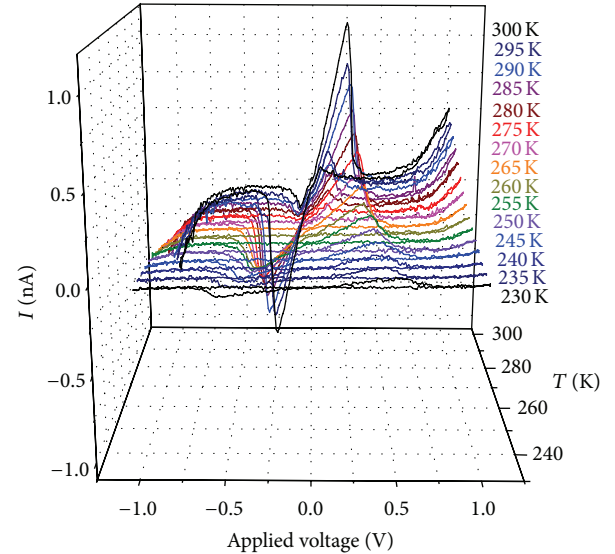


FIGURE 2: Temperature-dependent NDR behavior. All  $I$ - $V$  curves measured at various temperatures exhibit the symmetric NDR behavior.  $V_P$  increases but  $I_P$  decreases as the temperature decreases.

ionic defects to exist in the NSC crystal, and the defects can cause the current to flow through the sample by ionic conduction. The temperature-dependent conductivity of the NSC crystal seems to follow the ionic conduction behavior with the activation energy 0.35 eV. However, the resistivity is well fitted to the thermally activated hopping conduction,  $\rho = \rho_0 \exp(E_a/K_B T)$ , rather than the ionic conduction as shown in the inset of Figure 3(a).  $E_a$  and  $K_B$  are the activation energy and the Boltzmann constant, respectively. Moreover, the ionic conduction mechanism does not explain the unusual temperature dependence of the symmetric NDR

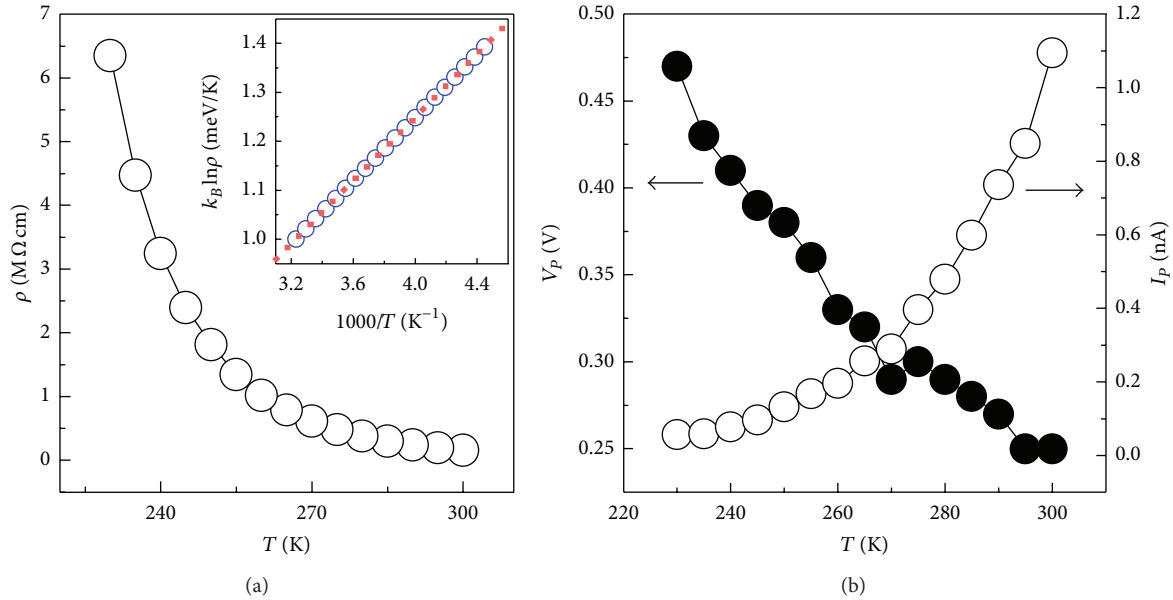


FIGURE 3: Abnormal NDR behavior. (a) Temperature-dependent resistivity follows the thermally activated hopping conduction (inset). (b) Contrary to NDR behavior reported previously,  $V_p$  increases but  $I_p$  decreases as the temperature decreases.

phenomena of the NSC crystal. Therefore, we suggest another possible mechanism for the NDR behavior.

Above all, we focused on the temperature-dependent NDR phenomena. Upon cooling, the values  $I_p$  decreased but  $V_p$  increased (Figure 3(b)). The temperature dependence of  $I_p$  and  $V_p$  was different from that of other NDR phenomena observed in the tunneling diode, Gunn effect [22], or subband transition from the high mobility of a fundamental level to the low mobility of a higher subband level, where  $I_p$  increased and  $V_p$  decreased upon cooling [9]. In case of a molecule containing a nitroamine redox center, both the  $I_p$  and  $V_p$  increased upon cooling [11]. The  $I_p$  decrement of the NSC crystal upon cooling is attributed to the thermally activated hopping conduction as described in Figure 3(a). However, the  $V_p$  increment on cooling is difficult to understand. We suggest a possible mechanism based on thermally modulated capacitance effect of the NSC itself.

At the beginning of voltage sweeping, the current increases due to the bias voltage and then charges are accumulated in the NSC gradually like a capacitor. At  $V_p$ , the charges are saturated in the NSC resulting in a drastic drop of the current at  $V_V$ . For  $V > V_V$ , the current exponentially increases with the increase of the bias voltage. This is called a thermal current [22]. During backward sweeping from  $V_V$  to 0 V, the current decreases exponentially, which follows the trace of a thermal current. In this process, hysteresis and discharging occur. As a negative bias voltage is applied, the same behavior is exhibited with an opposite polarity of charge. This results in symmetric NDR behavior with respect to the bias voltage.

In order to confirm that the charge storage is the dominant factor for the NDR of the NSC, we applied a different voltage ( $V_I$ ) at the beginning of sweeping (Figure 4(a)). When

$V_I$  started from the negative voltage (black line, from  $-1.0$  V to  $+1.0$  V), the peak in the negative voltage region did not appear. On the other hand, when the  $V_I$  was positive (red line, from  $+1.0$  V to  $-1.0$  V), the peak in the positive voltage region was not exhibited. Nonzero  $V_I$  over  $V_p$  means that a large number of charges are already stored in the NSC. Therefore, NDR was not observed. This is similar to the previous literature on ZnO nanowires [23]. In case of a consecutive sweep from  $-1.0$  V to  $+1.0$  V and to  $-1.0$  V, we found two peaks as expected (Figure 4(b)).

The decrease of  $V_p$  with the temperature can be understood by the thermally activated mobility,  $\mu = \mu_0 \exp(-\Delta/k_B T)$  [24]; here,  $\mu_0$  and  $\Delta$  are the prefactor and activation energy, respectively. This indicates that the mobility increases exponentially with the temperature and charges are more easily moved. At low temperature, an additional electrical potential, compared with high temperature, is necessary to fully store the charge in the sample. Hence, the  $V_p$  increases as the temperature decreases.

## 4. Conclusions

In summary, the temperature-dependent symmetric NDR phenomenon in the NSC crystal has been investigated. As the temperature decreases, the  $V_p$  increases but  $I_p$  decreases. We consider the thermally modulated capacitance effect of the NSC as the origin of the NDR behavior.

## Acknowledgment

This work was supported by the Incheon National University Research Grant in 20130418.

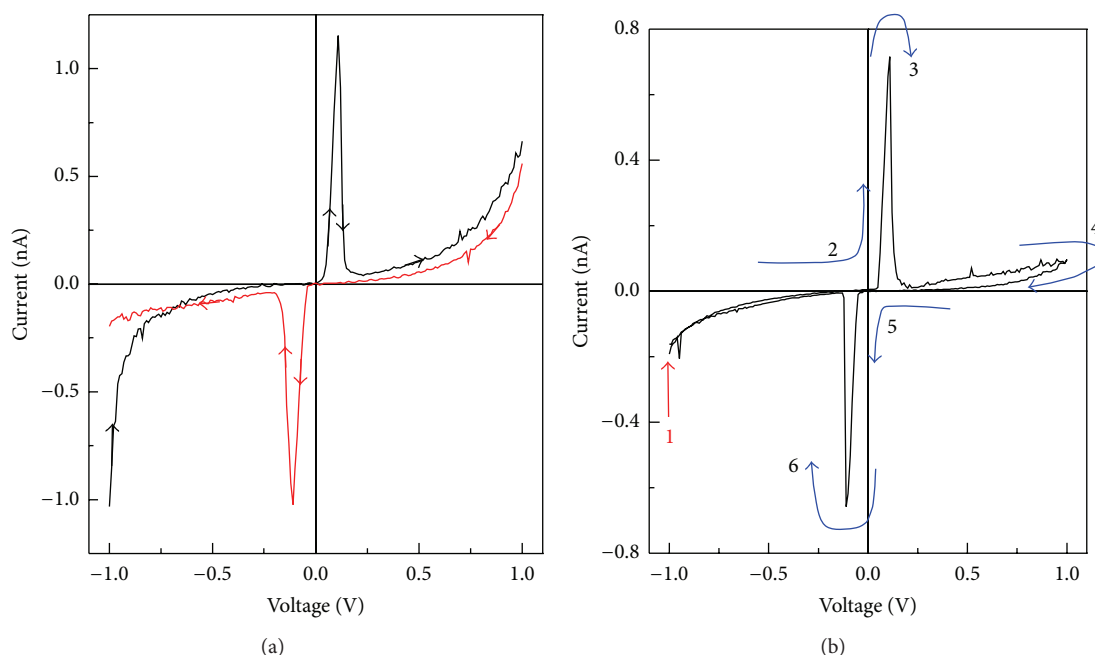


FIGURE 4: Capacitance effect of an NSC crystal. (a) A nonzero initial voltage results in the nonexistence of the peak in the voltage region, which is the same sign to the initial voltage. Black and red lines are the voltage sweep with negative and positive initial voltages, respectively. (b)  $I$ - $V$  characteristics were obtained by a consecutive bias voltage sweep. The number shows the sweep procedure.

## References

- [1] L. Esaki, "New phenomenon in narrow germanium p-n junctions," *Physical Review*, vol. 109, no. 2, pp. 603–604, 1958.
- [2] L. L. Chang, L. Esaki, and R. Tsu, "Resonant tunneling in semiconductor double barriers," *Applied Physics Letters*, vol. 24, no. 12, pp. 593–595, 1974.
- [3] M. A. Littlejohn, J. R. Hauser, and T. H. Glisson, "Monte Carlo calculation of the velocity-field relationship for gallium nitride," *Applied Physics Letters*, vol. 26, no. 11, pp. 625–627, 1975.
- [4] J. R. Söderström, D. H. Chow, and T. C. McGill, "New negative differential resistance device based on resonant interband tunneling," *Applied Physics Letters*, vol. 55, no. 11, pp. 1094–1096, 1989.
- [5] C. L. Wu, W. C. Hsu, M. S. Tsai, and H. M. Shieh, "Very strong negative differential resistance real-space transfer transistor using a multiple  $\delta$ -doping GaAs/InGaAs pseudomorphic heterostructure," *Applied Physics Letters*, vol. 66, no. 6, pp. 739–741, 1995.
- [6] T. Sugaya, K.-Y. Jang, C.-K. Hahn et al., "Enhanced peak-to-valley current ratio in InGaAs/InAlAs trench-type quantum-wire negative differential resistance field-effect transistors," *Journal of Applied Physics*, vol. 97, no. 3, Article ID 034507, 2005.
- [7] B. J. Keay, S. Zeuner, S. J. Allen Jr. et al., "Dynamic localization, absolute negative conductance, and stimulated, multiphoton emission in sequential resonant tunneling semiconductor superlattices," *Physical Review Letters*, vol. 75, no. 22, pp. 4102–4105, 1995.
- [8] J. A. Switzer, B. M. Maune, E. R. Raub, and E. W. Bohannan, "Negative differential resistance in electrochemically self-assembled layered nanostructures," *Journal of Physical Chemistry B*, vol. 103, no. 3, pp. 397–398, 1999.
- [9] B. Larade, J. Taylor, H. Mehrez, and H. Guo, "Conductance,  $I$ - $V$  curves, and negative differential resistance of carbon atomic wires," *Physical Review B*, vol. 64, no. 7, Article ID 075420, 10 pages, 2001.
- [10] T. Wu and J. F. Mitchell, "Negative differential resistance in mesoscopic manganite structures," *Applied Physics Letters*, vol. 86, no. 25, Article ID 252505, pp. 1–3, 2005.
- [11] J. Chen, M. A. Reed, A. M. Rawlett, and J. M. Tour, "Large on-off ratios and negative differential resistance in a molecular electronic device," *Science*, vol. 286, no. 5444, pp. 1550–1552, 1999.
- [12] M. Galperin, M. A. Ratner, and A. Nitzan, "Hysteresis, switching, and negative differential resistance in molecular junctions: a polaron model," *Nano Letters*, vol. 5, no. 1, pp. 125–130, 2005.
- [13] R. Liu, S.-H. Ke, H. U. Baranger, and W. Yang, "Negative differential resistance and hysteresis through an organometallic molecule from molecular-level crossing," *Journal of the American Chemical Society*, vol. 128, no. 19, pp. 6274–6275, 2006.
- [14] H. Ren, Q.-X. Li, Y. Luo, and J. Yang, "Graphene nanoribbon as a negative differential resistance device," *Applied Physics Letters*, vol. 94, no. 17, Article ID 173110, 3 pages, 2009.
- [15] X. F. Li, L. L. Wang, K. Q. Chen, and Y. Luo, "Strong current polarization and negative differential resistance in chiral graphene nanoribbons with reconstructed (2, 1)-edges," *Applied Physics Letters*, vol. 101, no. 7, Article ID 073101, 5 pages, 2012.
- [16] M. G. Silly, F. Charra, and P. Soukiasian, "Negative differential resistance at AgSi nanowires on silicon carbide: from a passive to an active massively parallel architecture," *Applied Physics Letters*, vol. 91, no. 22, Article ID 223111, 3 pages, 2007.
- [17] H. R. Moon, C. H. Choi, and M. P. Suh, "A stair-shaped molecular silver(0) chain," *Angewandte Chemie*, vol. 47, no. 44, pp. 8390–8393, 2008.

- [18] K. Hariharan, "Electrical ionic conductivity and electronic spectra of superionic  $\text{KAg}_4\text{I}_5$  films," *Journal of Physics D*, vol. 12, no. 11, pp. 1909–1916, 1979.
- [19] A. Avogadro, S. Manzini, and M. Villa, "Ionic conductivity and disorder modes in borate glass systems," *Physical Review Letters*, vol. 44, no. 4, pp. 256–258, 1980.
- [20] P. Vashishta, I. Ebbsjö, and K. Sköld, "Ionic motion in superionic  $\text{Ag}_2\text{S}$ ," *Journal of Physics C*, vol. 18, no. 11, pp. L291–L296, 1985.
- [21] M. A. Ureña, A. A. Piarristeguy, M. Fontana, and B. Arcondo, "Ionic conductivity ( $\text{Ag}^+$ ) in  $\text{AgGeSe}$  glasses," *Solid State Ionics*, vol. 176, no. 5-6, pp. 505–512, 2005.
- [22] S. M. Sze, *Physics of Semiconductor Devices*, chapter 11, John Wiley & Sons, New York, NY, USA, 2nd edition, 1981.
- [23] Y. Zhang and C.-T. Lee, "Negative differential resistance in  $\text{ZnO}$  nanowires bridging two metallic electrodes," *Nanoscale Research Letters*, vol. 5, no. 9, pp. 1492–1495, 2010.
- [24] P. W. M. Blom, M. J. M. de Jong, and M. G. van Munster, "Electric-field and temperature dependence of the hole mobility in poly(p-phenylene vinylene)," *Physical Review B*, vol. 55, no. 2, pp. R656–R659, 1997.



## Research Article

# Effect of Annealing on the ZnS Nanocrystals Prepared by Chemical Precipitation Method

**Nadana Shanmugam, Shanmugam Cholan, Natesan Kannadasan, Kannadasan Sathishkumar, and G. Viruthagiri**

*Department of Physics, Annamalai University, Annamalai Nagar, Chidambaram, Tamil Nadu 608 002, India*

Correspondence should be addressed to Nadana Shanmugam; [quantumgosh@rediffmail.com](mailto:quantumgosh@rediffmail.com)

Received 19 July 2013; Revised 12 October 2013; Accepted 21 October 2013

Academic Editor: Hong Seok Lee

Copyright © 2013 Nadana Shanmugam et al. This is an open access article distributed under the Creative Commons Attribution License, which permits unrestricted use, distribution, and reproduction in any medium, provided the original work is properly cited.

Nanocrystals of ZnS have been synthesized through simple chemical precipitation method using thiourea as sulphur source. The synthesized products were annealed at different temperatures in the range of 200–800°C. The as-synthesized and annealed samples were characterized by X-ray diffraction (XRD), UV-Visible absorption (UV-Vis), and room temperature photoluminescence (PL) measurements. The morphological features of ZnS annealed at 200 and 500°C were studied by atomic force microscope (AFM) and transmission electron microscope (TEM) techniques. The phase transformation of ZnS and formation of ZnO were confirmed by thermogravimetric (TG) and differential thermal analysis (DTA) curves.

## 1. Introduction

Wide bandgap semiconductor nanocrystals have attracted the scientific community in the past two decades because of their size dependent properties and diverse applications [1–3]. In semiconductor nanoparticles, bandgap energy can be tuned by slight variation in size and composition, which enables them to be used in variety of applications like photo catalysis, imaging, solar cells, and so forth with an increase in efficiency [4, 5]. A simultaneous control of structure and morphology of semiconductor nanocrystals provides opportunities to tune and explore their optical properties. Therefore, structure and morphology control are of great interest in the development of semiconductor nanocrystals. Zinc sulphide is a wide bandgap II-VI group semiconductor material of cubic and hexagonal morphologies with bandgaps of 3.72 eV [6] and 3.77 eV [7], respectively, at room temperatures. ZnS has wide range of applications owing to its fluorescence properties [8–13].

Annealing treatments are very common in semiconductor processing. The annealing can be used to improve the crystal quality and to confirm the stability of the crystal at a given temperature, which is important for device purposes. An annealing treatment is quite effective for reproducible

size control of ZnS nanocrystals [14]. In this work, we report the effect of annealing temperature on the structural and morphological properties of ZnS nanocrystals prepared by simple chemical precipitation method.

## 2. Experimental

**2.1. Preparation of ZnS Nanoparticle.** All the chemicals used in this study are of AR grade with 99% purity (Merck and SD fine chemicals) and used without further purification. Ultra-pure water was used for all dilution and sample preparation. Zinc acetate dihydrate  $[\text{Zn}(\text{CH}_3\text{COO})_2 \cdot 2\text{H}_2\text{O}]$  and thiourea  $[\text{CH}_4\text{N}_2\text{S}]$  were used as precursors.

The process to prepare ZnS nanoparticle is as follows. In this synthesis process, zinc and sulfur sources were taken in 1:1.5 molar ratios. For this 3 g of zinc acetate in 50 mL aqueous was stirred magnetically at 80°C until homogeneous solution was obtained. Then 3 g thiourea in 50 mL of aqueous was added drop by drop to the above solution. After stirring for 2 hours a colorless crystal cleared solution was formed. Then the solution was placed inside a hot air oven at a temperature of 130°C for 5 hours and then cooled down to room temperature. The resulting precipitates were filtered off

and washed several times in water and ethanol and the final products were dried in hot air oven at 80°C for 2 hours. The samples were then heat-treated at the rate of 10°C/min for 2 hours and held at temperatures in the range of 200, 400, 500, 600, and 800°C.

Nanocrystals of ZnS have been synthesized through simple chemical precipitation method using thiourea as sulphur source. The synthesized products were annealed at different temperatures in the range of 200–800°C mentioned above.

**2.2. Measurements.** The X-ray diffraction (XRD) patterns of the powdered samples were recorded using X' PERT PRO diffractometer with Cu-K $\alpha$  radiation ( $k = 1.5406 \text{ \AA}$ ). The crystallite size was estimated using the Scherrer equation. The optical absorption spectra of all the samples in deionized water were recorded using LAMDA 25 PERKIN ELMER spectrometer. Fluorescence measurements were performed on a VARIAN spectrophotometer. The morphology of the product was observed by Nano Surf Easy Scan 2 atomic force microscope (AFM). High-resolution transmission electron microscopy (HRTEM) analysis was performed using JEOL 3010 HRTEM to study the morphology and size of the nanocrystals. Thermogravimetric analysis (TGA) and differential thermal analysis (DTA) studies have been performed using Perkin Elmer Diamond TGA/DTA instrument at a heating rate of 20°C/min in air.

### 3. Results and Discussion

The XRD patterns of starting material as well as those of annealed samples are recorded in the scan range  $2\theta = 10\text{--}80^\circ$ . In the case of starting material, three diffraction peaks at  $2\theta$  values of  $28.5^\circ$ ,  $48^\circ$ , and  $57^\circ$  appeared due to reflection from the (111), (220), and (311) planes of the cubic (zinc blende) phase of ZnS (Figure 1). This result suggests that the crystal structure of the sample is in good accordance with that of the Zinc blende ZnS of the standard card (JCPDS card no-05-566). The particle size was determined to be 8.65 nm from the width of the diffraction peaks corresponding to (111), (220), and (311) planes by using the well-known Scherrer equation:

$$D = \frac{0.89\lambda}{\beta \cos \theta}, \quad (1)$$

where  $\lambda$  is wavelength of X-ray ( $1.5406 \text{ \AA}$ ),  $\beta$  is FWHM in radian, and  $\theta$  is Bragg's angle in degree.

From Figure 1 it is clear that, at 200°C, the sample is still in its cubic phase with broadened XRD peaks. The broadening of the diffraction peaks results from the decrease of particle size. The average particle size was determined to be 5.96 nm. As we increase the temperature to 400°C, phase transformation of ZnS has been taken place. As a result of transformation cubic phase of ZnS is changed into hexagonal ZnS. It is also seen in Figure 1 that at 400°C a faint portion of wurtzite ZnO has been formed and is indicated by the planes (100), (002), and (101).

The XRD patterns of all the four high temperature annealed samples match well with JCPDS numbers 36-1405 (for hexagonal ZnS) and 36-1451 (for hexagonal ZnO).

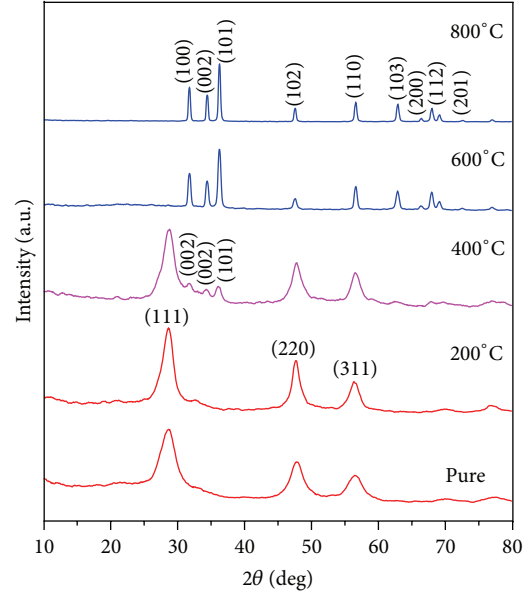


FIGURE 1: XRD patterns of as-synthesized and annealed ZnS.

However, ZnS wurtzite phase completely disappears and wurtzite ZnO appeared when the annealing temperature was brought to 500°C. This result reveals that 500°C is the temperature essential to the conversion from ZnS to ZnO nanoparticles in the presence of air [15]. The average particle size of the ZnO was determined from the diffractions peaks and found to be 22.82 nm.

Hence it is concluded that as a result of increase in annealing temperature formation of ZnO speeds up, and the transformation is completed at 500°C. On further increase in the annealing temperature up to 800°C, the diffraction peaks are found to narrow down as compared to those of the samples annealed at 500°C indicating the growth of bulk crystallites. The average crystallite sizes are 32.60 and 66.49 nm for the samples annealed at 600 and 800°C, respectively.

The optical properties of semiconductor materials are directly determined by the size and shape of the particles. We demonstrated the optical properties of as-synthesized and annealed products using a combination of UV-Visible and photoluminescence (PL) techniques. As shown in Figure 2, absorption peaks around 282, 278, 316, 333, 348, and 367 nm were noted corresponding to as-synthesized ZnS and ZnS annealed at 200, 400, 500, 600, and 800°C, respectively. In comparison with the absorption edge of as-synthesized ZnS, the absorption maximum of the sample annealed at 200°C was found to be blue-shifted by 4 nm. Such a shift in the optical absorption spectrum is known to take place owing to quantum confinement effect, which occurs in the case of nanoparticles when the particle size becomes comparable with or smaller than Bohr radius of exciton [16]. The ZnS nanoparticles annealed at 200°C have size less than the Bohr exciton diameter of ZnS, which is around 5.96 nm. According to the formula  $E_g = hc/\lambda \text{ eV}$ , the bandgaps were calculated and are 4.39, 4.46, 3.92, 3.72, 3.56, and 3.40 eV,

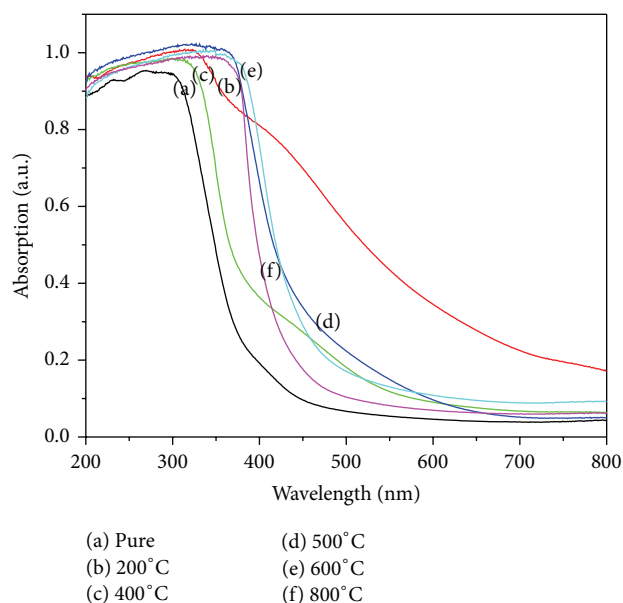


FIGURE 2: UV-Visible absorption spectra of as-synthesized and annealed ZnS nanocrystals.

respectively, for as-synthesized ZnS and ZnS annealed at different temperatures.

The bandgap of ZnS annealed at 200°C has been increased (4.46 eV) when compared with the bandgap of as-synthesized ZnS (4.39 eV) as a result of quantum confinement. This result suggests that 200°C is the optimum annealing temperature for the harvest of narrow sized ZnS nanocrystals. In addition, the bandgap value of the sample annealed at 500°C (3.72 eV) is higher than that of bulk value of ZnO (3.37 eV), which confirms the conversion of ZnS into ZnO as a result of oxidation of ZnS. However, beyond 200°C the bandgap of the samples decreases with increase in annealing temperature.

The room temperature PL spectra of the as-prepared and annealed ZnS nanoparticles are shown in Figure 3. The as-prepared ZnS exhibits three emission peaks positioned at ~349 nm, ~407 nm, and ~540 nm. The emission at ~349 nm is attributed to the near-band-edge emission of ZnS [17]. The peak observed at around ~407 nm can be attributed to the recombination of electrons at surface sulfur vacancy with the holes at the valance band. The emission at ~540 nm could be attributed to some self-activated defect centres related to Zn-vacancies [18]. In samples annealed at 200°C, the PL emission peaks are shifted to higher wavelength regions compared to as-synthesized samples. The shifts in PL peaks are attributed to the variation of bandgap as annealing temperature increases as mentioned in UV-Visible absorption studies. Particularly the peak positioned at 540 nm in as-synthesized ZnS was shifted (578 nm) with enhanced intensity. The red shift can be attributed to quantum size effect owing to small particle size and the enhanced intensity reveals that PL spectra are consistent with XRD result of ZnS annealed at 200°C.

The emission intensity at 578 nm may be due to the recombination of electrons from the energy level of sulfur

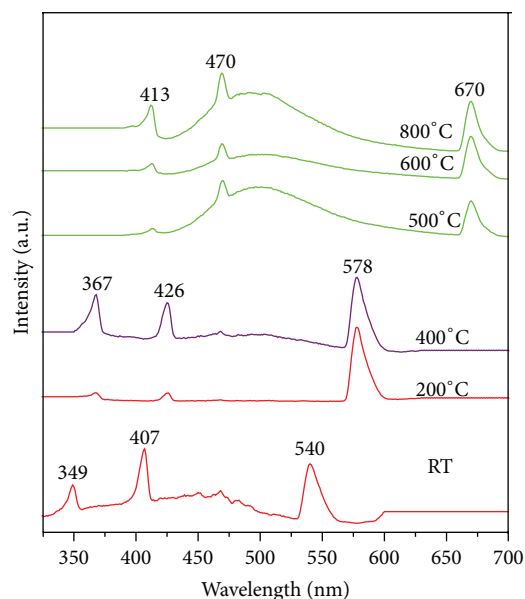


FIGURE 3: PL spectra of as-synthesized and annealed ZnS nanocrystals.

vacancies with the holes from the energy level of zinc vacancies. At an annealing temperature of 400°C, there is no change in the positions of the peaks but the intensity of them has been enhanced. Further, annealing at 500°C revealed three emission peaks at 413, 470, and 670 nm. The emission at 413 nm is attributed to near-band-edge emission of ZnO originating from excitonic transitions of between electrons in the conduction bands and the holes in the valence bands [19–21]. The emissions at 470 nm and 670 nm are probably ascribed to oxygen vacancies or other defects [22, 23]. The positions of the emission bands are unchanged as the annealing temperature is raised from 500 to 600°C and then to 800°C. This suggests that these emission bands are weakly associated with the bandgap properties. On the other hand, as far as the intensity is concerned, the intensity of the emission peaks has been enhanced with raise in annealing temperature which means that the oxygen vacancy concentration increases after annealing at high temperatures.

The surface morphology and particle size of the ZnS annealed at 200 and 500°C were studied by AFM. The two- and three-dimensional images of the ZnS annealed at 200°C are shown in Figures 4(a) and 4(b). From the two-dimensional view it is noted that most of the particles are well separated from each other and are spherical in shape. The sizes of the particles are in the range of 2.5–27.5 nm. However, most of the particles are in the range of 5–15 nm. The size obtained from the AFM matched well in accordance with the XRD and TEM results. The 3D view revealed that the growth direction of all the particles was the same.

Figure 4(c) shows the AFM image of ZnS nanoparticles after being annealed at 500°C. As can be seen in the figure, the spherical shape of the nanocrystals does not changes upon annealing, whereas the morphology at the nanoscale exhibits dramatic changes. As a result of high temperature

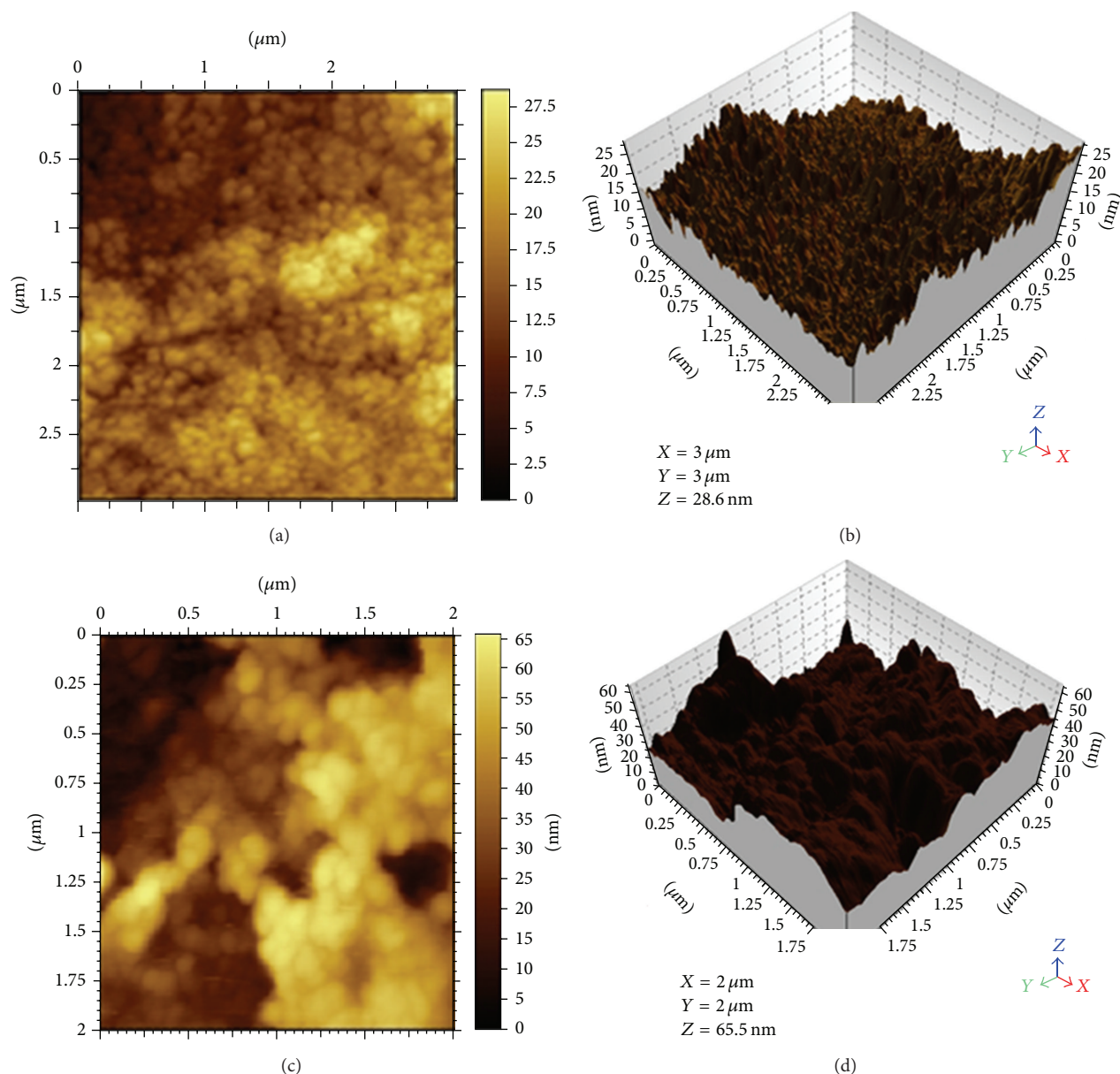


FIGURE 4: (a) AFM image of ZnS annealed at 200°C, (b) corresponding 3D view. (c) AFM image of ZnS annealed at 500°C, (d) corresponding 3D view.

annealing, the size of the particles has been increased due to agglomeration. The size is ranging between 10 and 65 nm. However, most of them are in the range of 30 nm. The 3D view (Figure 4(d)) exhibits the inhomogeneous growth pattern of the samples.

The morphology and sizes of the nanocrystals are confirmed from TEM studies, as shown in Figure 5. Figure 5(a) indicates the HRTEM image of the samples annealed at 200°C, revealing the formation of almost monodispersed nanocrystals with average diameter  $\sim 2$  nm. TEM measurements of ZnS (Figures 5(b) and 5(c)) annealed at 200°C show the agglomerated, nearly spherical particles with size variation between 10 and 15 nm. Figure 5(d) depicts the

selected-area electron diffraction (SAED) pattern of the sample annealed at 200°C. All the diffraction rings were indexed to those of spherical phase of ZnS in agreement with the XRD patterns. The clear lattice fringes display indicates that the nanoparticles are good crystals. The (111) lattice planes of some particles can mainly be observed and this lattice spacing is estimated to be about 0.310 nm from HRTEM image, which is consistent with the cubic ZnS (111) spacing value (0.312 nm) from standard JCPDS database.

The TEM measurements of ZnO (ZnS annealed at 500°C) are shown in Figure 6. Figure 6(a) specifies the HRTEM image of the ZnS annealed at 500°C, revealing the formation of ZnO nanocrystals with diameter  $\sim 2$  nm. In addition the



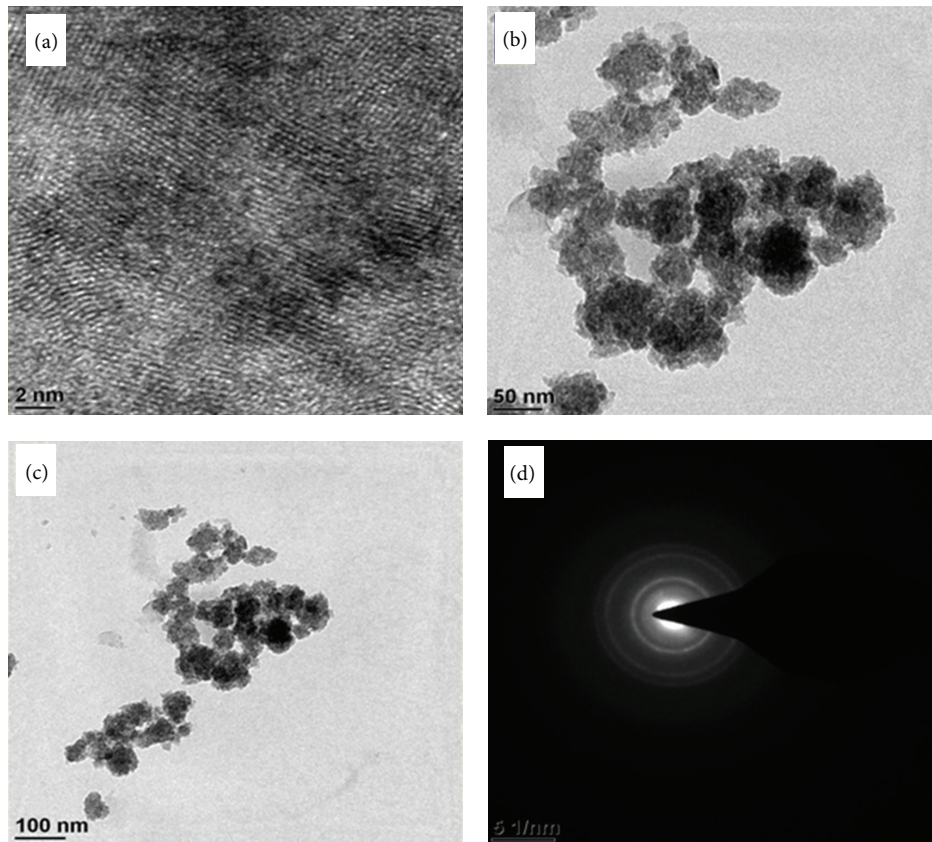


FIGURE 5: (a) HRTEM image of ZnS annealed at 200°C, (b), (c) corresponding TEM micrographs, and (d) corresponding SAED pattern.

HRTEM shows that the lattice fringes are separated by a diameter of 0.26 nm, representing the interplanar distance of the (101) lattice plane of ZnO hexagonal phase. TEM images of the ZnO show (Figures 6(b) and 6(c)) that the sizes of the individual particles are in the range of 25 to 80 nm. The SAED pattern shows the well-defined electron diffraction spots, confirming the single crystalline nature of the hexagonal phase of ZnO nanocrystals.

The deviation in the size of the nanoparticles measured by AFM and TEM from Debye-Scherrer calculation may be due to difference in the film preparation and detection technique. When preparing thin film for AFM or TEM techniques, the smaller nanoparticles may physically contact each other to form larger size particle [24]. It is a well-established fact that precision of crystallite size analysis by Debye-Scherrer calculations, as best, of the order of  $\pm 10\%$  [25, 26].

The thermal stability of the synthesized product was investigated by TG-DTA, as shown in Figure 7. The TGA showed four distinct weight losses arising from desorption of water (below 200°C), the decomposition of organic template (200–300°C), the phase transformation of ZnS (300–500°C), and the formation of ZnO due to oxidation of ZnS (500–800°C). After 800°C there was no weight loss until 1200°C.

From the DTA curve, there exists an endothermic peak at 180°C that may be due to removal of water molecules. A sharp endothermic peak at 220°C could be due to the removal of residual organics. As the temperature increases

to 340°C, a small endothermic peak appeared as a result of starting of phase transformation of ZnS. A wide exothermic peak between 300 and 700°C with a maximum at 500°C was noted. The maximum at 500°C explains the formation of ZnO as a result of oxidation of ZnS. During oxidation enormous amount of energy is released in the form of heat. The wideness of the exothermic peak was due to the growth of the particles and the energy was, therefore released [27]. As the temperature was over 800°C, the whole system tended to be endothermic. It could be assumed that sulfur atoms escape from the zinc sulfide lattice completely and therefore absorb energy.

#### 4. Conclusions

In the present work, the influence of thermal annealing on the structural, optical, and morphological features of ZnS nanocrystals was investigated. XRD patterns show the formation of 5.96 nm sized sphere-like cubic ZnS nanocrystals at 200°C. However, annealing at 500°C in air converts ZnS into ZnO as a result of oxidation. UV-Visible absorption peaks suggest that beyond 200°C the bandgap of the sample decreases with increase in annealing temperature. The room temperature PL measurements of as-synthesized and annealed samples exhibit that the intensity of the emission peaks has been enhanced with raise in annealing temperature which means that the oxygen vacancy concentration

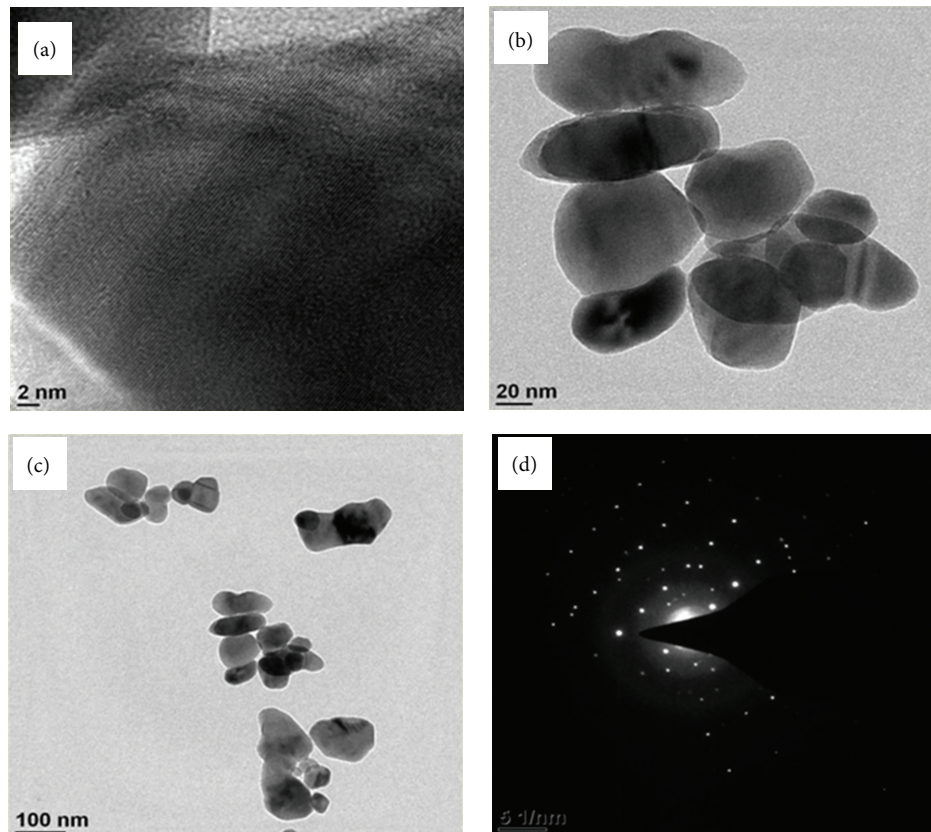


FIGURE 6: (a) HRTEM image of ZnO (ZnS annealed at 500°C), (b), (c) corresponding TEM micrographs, and (d) corresponding SAED pattern.

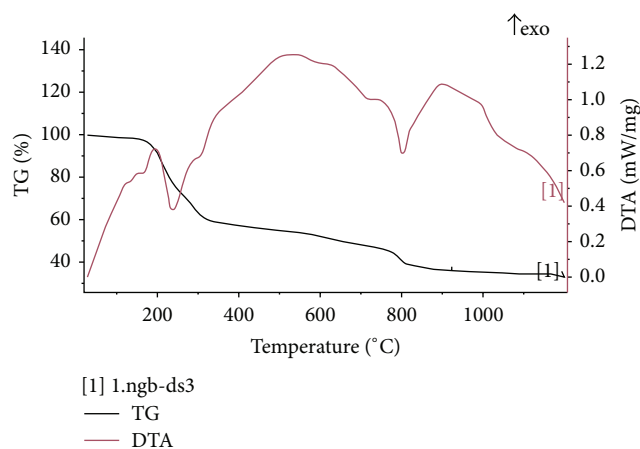


FIGURE 7: TG-DTA curves of as-synthesized ZnS nanocrystals.

increases after annealing at high temperatures. The surface morphology of ZnS and ZnO was studied by atomic force microscope. The AFM results reveal that particle agglomeration increases with increase of annealing temperature. The periodic layer nanometer structures of ZnS and ZnO

were identified by high resolution transmission electron microscopy (HR-TEM) images, with thickness of  $\sim 2$  nm. TEM measurements of ZnS annealed at 200°C show the agglomerated, nearly spherical particles with size variation between 10 and 15 nm, whereas micrographs of the ZnS annealed at 500°C show that the sizes of the individual particles are in the range of 25 to 80 nm. The phase transformation of ZnS and formation of ZnO were confirmed by TG-DTA curves.

## References

- [1] X. Fang, Y. Bando, U. K. Gautam et al., "ZnO and ZnS nanostructures: ultraviolet-light emitters, lasers, and sensors," *Critical Reviews in Solid State and Materials Sciences*, vol. 34, no. 3-4, pp. 190-223, 2009.
- [2] F. Monroy, F. Omnes, and F. Calle, "Wide-band gap semiconductor ultraviolet photo detectors," *Semiconductor Science and Technology*, vol. 18, pp. 33-51, 2003.
- [3] C. Feigl, S. P. Russo, and A. S. Barnard, "Safe, stable and effective nanotechnology: phase mapping of ZnS nanoparticles," *Journal of Materials Chemistry*, vol. 20, no. 24, pp. 4971-4980, 2010.
- [4] A. P. Alivisatos, "Semiconductor clusters, nanocrystals, and quantum dots," *Science*, vol. 271, no. 5251, pp. 933-937, 1996.

- [5] P.-C. Kuo, H.-W. Wang, and S.-Y. Chen, "Synthesis and photoluminescent properties of wurtzite ZnS nanorods by hydrothermal and co-precipitation methods," *Journal of the Ceramic Society of Japan*, vol. 114, no. 1335, pp. 918–922, 2006.
- [6] W. Park, T. C. Jones, W. Tong et al., "Luminescence decay kinetics in homogeneously and delta-doped ZnS:Mn," *Journal of Applied Physics*, vol. 84, no. 12, pp. 6852–6858, 1998.
- [7] H. C. Ong and R. P. H. Chang, "Optical constants of wurtzite ZnS thin films determined by spectroscopic ellipsometry," *Applied Physics Letters*, vol. 79, no. 22, pp. 3612–3614, 2001.
- [8] T. Yamamoto, S. Kishimoto, and S. Iida, "Control of valence states for ZnS by triple-codoping method," *Physica B*, vol. 308–310, pp. 916–919, 2001.
- [9] M. Bredol and J. Merikhi, "ZnS precipitation: morphology control," *Journal of Materials Science*, vol. 33, no. 2, pp. 471–476, 1998.
- [10] P. Calandra, M. Goffredi, and V. T. Liveri, "Study of the growth of ZnS nanoparticles in water/AOT/n-heptane microemulsions by UV-absorption spectroscopy," *Colloids and Surfaces A*, vol. 160, no. 1, pp. 9–13, 1999.
- [11] C. Falcony, M. Garcia, A. Ortiz, and J. C. Alonso, "Luminescent properties of ZnS:Mn films deposited by spray pyrolysis," *Journal of Applied Physics*, vol. 72, no. 4, pp. 1525–1527, 1992.
- [12] W. Tang and D. C. Cameron, "Electroluminescent zinc sulphide devices produced by sol-gel processing," *Thin Solid Films*, vol. 280, no. 1–2, pp. 221–226, 1996.
- [13] C. N. Xu, T. Watanabe, M. Akiyama, and X. G. Zheng, "Artificial skin to sense mechanical stress by visible light emission," *Applied Physics Letters*, vol. 74, no. 9, pp. 1236–1238, 1999.
- [14] T. Kuzuya, Y. Tai, S. Yamamuro, and K. Sumiyama, "Synthesis of copper and zinc sulfide nanocrystals via thermolysis of the polymetallic thiolate cage," *Science and Technology of Advanced Materials*, vol. 6, no. 1, pp. 84–90, 2005.
- [15] D. Amaranatha Reddy, G. Murali, B. Poornaprakash, R. P. Vijayalakshmi, and B. K. Reddy, "Effect of annealing temperature on optical and magnetic properties of Cr doped ZnS nanoparticles," *Solid State Communications*, vol. 152, no. 7, pp. 596–602, 2012.
- [16] S. Biswas and S. Kar, "Fabrication of ZnS nanoparticles and nanorods with cubic and hexagonal crystal structures: a simple solvothermal approach," *Nanotechnology*, vol. 19, no. 4, Article ID 045710, 2008.
- [17] Y. Li, L. You, R. Duan et al., "Straight ZnS nanobelts with wurtzite structure synthesized by the vapour phase transport process and their crystallization and photoluminescence properties," *Nanotechnology*, vol. 15, no. 5, pp. 581–585, 2004.
- [18] W. Que, Y. Zhou, Y. L. Lam et al., "Photoluminescence and electroluminescence from copper doped zinc sulphide nanocrystals/polymer composite," *Applied Physics Letters*, vol. 73, no. 19, pp. 2727–2729, 1998.
- [19] H.-P. Cong and S.-H. Yu, "Hybrid ZnO-dye hollow spheres with new optical properties from a self-assembly process based on evans blue dye and cetyltrimethylammonium bromide," *Advanced Functional Materials*, vol. 17, no. 11, pp. 1814–1820, 2007.
- [20] S. Yu, C. Wang, J. Yu, W. Shi, R. Deng, and H. Zhang, "Precursor induced synthesis of hierarchical nanostructured ZnO," *Nanotechnology*, vol. 17, no. 14, pp. 3607–3612, 2006.
- [21] R.-Q. Song, A.-W. Xu, B. Deng, Q. Li, and G.-Y. Chen, "From layered basic zinc acetate nanobelts to hierarchical zinc oxide nanostructures and porous zinc oxide nanobelts," *Advanced Functional Materials*, vol. 17, no. 2, pp. 296–306, 2007.
- [22] G. Shen, Y. Bando, and C.-J. Lee, "Growth of self-organized hierarchical ZnO nanoarchitectures by a simple In/In<sub>2</sub>S<sub>3</sub> controlled thermal evaporation process," *Journal of Physical Chemistry B*, vol. 109, no. 21, pp. 10779–10785, 2005.
- [23] Y. Zhang and J. Mu, "Controllable synthesis of flower- and rod-like ZnO nanostructures by simply tuning the ratio of sodium hydroxide to zinc acetate," *Nanotechnology*, vol. 18, no. 7, Article ID 075606, 2007.
- [24] N. Goswami and P. Sen, "Photoluminescent properties of ZnS nanoparticles prepared by electro-explosion of Zn wires," *Journal of Nanoparticle Research*, vol. 9, no. 3, pp. 513–517, 2007.
- [25] B. D. Cullity, *Elements of X-Ray Diffraction*, Addison-Wesley, Reading, Mass, USA, 1978.
- [26] L. V. Azaroff, *Elements of X-Ray Crystallography*, McGraw-Hill, New York, NY, USA, 1968.
- [27] R. K. Rana, L. Zhang, J. C. Yu, Y. Mastai, and A. Gedanken, "Mesoporous structures from supramolecular assembly of in situ generated ZnS nanoparticles," *Langmuir*, vol. 19, no. 14, pp. 5904–5911, 2003.



## Research Article

# Novel Method of Evaluating the Purity of Multiwall Carbon Nanotubes Using Raman Spectroscopy

Young Chul Choi,<sup>1</sup> Kyoung-In Min,<sup>2</sup> and Mun Seok Jeong<sup>3,4</sup>

<sup>1</sup> CNT Team, Hanwha Chemical, 80 Annamro 402 gil, Bupyeong-gu, Incheon 403-030, Republic of Korea

<sup>2</sup> Spectro, Gwangju 500-712, Republic of Korea

<sup>3</sup> Center for Integrated Nanostructure Physics, Institute for Basic Science, Sungkyunkwan University, Suwon 440-746, Republic of Korea

<sup>4</sup> Department of Energy Science, Sungkyunkwan University, Suwon 440-746, Republic of Korea

Correspondence should be addressed to Mun Seok Jeong; [mjeong@skku.edu](mailto:mjeong@skku.edu)

Received 15 October 2013; Accepted 29 October 2013

Academic Editor: Clare C. Byeon

Copyright © 2013 Young Chul Choi et al. This is an open access article distributed under the Creative Commons Attribution License, which permits unrestricted use, distribution, and reproduction in any medium, provided the original work is properly cited.

We propose the quantitative method of evaluating the purity of multiwall carbon nanotubes (MWCNTs) using Raman spectroscopy. High purity MWCNTs were prepared by chemical vapor deposition (CVD) to be used as a reference material with 100% purity. Since the intensity and wavenumber of  $D''$ -band located at around  $1500\text{ cm}^{-1}$  were found to be independent of the excitation wavelength of a laser, the purity of MWCNTs was measured by comparing the intensity ratio of  $D''$ -band to  $G$ -band ( $I_{D''}/I_G$ ) of the sample with that of a reference material. The established method was verified by testing the mixture of amorphous carbon particles and reference MWCNTs.

## 1. Introduction

Since multiwall carbon nanotubes (MWCNTs) possess high electrical conductivity, high thermal conductivity, and excellent mechanical properties [1–3], they have been extensively studied for being used in the electrical, thermal, and mechanical applications [4–7]. In order to achieve better characteristics of application products, the advancement in the synthesis technology has been tried to improve the properties of MWCNTs, including crystallinity, dispersibility, and purity [8–10]. Among these characteristics, purity is one of the most important properties from the viewpoint of better performance of application products. In addition, since higher purity means that a smaller amount of CNTs is required to achieve targeted properties, it is very important for industrial applications to use high purity MWCNTs in terms of low cost. Many researchers have used thermogravimetric analysis (TGA) [11–13] and  $D$ -band to  $G$ -band intensity ratio of Raman spectrum ( $I_D/I_G$ ) [14] to measure the purity of MWCNTs. However, TGA represents the whole carbon content in the sample because measuring the weight

loss with increasing temperature does not distinguish carbon nanotubes from other carbon species. Meanwhile, apart from the fact that the intensity and position of  $D$ -band peak are varied with the excitation wavelength of a laser to a great extent [15],  $D$ -band originates from not only amorphous carbon particles but also nanotube-related aspects including defects in the curved graphene sheets, tube ends, and finite size of crystalline domains of the tubes [16]. Thus, the measurement of ( $I_D/I_G$ ) is not useful for evaluating the purity of MWCNTs using various wavelengths of laser. In contrast to  $D$ -band, the intensity and position of  $D''$  band are not varied with the wavelength of laser. Moreover,  $D''$ -band originates from only amorphous carbons [17]. Therefore, we propose here the quantitative method evaluating the purity of MWCNTs using the  $D''$ -band Raman spectrum of MWCNTs as a signal for amorphous carbon particles.

As-synthesized MWCNTs are in general composed of the nanotubes, catalyst particles, and amorphous carbonaceous particles. Since the crystallinity of MWCNTs observed from Raman spectroscopy is clearly distinguishable from that of amorphous carbons, we used the comparison of Raman peaks



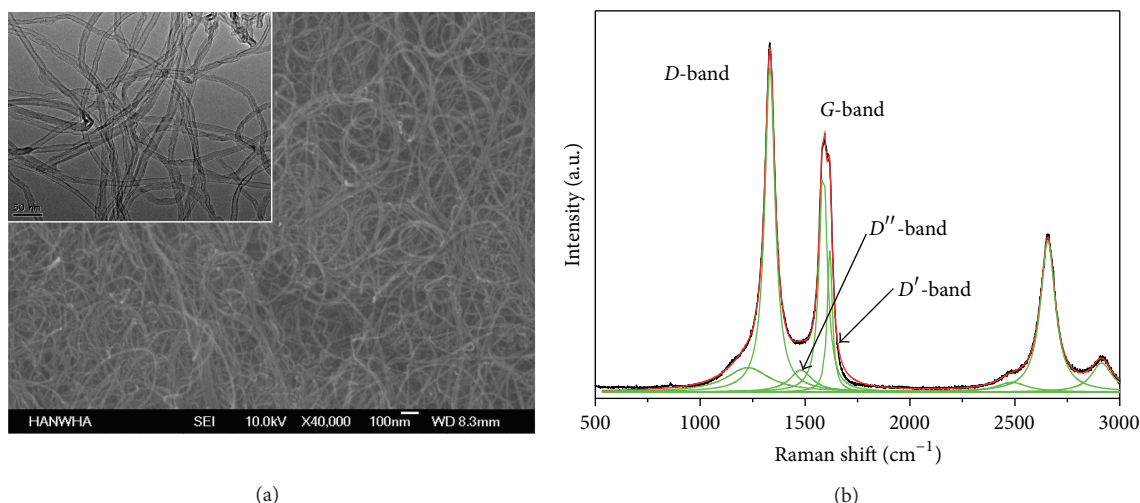


FIGURE 1: (a) SEM image of reference MWCNTs with 100% purity. Inset shows the HRTEM image of reference MWCNTs. (b) Raman spectrum of reference MWCNTs.

observed from MWCNTs and amorphous carbons for evaluating the purity of MWCNTs. A high purity MWCNT-sample was prepared and then used as a reference material. The purity was evaluated from comparing  $D''$ -band to G-band intensity ratio ( $I_{D''}/I_G$ ) of sample with  $I_{D''}/I_G$  of reference materials. MWCNTs have been synthesized by either arc-discharge [18, 19] or chemical vapor deposition (CVD) [1–10]. Since the MWCNTs synthesized by arc-discharge have higher crystallinity,  $D''$ -band is scarcely seen in the Raman spectrum. Therefore, the method to be introduced in this report is useful for only CVD-grown MWCNTs. But, the MWCNTs synthesized by arc-discharge are not used in the practical applications due to the impossibility of mass production. Therefore, it is still worthy of developing the method have evaluating the purity of CVD-grown MWCNTs that are unexceptionally shown  $D''$ -band in the Raman spectrum. We will provide the detailed protocols for determining the purity of CVD-grown MWCNTs, which are confirmed by testing the mixture of high purity MWCNTs and amorphous carbon particles.

## 2. Experimental

In order to synthesize MWCNTs, Fe/Mo/ $\text{Al}_2\text{O}_3$  particles were prepared using combustion method. Fe/Mo particles were used as catalysts and  $\text{Al}_2\text{O}_3$  was supporting the catalysts. Metal-organic precursors of iron nitrate, molybdenum acetate, and aluminum nitrate were dissolved in deionized water, and then the prepared solution was transformed into catalyst powder by thermal treatment at  $450^\circ\text{C}$  for 30 min in air ambient. The quartz boat having the catalyst powder was placed inside a quartz tube reactor. After heating the reactor to  $700^\circ\text{C}$  in Ar atmosphere, a gas mixture of  $\text{C}_2\text{H}_4/\text{H}_2$  (1:1) was fed into the reactor with a pressure of 1 atm for the synthesis, followed by cooling to room temperature under Ar atmosphere.

The morphologies of MWCNTs were investigated using scanning electron microscopy (SEM, JEOL JSM 6700F) and

transmission electron microscopy (TEM, FEI Tecnai 20, 200 kV). The amount of catalyst particles included in the synthesized MWCNT samples was investigated by TGA. Amorphous carbon powder was purchased from Aldrich to be used as an impurity material. In order to verify the proposed evaluation method, several intermediate purity samples, having the purity range of 0–100% with 20% interval, were prepared by mixing high purity MWCNTs and amorphous carbon powder, considered as 100% and 0%, respectively. Then, Raman spectroscopy measurement was carried out to evaluate the purity of MWCNTs using a Raman microscope (TRIVIA, Acton).

## 3. Results and Discussion

Through optimizing the experimental parameters for the synthesis of MWCNTs, we prepared very high purity MWCNTs, as can be seen in Figure 1(a). Despite of a number of observations using SEM, we could not see carbonaceous particles. TEM image (inset figure) clearly shows the synthesized materials are all of MWCNTs with hollow insides. According to TGA analysis, two weight-percent (wt%) of catalyst metal particles is included in the prepared MWCNTs. However, we could hardly see the catalyst particles during both SEM and TEM observations. It is believed that 2 wt% of catalyst particles corresponds to an extremely small *volume* percent that could be negligible, because the bulk density of catalyst particle is much larger than that of MWCNTs. Furthermore, most of the catalyst particles are residing inside MWCNTs after the synthesis [20], which does not affect Raman spectrum. Therefore, this high purity MWCNTs could be considered as a reference material with 100% purity. Figure 1(b) represents the Raman spectrum of a reference MWCNT sample. The spectrum was taken using an excitation wavelength of 633 nm. The Raman spectrum shows a typical feature of MWCNTs: the first ordered  $D$ -,  $G$ -, and  $D'$ -band peaks located at around 1350, 1582, and  $1610\text{ cm}^{-1}$ , respectively.  $G$ -band peak is assigned to “in plane” displacement of the carbons

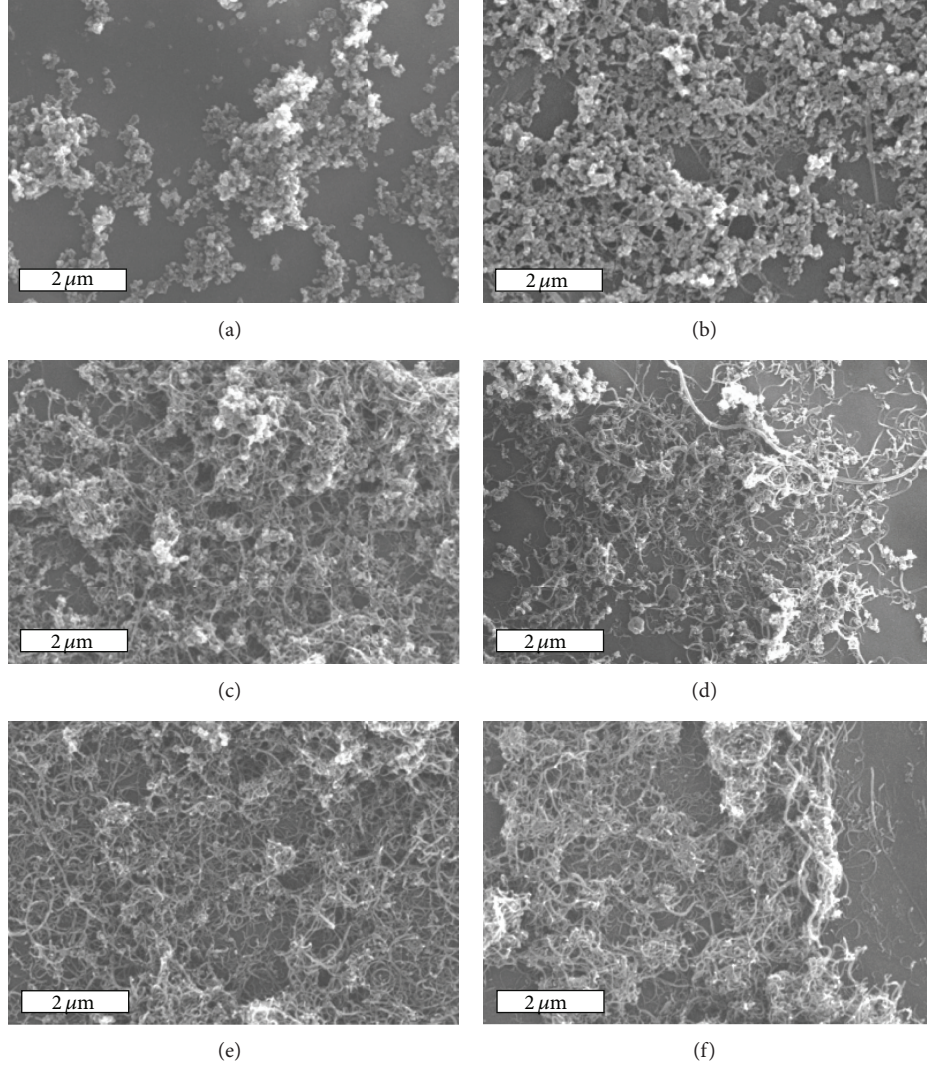


FIGURE 2: SEM images of purity-controlled MWCNT samples by mixing amorphous carbon particles and highly pure MWCNTs: (a) 0%, (b) 20%, (c) 40%, (d) 60%, (e) 80%, and (f) 100%.

strongly coupled in the hexagonal sheets [17].  $D$ - and  $D'$ -band are found when disorder is introduced into the graphite structure. For this reason, the intensity ratio of  $D$ -band to  $G$ -band ( $I_D/I_G$ ) has been used to determine the crystallinity of MWCNTs [15, 20]. However, according to Behler et al. [15], the intensity and position of  $D$ -band peak are varied with the excitation wavelength of laser to a great extent. Therefore, the measurement of  $I_D/I_G$  cannot be used as a standard method for evaluating the crystallinity of MWCNTs although  $I_D/I_G$  is used to compare the crystallinity of carbon nanotubes when the identical wavelength is used. Another broad peak ( $D''$ -band) located at around  $1500\text{ cm}^{-1}$  is also found in the Raman spectrum (Figure 1(b)).  $D''$ -band was reported to be associated with amorphous  $sp^2$ -bonded forms of carbon [21, 22]. Unlike  $I_D/I_G$ , the intensity ratio of  $D''$ -band to  $G$ -band ( $I_{D''}/I_G$ ) was found to be invariable with the excitation wavelength of laser. In addition,  $D''$ -band is associated with only amorphous carbons. Hence, we suggest  $I_{D''}/I_G$  instead

of  $I_D/I_G$  to be used for representing the crystallinity of carbon nanotubes.  $I_{D''}/I_G$  of the reference samples obtained from Figure 1(b) is 0.06. On the other hand,  $I_{D''}/I_G$  of amorphous carbon particles that was purchased from Aldrich is 0.37. We suggest that  $I_{D''}/I_G$  of the high purity MWCNTs (0.06) and amorphous carbons (0.37) should represent the purities of 100% and 0%, respectively. Therefore, the purity of MWCNTs ( $P_{MW}$ ) can be simply determined by an equation of

$$P_{MW}(\%) = \left( \frac{AC(D''/G) - MW(D''/G)}{AC(D''/G) - RMW(D''/G)} \right) \times 100, \quad (1)$$

where  $AC(D''/G)$ ,  $MW(D''/G)$ , and  $RMW(D''/G)$  are  $D''/G$  ratios of amorphous carbon particles, MWCNTs being tested, and reference MWCNTs, respectively. In order to verify the suggested equation, intermediate purity samples were prepared with 20% purity interval from 0% to 100% by mixing high purity MWCNTs and amorphous carbon particles.

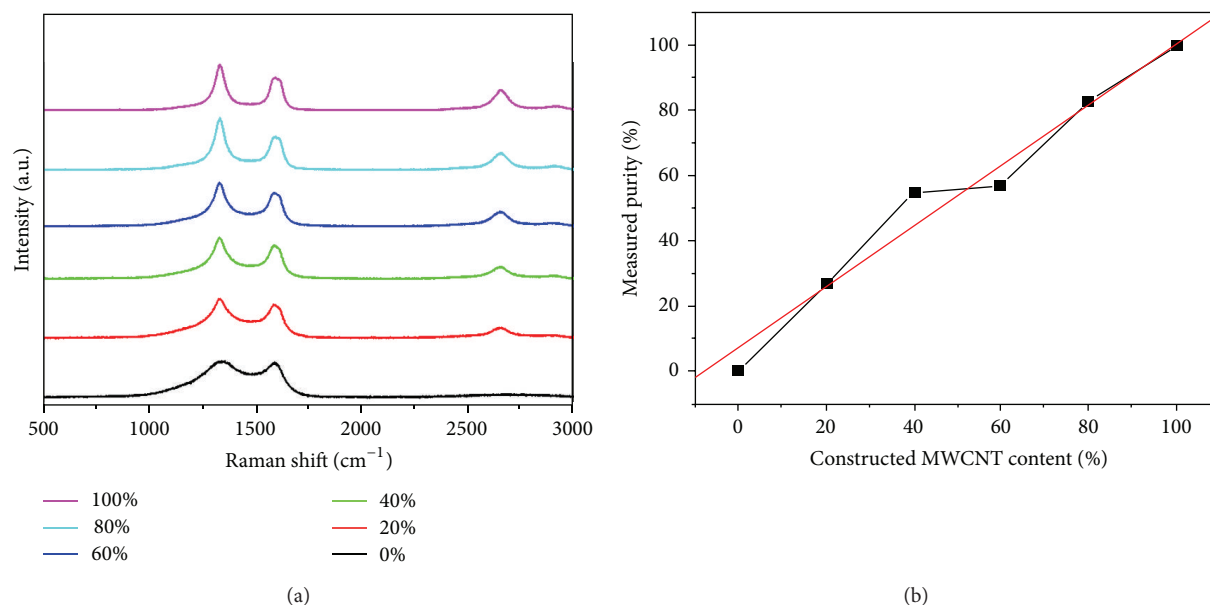


FIGURE 3: (a) Raman spectra, taken using an excitation wavelength of 633 nm, of purity-controlled MWCNT samples with purities ranging from 0% to 100% with 20% interval. (b) Purity measured from Raman spectroscopy using 633 nm laser versus constructed content of MWCNTs.

First, we dispersed the MWCNTs and amorphous carbon particles in the dimethylformamide (DMF) separately with 1 mg/100 ml concentration. Then, two solutions were mixed with designed ratios. The mixed solutions were dropped onto glass and Si substrates for the analyses by Raman and SEM, respectively. Figure 2 shows the SEM images of several intermediate purity samples. It can be clearly observed from these figures that the amount of impurity decreases as the purity of MWCNT increases. However, it is hard to define the purity of samples quantitatively by using SEM measurements.

Six different intermediate samples prepared with different purities (0%–100%) were analyzed by Raman spectroscopy. Figure 3(a) shows the Raman spectra, taken using an excitation wavelength of 633 nm, of MWCNTs with various purities. 100% and 0% purity samples show the Raman spectra of reference MWCNTs and amorphous carbons, respectively. Although the deconvoluted peaks of 0% purity sample are not presented here, it was found that the Raman spectrum of 0% purity sample is composed of not only conventional  $D$ - and  $G$ -bands but also  $D''$ -band with a considerable intensity. With increasing the purity of MWCNTs, full width at the half maximum (FWHM) of the peak at 1200–1400  $\text{cm}^{-1}$  ( $D + D''$ -bands) decreases because the contribution of  $D''$ -band is getting smaller. We applied the proposed equation to the series of MWCNT samples with intentionally varied purity, and the results are illustrated in Figure 3(b). Figure 3(b) plots the purity evaluated using the equation to the constructed contents with varying purities from 0% to 100%. The linear fitting yielded a slope close to unity, 0.96, and the confidence value  $R^2$  was 0.95. Thus, the evaluated purities of MWCNTs are in good agreement with the designed values of constructed content. It can be therefore said that the suggested

equation can be simply used for evaluating the purity of MWCNTs.

Various lasers with different excitation wavelengths are used in Raman spectroscopy. Therefore, in order to standardize an evaluation method using Raman spectroscopy, the method should not be dependent upon the excitation wavelength. A number of previous literatures reported the crystallinity of carbon nanotubes determined from the intensity ratio of  $D$ -band ( $\sim 1350 \text{ cm}^{-1}$ ) to  $G$ -band ( $I_D/I_G$ ). However, the measurement of  $I_D/I_G$  cannot be used as a standardized evaluation method since the intensity of  $D$ -band is significantly dependent upon the wavelength of laser [15]. In this study, we measured the purities of several different samples by using the excitation wavelength of not only 633 nm shown in Figure 3(b) but also 532 nm to verify the independency of this method on the wavelength. Generally, 633 nm and 532 nm laser are widely used for the Raman scattering measurement of MWCNTs. Figure 4 represents the purities evaluated from the Raman spectra taken using 532 nm laser as a function of constructed content.  $I_{D''}/I_G$ , obtained using an excitation wavelength of 532 nm, of high purity reference MWCNTs and amorphous carbon particles was 0.07 and 0.49, respectively. Although  $I_{D''}/I_G$  measured using 532 nm laser is slightly different from that obtained using 633 nm laser, the purity measured using an excitation wavelength of 532 nm is also well matched to the constructed content, as can be seen in Figure 4. The linear fitting yielded a slope of 1.03, and the confidence value  $R^2$  was 0.96. Thus, the purities of MWCNTs evaluated using excitation wavelength of 532 nm are also in good agreement with the designed values of constructed content. It can be therefore concluded that evaluating the purity of MWCNTs using  $I_{D''}/I_G$  is valid regardless of excitation wavelength of laser.



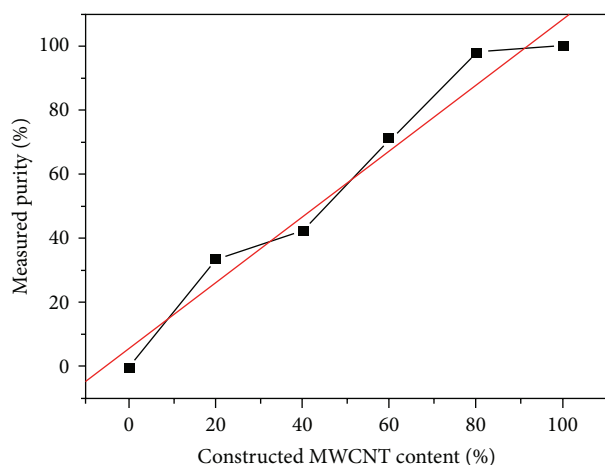


FIGURE 4: Purity measured from Raman spectroscopy using an excitation wavelength of 532 nm versus constructed content of MWCNTs.

#### 4. Conclusion

A quantitative method for evaluating the purity of MWCNTs using Raman spectroscopy was newly proposed. The purity of MWCNTs was determined by comparing the intensity ratio of  $D''$ -band to  $G$ -band ( $I_{D''}/I_G$ ) of MWCNTs being tested with that of the high purity reference material. The established method was verified by testing the mixture of reference MWCNTs of high purity and amorphous carbon particles. Furthermore, it was found that the proposed method was found to be valid regardless of the excitation wavelength of laser.

#### Acknowledgment

This work was supported by Institute for Basic Science (IBS) (EM1304).

#### References

- [1] L. J. Cui, H. Z. Geng, W. Y. Wang, L. T. Chen, and J. Gao, "Functionalization of multi-wall carbon nanotubes to reduce the coefficient of the friction and improve the wear resistance of multi-wall carbon nanotube/epoxy composites," *Carbon*, vol. 54, pp. 277–282, 2013.
- [2] Y. J. Noh, H. S. Kim, and S. Y. Kim, "Improved electrical conductivity of a carbon nanotube mat composite prepared by in-situ polymerization and compression molding with compression pressure," *Carbon Letters*, vol. 13, no. 4, pp. 243–247, 2012.
- [3] Y. C. Choi, Y. M. Shin, Y. H. Lee et al., "Controlling the diameter, growth rate, and density of vertically aligned carbon nanotubes synthesized by microwave plasma-enhanced chemical vapor deposition," *Applied Physics Letters*, vol. 76, no. 17, pp. 2367–2369, 2000.
- [4] S. Akita, Y. Ohshima, and T. Arie, "Nanoincandescent consisting of individual carbon nanotubes," *Applied Physics Express*, vol. 4, no. 2, Article ID 025101, 2011.
- [5] C. T. Chang, C.-P. Juan, and H.-C. Cheng, "Pillar height dependence of field-emission properties in an array of carbon nanotube pillars," *Japanese Journal of Applied Physics*, vol. 52, no. 18, Article ID 085101, 2013.
- [6] A. Mierczynska, M. Mayne-L'Hermite, G. Boiteux, and J. K. Jeszka, "Electrical and mechanical properties of carbon nanotube/ultrahigh-molecular-weight polyethylene composites prepared by a filler prelocalization method," *Journal of Applied Polymer Science*, vol. 105, no. 1, pp. 158–168, 2007.
- [7] F. L. Jin and S. J. Park, "Recent advances in carbon-nanotube-based epoxy composites," *Carbon Letters*, vol. 14, no. 1, pp. 1–13, 2013.
- [8] J. S. Kim, S. J. Cho, K. S. Jeong, Y. C. Choi, and M. S. Jeong, "Improved electrical conductivity of very long multi-walled carbon nanotube bundle/poly (methyl methacrylate) composites," *Carbon*, vol. 49, no. 6, pp. 2127–2133, 2011.
- [9] Y. C. Choi, Y. M. Shin, S. C. Lim et al., "Effect of surface morphology of Ni thin film on the growth of aligned carbon nanotubes by microwave plasma-enhanced chemical vapor deposition," *Journal of Applied Physics*, vol. 88, no. 8, pp. 4898–4903, 2000.
- [10] Y. S. Park, H. S. Moon, M. Huh et al., "Synthesis of aligned and length-controlled carbon nanotubes by chemical vapor deposition," *Carbon Letters*, vol. 14, no. 2, pp. 99–104, 2013.
- [11] P. Mahanandia, P. N. Vishwakarma, K. K. Nanda et al., "Synthesis of multi-wall carbon nanotubes by simple pyrolysis," *Solid State Communications*, vol. 145, no. 3, pp. 143–148, 2008.
- [12] J. H. Lehman, M. Terrones, E. Mansfield, K. E. Hurst, and V. Meunier, "Evaluating the characteristics of multiwall carbon nanotubes," *Carbon*, vol. 49, no. 8, pp. 2581–2602, 2011.
- [13] J. P. C. Trigueiro, G. G. Silva, R. L. Lavall et al., "Purity evaluation of carbon nanotube materials by thermogravimetric, TEM, and SEM methods," *Journal of Nanoscience and Nanotechnology*, vol. 7, no. 10, pp. 3477–3486, 2007.
- [14] R. A. DiLeo, B. J. Landi, and R. P. Raffaele, "Purity assessment of multiwalled carbon nanotubes by Raman spectroscopy," *Journal of Applied Physics*, vol. 101, no. 6, Article ID 064307, 2007.
- [15] K. Behler, S. Osswald, H. Ye, S. Dimovski, and Y. Gogotsi, "Effect of thermal treatment on the structure of multi-walled carbon nanotubes," *Journal of Nanoparticle Research*, vol. 8, no. 5, pp. 615–625, 2006.
- [16] W. Li, H. Zhang, C. Wang et al., "Raman characterization of aligned carbon nanotubes produced by thermal decomposition of hydrocarbon vapor," *Applied Physics Letters*, vol. 70, no. 20, pp. 2684–2686, 1997.
- [17] T. Jawhari, A. Roid, and J. Casado, "Raman spectroscopic characterization of some commercially available carbon black materials," *Carbon*, vol. 33, no. 11, pp. 1561–1565, 1995.
- [18] Y. S. Park, Y. C. Choi, K. S. Kim et al., "High yield purification of multiwalled carbon nanotubes by selective oxidation during thermal annealing," *Carbon*, vol. 39, no. 5, pp. 655–661, 2001.
- [19] X. Song, Y. Liu, and J. Zhu, "Multi-walled carbon nanotubes produced by hydrogen DC arc discharge at elevated environment temperature," *Materials Letters*, vol. 61, no. 2, pp. 389–391, 2007.
- [20] Z. Balogh, G. Halasi, B. Korbély, and K. Hernadi, "CVD-synthesis of multiwall carbon nanotubes over potassium-doped supported catalysts," *Applied Catalysis A*, vol. 344, no. 1–2, pp. 191–197, 2008.



- [21] D. S. Knight and W. B. White, "Characterization of diamond films by Raman spectroscopy," *Journal of Materials Research*, vol. 4, no. 2, pp. 385–393, 1989.
- [22] P. V. Huong, "Structural studies of diamond films and ultrahard materials by Raman and micro-Raman spectroscopies," *Diamond and Related Materials*, vol. 1, no. 1, pp. 33–41, 1991.